Optical Spectroscopy of Tungsten Carbide for Electron Electric Dipole Moment Search

by

Jeongwon Lee

A dissertation submitted in partial fulfillment
of the requirements for the degree of
Doctor of Philosophy
(Physics)
in The University of Michigan
2012

Doctoral Committee:

Assistant Professor Aaron E. Leanhardt, Chair
Professor Timothy E. Chupp
Professor James T. Liu
Professor Georg A. Raithel
Professor Roseanne J. Sension

For my parents.

ACKNOWLEDGEMENTS

First I would like to thank my advisor, Aaron Leanhardt, for his guidance and friendship throughout the years. I learned the importance of intuitive thinking, the virtue of hard work, and efficient communications skills from him. He was also patient enough to teach me, who had zero experience in experimental atomic physics by the time I joined the group. I remember him saying, "Everyone has to start somewhere", on the day we met, when I showed concerns about how little background I had. This motivated me to explore the exciting new field of atomic molecular optical physics.

The person I spent most of my time with in the lab was Jinhai, the postdoc who worked with me on the WC electron EDM project. Without his expertise in molecular beam production, I wouldn't have the results shown in this thesis. He taught me many subtle experimental tricks which I wouldn't be able to learn from anywhere else.

I was lucky to work with many great lab mates, Emily, Yisa, Skyler, and Kaitlin. Even though we haven't worked on the same project, I have learned a lot from each of them. Emily helped me out many times with the computer interface for data acquisition. She also has good sense of humor giving positive energy in the lab. Yisa and I shared interesting conversations in many fields of physics, which always motivated me to read broader range of literature. Skyler joined our lab as a beginning graduate student when I was heading towards the end of my Ph.D. years. I had a great time sharing ideas with him, and giving feedback to each other. Kaitlin started working in our lab as an undergraduate showing good progress in multiple projects,

and continued as a graduate student. Her organizing ability is something that I would like to follow.

Several undergraduates contributed to the WC electron EDM project. Rabin spent two summers in our lab working with me on the continuous supersonic beam source. He showed great working ethics, not leaving the lab until we finish what we planned for the day. Charlie and Peter worked briefly over one summer, each working on the optimization of filament evaporation and electric field plates. Ross and Kevin each worked on electric field simulation and the tungsten thin film deposition. I hope the best for everyone.

I would also like to thank our collaborators for all of their help. Ed Meyer and John Bohn from JILA helped us to develop the idea of using the WC molecule for electron EDM measurement. Alex Petrov and Anatoly Titov from PNPI further calculated many important molecular constants related to the systematic uncertainties of the EDM experiment, which is the main focus of my thesis. I appreciate Tim Steimle's group from ASU for sharing their experimental results as soon as it came out, and Michael Morse from Univ. of Utah for generously providing many unpublished results of WC spectroscopy.

Looking back, I am in great debt with my undergraduate advisors, Hie-Tae Moon, Soonchil Lee, and Hawoong Jeong from KAIST, for stimulating my interest in physics. They were great mentors, guiding and encouraging me to do Ph.D. in physics.

Lastly, I thank my parents deeply for their love and support. My father Youn-jae, a scholar himself, has been my role model, and my mother, Sun-ah, always gave me strength. I dedicate my work to you.

TABLE OF CONTENTS

LIST OF FIGURES

Figure

LIST OF TABLES

Table

LIST OF APPENDICES

Appendix

ABSTRACT

Optical Spectroscopy of Tungsten Carbide for
Electron Electric Dipole Moment Search

by

Jeongwon Lee

Chair: Aaron E. Leanhardt

Searching for a permanent electron electric dipole moment (EDM) is a powerful tool to probe for physics beyond the Standard Model. We identified the $X^3\Delta_1$ ground state of tungsten carbide (WC) molecule as a candidate system for the electron EDM search. This work focuses on two main parts: one being devoted to the development of various forms of intense molecular beam sources, and the other consisting of the analysis of the EDM sensitive molecular transition. Initially, we developed a supersonic beam of WC molecules in a continuous form; however, this approach had several limitations. To overcome these issues, we designed a second generation beam source in a pulse form. We used laser induced fluorescence (LIF) spectroscopy on a pulse supersonic beam to detect the molecules through the $[20.6]\Omega = 2, v' = 4 \leftarrow X^3\Delta_1, v" = 0$ transition. The hyperfine structure and the Ω-doublet of the transition were measured, which were essential for estimating the size of the potential systematic uncertainties for the electron EDM measurement. For further suppression of systematic uncertainty, an EDM measurement scheme utilizing the g-factor crossing point of the

Ω-doublet levels was studied. On the other hand, flux and internal temperature of the molecular beam were characterized, setting the limit of the statistical uncertainty of the EDM experiment. With the given results, the prospect of an electron EDM experiment with the $X^3\Delta_1$ state of WC molecule is discussed.

CHAPTER I

Introduction

1.1 Searching for physics beyond the Standard Model

The Standard Model of particle physics cannot explain several important experimental observations. For example, why are the strengths of the fundamental forces so different (i.e. the hierarchy problem)? Why is there a dominance of matter over anti-matter in the universe (i.e. baryogenesis)? Various extensions to the Standard Model, most notably Supersymmetry (SUSY), have been developed with the goal of resolving these issues. These extensions predict 'new physics' that can be observed by experiments ranging in size from the Large Hadron Collider to laboratory based tabletop precision measurements [JW09]. This work focuses on the latter, specifically, an electron electric dipole moment search using the valence electrons in the $X^3\Delta_1$ ground state of tungsten carbide molecules.

As shown on Fig. 1.1, any permanent electric dipole moment (EDM) violates both parity (P) and time-reversal (T) symmetries [PR50]. According to the CPT Theorem, T-violation and CP-violation are equivalent such that EDMs enter the Standard Model through the CP-violating phase contained in the CKM Matrix [Ae08]. For the electron, the Standard Model EDM prediction is limited to $|d_e| \approx 10^{-38}$ e-cm; while, various extensions to the Standard Model predict electron EDMs that are over 10 orders of magnitude larger [PR05]. These various predictions are shown

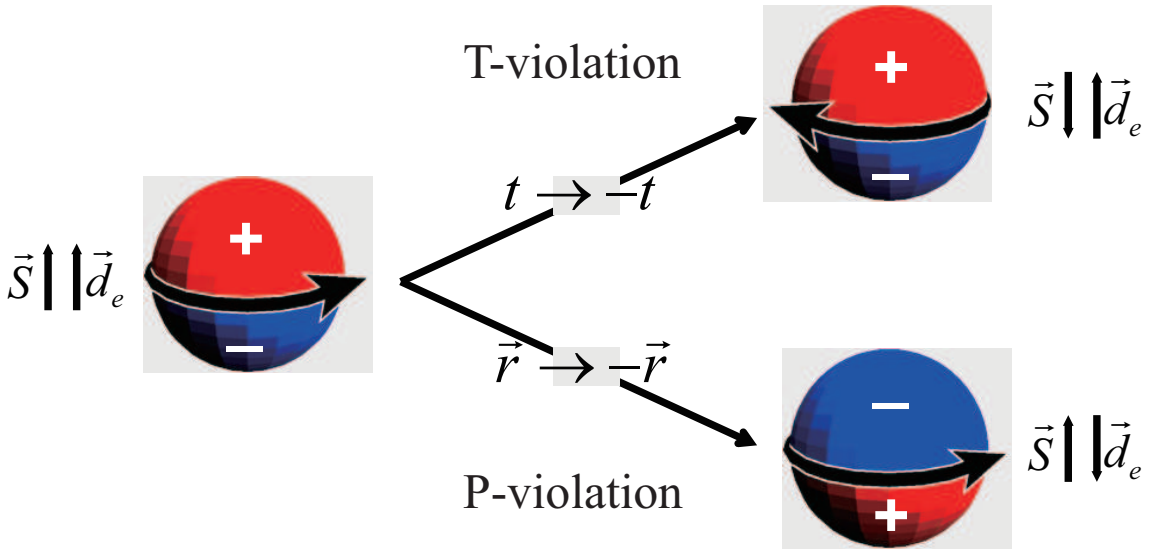

Figure 1.1: P- and T- violations of a non-zero electron EDM.

on Fig. 1.2 along with the current experimental limit on the electron EDM, which is at $|d_e| < 1.05 \times 10^{-27}$ e-cm [HKS+11]. This gap between predictions provides a large window where a non-zero electron EDM signal would be a background-free discovery of physics beyond the Standard Model; a null measurement would serve as a constraint for numerous theories. One can see that the current experimental limit already started constraining considerable parts of SUSY models shown on Fig. 1.2, and 2 to 3 orders of magnitude improvement in the experimental limit would be probing into more interesting regions, also serving as even tighter constraints. The EDM searches are not limited to the electron, and experiments are underway in a variety of systems [Com07, GSL+09].

1.2 Electron EDM experiment with $X^3\Delta_1$ state of WC

In this section, we will show an overview of the electron EDM experiment with the $X^3\Delta_1$ state of WC. First, we will describe a general way of measuring the electron EDM: what factors we need to care about, and how heavy polar molecules have

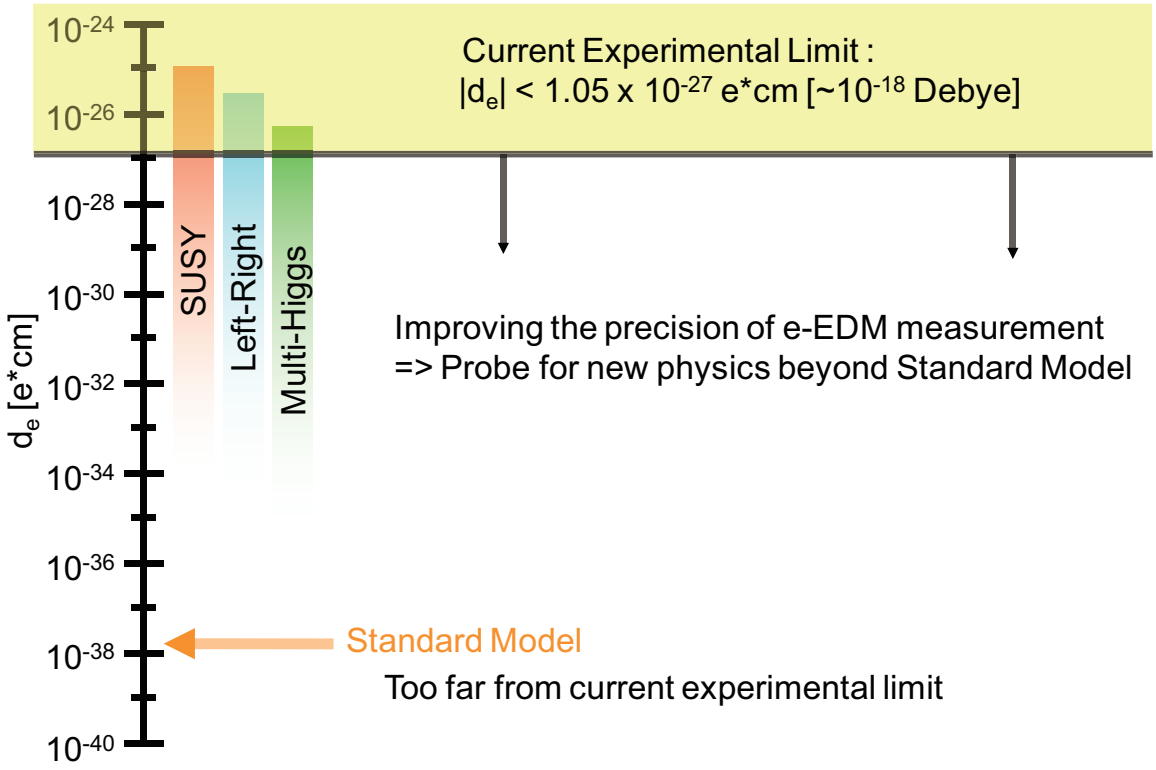

Figure 1.2: The electron Electric Dipole Moment(EDM) predictions from the Standard Model and various extensions are shown.

favorable qualities related to these factors. Then, we will move on to showing special advantages of using the $X^3\Delta_1$ ground state of WC, which come from its molecular structure. Towards the end, we will introduce the systematic uncertainties of the electron EDM experiment with the WC system, which need to be characterized.

1.2.1 Electron EDM measurement with heavy polar molecules

The goal of every EDM experiment is to measure an EDM induced Stark shift, which in our case is, to measure a Stark shift d_eE in the electronic energy level. Considering the case of J=1 spin triplet states, the energy differences between the $M = \pm 1$ levels are measured under two different conditions of magnetic and electric fields in parallel direction, or in antiparallel direction. The measured frequencies, $\nu_\pm$, can be written as,

$$\nu_\pm = \frac{2\mu B \pm 2d_eE}{h}. \tag{I.1}$$

By taking the difference between these two frequency measurements, we effectively cancel out the Zeeman shift term and only leave the Stark shift term $4d_eE/h$, which is proportional to the electron EDM, d_e.

As shown in eq. I.1, the control of the electric field and magnetic field should be considered for electron EDM experiments. Since the electron EDM manifests itself as an energy splitting between spin-up and spin-down states that is proportional to the electric field experienced by the electron, one needs to find a system that would apply a large electric field to the electron. Heavy atoms have been a popular choice in the past [RCSD02, Hei, AMG07, FW09], as the valence electrons experience an enhanced electric field (commonly referred to as an effective electric field) near the nucleus due to relativistic effects [San66]. The second factor to consider is the imperfect cancelation of the Zeeman shifts from limited controllability of the magnetic fields in the system, which would become a source of systematic error in an electron EDM

measurement. In fact, the best experimental limit for the electron EDM measurement with an atomic system was limited by the motional magnetic field [RCSD02]. As an order of magnitude estimate, the Stark shift of an electron EDM at the current experimental limit in one atomic unit of electric field is comparable to the Zeeman shift of a Bohr magneton in a magnetic field of only 1 nG.

The above comparison illuminates the need to apply enormous electric fields to the electron while maintaining exquisite control over residual Zeeman shifts. This can be accomplished by using the valence electrons in a heavy polar molecule [Hin97]. Heavy polar molecules have effective electric fields in the range of $10 \sim 100$GV/cm, which are much larger than that of the atomic systems. The effective electric field scales as $Z^3\alpha^2$, where the polar molecules gain a factor of $100 \sim 1000$ compared with the atomic case, due to the higher polarizability [San67]. Further exploration in this direction from the JILA EDM Group [MBD06, LBL$^+$11] has elucidated the extra benefits of heavy diatomic molecules in $^3\Delta_1$ states for molecule-based electron EDM searches. These benefits include small magnetic moment of the molecule, and the use of internal co-magnetometer, which would be discussed in more detail in the following subsection.

On the other hand, one needs to maximize the resolution of the frequency measurement in order to see a smaller splitting. To put a more intuitive size scale on how small the electron EDM is, the current experimental limit of $|d_e| < 1.05 \times 10^{-27}$ e-cm [HKS$^+$11] corresponds to 5×10^{-19}D; while, typical induced (molecule-frame) electric dipole moments in polar molecules are of the order of a few Debye. This limit converts to a frequency shift in $h \times O$(mHz) level, when tens of GV/cm is accessible from an appropriately chosen heavy polar molecules.

Ramsey spectroscopy [Ram50] could deliver the frequency resolution in the desired range, where we could measure the phase accumulation between the electron spin superposition states, which would be proportional to the energy difference of the

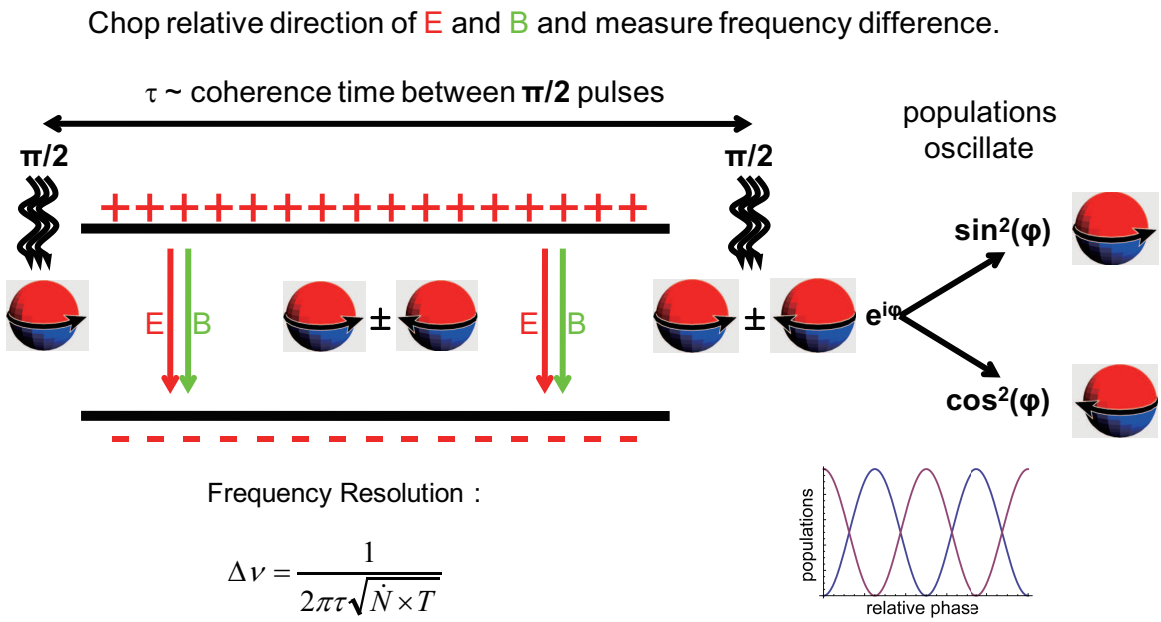

Figure 1.3: Diagram of Ramsey spectroscopy.

states. A simplified diagram of Ramsey spectroscopy is shown in Fig. 1.3. When the electronic spin states are prepared in either spin-up or spin-down states initially, the first $\pi/2$ pulse of oscillatory field would put them in a coherent superposition state of spin-up and spin-down. As the atoms or molecules travel through the interaction region with parallel or anti-parallel electric and magnetic fields, there is a relative phase accumulation of φ between the spin states, which is proportional to $2\mu B \pm 2dE$. The second $\pi/2$ pulse would put the superposition state back into one of the spin states, with the phase information encoded. Since the population of the final state would oscillate depending on this phase, one could use this fringe pattern called the Ramsey fringe as a sensitive phase detector.

The purpose of this diagram is not only to show the well established method of precision frequency measurement, but also to emphasize the relevant experimental parameters for designing an electron EDM experiment. The frequency resolution can be written as,

$$\Delta\nu = \frac{1}{2\pi\tau\sqrt{\dot{N} \times T}}. \tag{I.2}$$

where τ is the coherence time between the $\pi/2$ pulses, $\dot{N}$ is the rate of measurements, and T is the total integration time. From eq. I.2, longer coherence time, faster rate of measurement, and longer integration time would give better resolution. Longer integration time is the obvious one, which is to take multiple sets of data to reduce the statistical noise. However, the first two factors should be carefully considered for experimental design purposes. Coherence time is defined by how long one could preserve the superposition state inside the interaction region. Usually it is limited either by the lifetime of the electronic state, or the mean free path of the molecule. Therefore one should find a long lived electronic state, if not the ground state, and also have a well collimated molecular beam with long mean free path. As for the rate of measurement, in case of a laser induced fluorescence (LIF) detection, strong electric dipole coupling between the EDM state and the read-out state is required, in order to maximize the detection rate of the spin states.

In this thesis work, we investigate the $X^3\Delta_1$ ground state of tungsten carbide (WC) as the candidate molecular system for electron EDM measurement [LMP+09]. This adds to the work on metastable $^3\Delta_1$ states in HfF^+ [LBL+11, MBD06, PMT09], ThF^+ [LBL+11, MB08a], and ThO [MB08a, MB08b, VCG+10], which all share several advantageous features of the $^3\Delta_1$ state. However, up to our knowledge, tungsten carbide is the heaviest molecule which has the $^3\Delta_1$ state in the ground state, where there is an additional benefit of the Ramsey measurement of the electron EDM not being limited by the lifetime of the state. The next subsection will show details of the WC molecular structure, and also explain how some of those are favorable for electron EDM experiments.

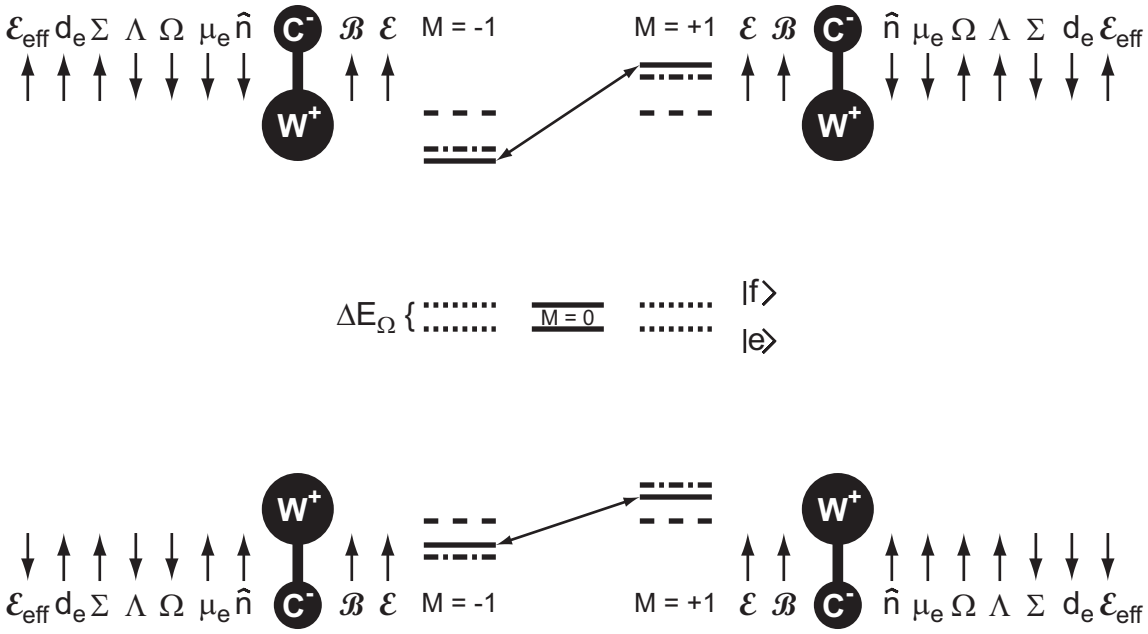

Figure 1.4: The $X^3\Delta_1$, $J = 1$ ro-vibrational ground state of WC in external electromagnetic fields. In the absence of laboratory electric and magnetic fields, the ground state is split into a pair of $J = 1$ parity eigenstates, $|e\rangle$ and $|f\rangle$, with a small energy separation ΔE_Ω (denoted as dotted lines for $|M| = 1$ and solid lines for $M = 0$). From here, applying a laboratory electric field, $\mathcal{E}$, mixes the states of opposite parity and shifts the $|M| = 1$ states by an approximate energy $-\vec{\mu}_e \cdot \vec{\mathcal{E}}$ to locations denoted by dashed lines. Next, in addition to the Stark shift, a laboratory magnetic field, $\mathcal{B}$, shifts the $|M| = 1$ levels by an energy $gM\mu_B\mathcal{B}$ to locations denoted by dash-dot-dash lines. Finally, in addition to the Stark and Zeeman shifts, a non-zero electron electric dipole moment, d_e, shifts the $|M| = 1$ levels by an energy $-\vec{d}_e \cdot \vec{\mathcal{E}}_{\text{eff}}$ to their final locations denoted by solid lines. By taking the difference between the energy splittings of top doublet $|\Delta M| = 2$ transitions and the bottom doublet $|\Delta M| = 2$ transitions, we are left with $\sim 4d_e\mathcal{E}_{\text{eff}}$, which is nominally independent of the laboratory electric and magnetic fields. The energy splittings are not drawn to scale and $g > 0,\ \mathcal{B} > 0,\ d_e > 0$ was assumed. The sign conventions are as follows: (i) the direction of the applied laboratory electric field, $\vec{\mathcal{E}}$, defines the positive direction for the space-fixed quantization axis, (ii) the molecular axis, $\hat{n}$, is defined to point from carbon (C) to tungsten (W) and defines the positive direction for the molecule-fixed quantization axis, and (iii) the projection of the electronic spin along the molecular axis, Σ, defines the positive direction for the electron EDM, $\vec{d}_e$. The projection of each vector quantity along the space-fixed quantization axis is indicated by ↑ or ↓ for the polarized molecular levels. See text for more details and definitions of various parameters.

1.2.2 Electron EDM measurement scheme with $X^3\Delta_1$ state of WC

Tungsten carbide has a $X^3\Delta_1$ ground state with its two valence electrons in a $\sigma\delta$ molecular orbital configuration [Bal00, SSM02, SCCW06, RHJ08]. The designation $^3\Delta_1$ is written as a term symbol, $^{2S+1}|\Lambda|_{|\Omega|}$, in the Hund's case (a) basis, which is not entirely accurate in the limit of large spin-orbit coupling, but will suffice for explanatory purposes. The two valence electrons in tungsten carbide form a $S = 1$ spin triplet with projection $\Sigma = \mp 1$ along the molecular axis. Δ signifies a projection of the net electronic orbital angular momentum along the molecular axis of $\Lambda = \pm 2$. Finally, the projection of the total electronic angular momentum along the molecular axis is $\Omega = \Lambda + \Sigma = \pm 1$.

More generally, even in the limit of strong spin-orbit coupling, the ro-vibrational ground state of tungsten carbide has total angular momentum $J = 1$ with projections $M = 0, \pm 1$ along a space-fixed quantization axis (Fig. 1.4). Additionally, the $J = 1$ ground state has a well-defined value of $|\Omega| = 1$, which represents the projection of the *total* electronic angular momentum (spin *plus* orbital) along the molecular axis. In the absence of laboratory electric fields, the $J = 1$ ground state is split into a pair of $J = 1$ parity eigenstates, known as an Ω-doublet. For the $J = 1, |\Omega| = 1$ ground state of tungsten carbide, the Ω-doublet levels are labeled as $|e\rangle = |-\rangle = \left(|\eta; J, +|\Omega|, M\rangle - |\eta; J, -|\Omega|, M\rangle\right)/\sqrt{2}$ and $|f\rangle = |+\rangle = \left(|\eta; J, +|\Omega|, M\rangle + |\eta; J, -|\Omega|, M\rangle\right)/\sqrt{2}$, with odd $(-)$ and even $(+)$ parities, respectively, where η represents the any remaining labels necessary to fully specify the state.

The small energy splitting, $\Delta E_\Omega \sim h \times \mathcal{O}(\text{kHz})$, between Ω-doublet levels and relatively large induced electric dipole moment, $\mu_e \sim \mathcal{O}(\text{D})$, of the WC molecule, allows for a relatively weak laboratory electric field, $\mathcal{E} \sim \mathcal{O}(\text{V/cm})$, to mix the states of opposite parity completely and to polarize the molecule fully. The polarization of tungsten carbide has the polarity W^+C^-, such that the induced (molecule-frame)

electric dipole moment points *along* the molecular axis (i.e. from C^- to W^+). The dc laboratory electric field provides the space-fixed quantization axis for the remainder of the discussion. Furthermore, it only couples states with $\Delta M = 0$ and an electric dipole selection rule forbids coupling between states with $\Delta J = 0$ & $\Delta M = 0$ for $M = 0$ levels. As such, the $M = 0$ levels do not mix and are nominally unaffected by laboratory electric and magnetic fields[1]. With a laboratory electric field applied, the energies of the $J = 1,\ |M| = 1$ levels follow $\pm\sqrt{(\Delta E_\Omega/2)^2 + (\mu_e \mathcal{E})^2}$, where the zero of energy is taken at the midpoint of the Ω-doublet. In the limit $\mu_e \mathcal{E} \gg \Delta E_\Omega$, the $J = 1,\ |M| = 1$ levels are no longer eigenstates of parity and instead have (i) a definite value of the signed quantum number Ω and (ii) a non-zero effective electric field, $\mathcal{E}_{\text{eff}}$, experienced by the valence electrons that is nominally *independent* of the applied laboratory electric field when the molecule is fully polarized. A non-zero electron electric dipole moment, d_e, shifts the $|M| = 1$ levels by an energy $-\vec{d}_e \cdot \vec{\mathcal{E}}_{\text{eff}}$. The effective electric field would be in the tens of GV/cm range, which will be calculated in detail in Chapter 4.

Several sources of systematic error are proportional to the laboratory electric field [e.g. Zeeman shifts due to (i) leakage currents and (ii) $\vec{v}\times\vec{\mathcal{E}}/c^2$ effective magnetic fields, where $\vec{v}$ is the velocity of molecules moving through the laboratory electric field $\vec{\mathcal{E}}$ and c is the speed of light], while a potential electron EDM signal is proportional to $\mathcal{E}_{\text{eff}}$. The saturation of $\mathcal{E}_{\text{eff}}$ when the molecule is fully polarized allows for a large variation of the laboratory electric field to search for systematic effects while leaving a true EDM signal unaffected. Furthermore, the small magnitude of $\mathcal{E}$ reduces the overall magnitude of these potential systematic errors, which is in sharp contrast to EDM searches using the valence electrons in atoms (Tl [RCSD02] and Cs [Hei, AMG07, FW09]) and some molecules (YbF [HSTH02] and PbF [SR06]), where laboratory

[1]Note: all M levels of the $J = 1$ rotational ground state will mix with the corresponding M levels of the $J = 2$ rotationally excited state, however this mixing will be minimal for sufficiently weak laboratory electric fields in the limit $\Delta E_\Omega \ll \mu_e \mathcal{E} \ll hcB$, where h is the Planck constant, c is the speed of light, and B is the rotational constant of the molecular state.

electric fields of order 10^5 V/cm and 10^4 V/cm must be applied, respectively.

For a laboratory magnetic field, $\vec{\mathcal{B}}$, applied parallel or anti-parallel to the electric field $\vec{\mathcal{E}}$, the $|M| = 1$ levels shift in energy by an amount $gM\mu_B\mathcal{B}$ due to the Zeeman effect, where g is the magnetic g-factor, μ_B is the Bohr magneton, and $\mathcal{B} > 0$ and $\mathcal{B} < 0$ represents $\vec{\mathcal{B}}$ parallel and anti-parallel to $\vec{\mathcal{E}}$, respectively. For a good Hund's case (a) state, the g-factor for a rotational level J is given by $g_J \approx \Omega(g_L\Lambda + g_S\Sigma)/J(J+1)$. For the $X^3\Delta_1$ ground state of tungsten carbide, $\Lambda = \pm 2$ and $\Sigma = \mp 1$, which yields $g_J \approx 0$ under the approximations $g_S \approx 2$ and $g_L \approx 1$ for the spin and orbital g-factors of the electron, respectively. Thus, the inherent sensitivity of the molecular levels to magnetic fields is significantly reduced compared to that of an unpaired valence electron in atoms such as Tl [RCSD02] and Cs [Hei, AMG07, FW09] and molecules such as YbF [HSTH02] and PbO [BHJD09]. A similar reduction in g-factor appears in the $^2\Pi_{1/2}$ state of PbF [SR06] and $^3\Delta_1$ states of HfF^+ [LBL+11, MBD06, PMT09], ThF^+ [LBL+11, MB08a], and ThO [MB08a, MB08b, VCG+10]. As for the $X^3\Delta_1$ state of WC molecule, the g-factor has been measured to be 0.022 [WS11a].

Even in the presence of a non-zero molecular g-factor, the pair of $|\Delta M| = 2$ transitions shown in Fig. 1.4 share a common Zeeman shift with opposite direction of the EDM shift. Thus, taking the difference between the transition energies yields a result, $4d_e\mathcal{E}_{\text{eff}}$, that is exclusively due to the electron EDM. This eliminates the need of laboratory electric field reversal with respect to the magnetic field, as the molecule has a pair of energy levels effectively doing the reversal. This of course assumes that the g-factors of the upper and lower transitions are equal, which is a good approximation, but not an exact result [BHJD09]. The difference in g-factors will be discussed many times throughout this thesis work.

In a pure Hund's case (a) basis state, e.g. $^3\Delta_1$, the Ω-doublet splitting is more appropriately called Λ-type doubling and is caused by rotational and spin-orbit effects that mix in excited $^{2S+1}\Sigma_{|\Omega|}$ states of a particular parity. The splitting can be com-

puted with 4^{th}-order perturbation theory by appropriately accounting for the many routes through which the perturbation can be transmitted [BCM87]. However, the process is quite sensitive to the detailed energy differences between the intermediate electronic states, therefore, experimental determination is necessary.

Without an applied laboratory electric field, the parity eigenstates, $|e\rangle$ and $|f\rangle$, have slightly different g-factors as the $X^3\Delta_1$ ground state is being affected by neighboring electronic states due to spin-orbit coupling. Under the application of a laboratory electric field large enough to fully mix the parity eigenstates, the g-factors for the *upper* and *lower* transitions shown in Fig. 1.4 deviate further. For $^3\Delta_1$ molecules in the ground rotational state, the leading order correction to $g_{J=1}$ is due to an interference between the Stark mixing and Zeeman mixing of the $J = 2$ rotational excited state. The difference in g-factors scales as $\Delta g(\mathcal{E})/g_{J=1} = (g_{\text{upper}} - g_{\text{lower}})/g_{J=1} \approx +(3/10)(\mu_e \mathcal{E}/hcB)$ [BHJD09]. As a result, the energy difference between the pair of $|\Delta M| = 2$ transitions shown in Fig. 1.4 will have a small laboratory electric field and magnetic field dependence, rather than simply being equal to $4d_e\mathcal{E}_{\text{eff}}$. This could potentially introduce a systematic uncertainty and the size of this uncertainty needs to be addressed.

1.3 Outline

This thesis will mainly discuss ground work that we have done for the newly proposed molecule based electron EDM experiment using the $X^3\Delta_1$ ground state of WC. We will show how we create the WC molecular beam, how we estimate statistical uncertainty based on the flux and internal temperature of the beam, and how we characterize the key systematic uncertainties, which would put the WC system in an unique position among many molecule based electron EDM experiments.

In Chapter 2, we will discuss the experimental efforts of generating the WC beam in a continuous form. We were able to detect the mass spectrum of WC with the

continuous beam source, however, the optical detection of WC was not successful. We analyze the main limitations of the continuous beam source and show some ideas for future direction of the continuous beam source. Chapter 3 will discuss the second generation experiment with a pulse molecular beam source, where we were able to detect the optical spectrum of WC. The optical spectrum of tungsten will also be shown in chapter 3, as its isotope shifts can give us valuable information not only related to the electron EDM experiment, but also in other fields of physics. In Chapter 4, we will analyze the optical spectrum of WC to extract the statistical sensitivity and systematic uncertainties for electron EDM measurement. Chapter 5 will summarize and conclude this work.

CHAPTER II

First Generation Experiment: Continuous Supersonic Beam Source Measurements

In this chapter, I will focus on describing our experimental efforts of generating and detecting the WC molecular beam in a continuous form. As the experiment plans to measure the electron EDM at the rovibrational ground state of the WC molecules, efficient cooling of internal degrees of freedom is required. There have been several different approaches to cool rovibrational levels of molecules, which could be grouped into two main categories: laser cooling [SBD10, LWO11] and collisional cooling [KG51, DCKD09]. There are approaches from the other direction, which is to bind the pre-cooled atoms into molecules, such as the photoassociation method [WBZJ99] and the Feshbach method [SPH03, NOW$^+$10]. However, these are not applicable to our case of WC molecules because neither W or C can be laser cooled.

Laser cooling is based on momentum kicks that the atoms or molecules get when they scatter off photons. With a closed cycling transition to continuously scatter photons, laser cooling could reach micro-Kelvin temperatures for atoms [MS99]. However, a cycling transition becomes increasingly tough to find in molecules as there are many vibrational and rotational levels within the electronic states, causing multiple photon decay paths from the excited state, and increasing the number of repump lasers to an unrealistic level. Therefore, only a handful of molecules are being considered for laser

cooling technique, and only the strontium fluoride molecule has been laser cooled experimentally so far [SBD10].

On the other hand, collisional cooling is applicable to a variety of molecules due to the simplicity of the physics involved. In particular, the supersonic expansion technique has been a widely accepted method of cooling molecules in order to simplify their optical spectra. It utilizes the energy conversion process between different degrees of freedoms through colliding the target molecule with an inert buffer gas. The typical rotational temperature one can achieve is in the 1 to 10K range, which is enough to put more than 50% of WC molecules in their rovibrational ground state.

I spent the first two years in the lab developing a continuous supersonic beam source for the electron EDM experiment. During this time, I have measured the WC mass spectroscopy and also studied the supersonic beam properties through optical spectroscopy of tungsten. However, there were multiple limitations of the continuous supersonic beam technique, which inhibited the optical detection of the rovibrational ground state of WC. Nevertheless, I have learned a great deal about supersonic beams through the developing process in a continuous form, which eventually became very helpful when I moved on to create a pulse form of the supersonic beam, which will be described in chapter 3. In this chapter, we will discuss the main results from the continuous beam source, identify the limitations, and show some of the ideas to attack those problem.

2.1 Initial detection of chemistry

Before worrying about the rovibrational ground state population of WC molecules, we first had to make sure that we were getting the chemical reaction for the molecule. We had to check for both an efficient evaporation rate of tungsten, and the reaction probability of tungsten with a carbon agent, such as methane. These two factors were tested by using a scanning electron microscopy (SEM), and a residual gas analyzer

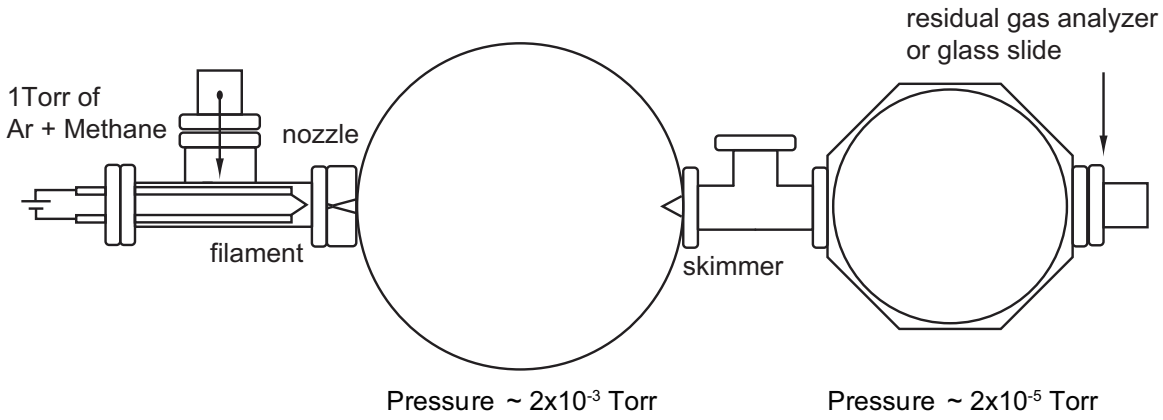

Figure 2.1: The initial design of the vacuum chamber to test tungsten evaporation rate and reaction of tungsten with carbon contained gas.

(RGA). The results were used to estimate the density of molecules being created under particular beam conditions.

2.1.1 Beam apparatus for mass spectroscopy

At the initial stage of the experiment, I designed a two stage pumping vacuum chamber shown in Fig. 2.1 using a tungsten filament as a beam source. Tungsten atoms are continuously evaporated from a resistively heated filament by passing a dc current through it. For a 6cm long filament with 5mm diameter, 6 Volts and 25 Amps heat the filament to a temperature of 3000 K. The final temperature T of the filament can be estimated from the final resistance R using the following equation,

$$R = R_0[1 + \alpha(T - T_0)], \tag{II.1}$$

where R_0, T_0 are initial resistances and temperatures, and the resistivity coefficient is α.

Close to the surface of the filament, we can estimate the evaporation rate of tungsten, $\frac{dm}{dt}$, at a given temperature by using Langmuir's formula [Lan13],

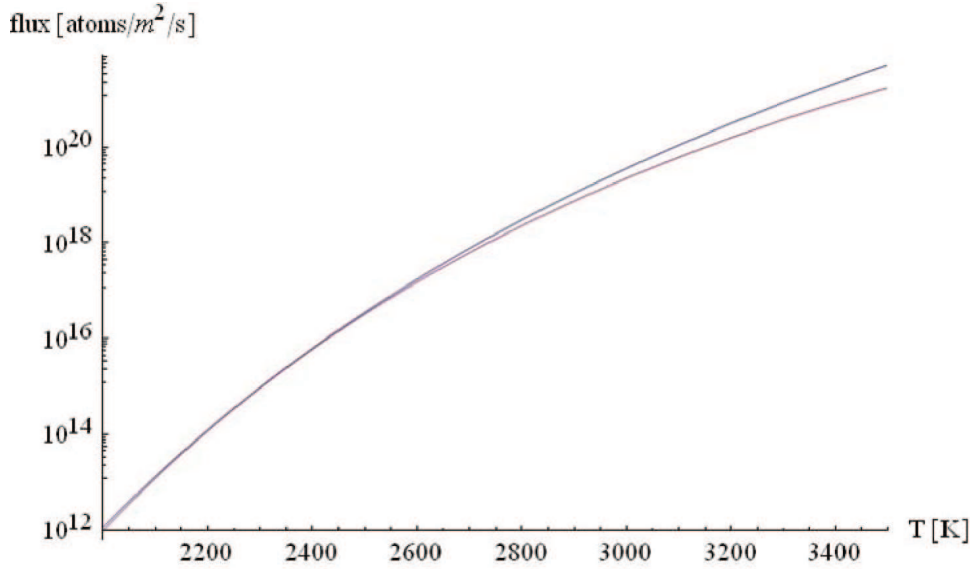

Figure 2.2: The plot shows the temperature dependant evaporation rate of tungsten. The blue curve uses the p coefficient valid in low temperature region(298K-2350K) and the red curve uses the high temperature coefficient valid in (2200-2500K).

$$\frac{dm}{dt} = p\sqrt{\frac{M}{2\pi RT}}, \tag{II.2}$$

where M is the molar mass, R is the gas constant, and p is an empirical coefficient. Figure 2.2 plots the evaporation rate of tungsten in the units of atomic flux at different temperatures. The exact coefficient of p at 3000K is not known, however, an order of magnitude estimate is possible from the high temperature coefficient curve of the plot, which gives 10^{19} tunsten atoms/m^2/s.

During the evaporation process, the filament was surrounded by 1 torr of argon buffer gas. Evaporation of Tungsten becomes suppressed in the presence of an inert gas [Fon28]. The evaporation process under gas pressure is described by a "Langmuir sheath", which is a sheath of gas molecules surrounding the surface of the evaporation source [Lan12]. Therefore there is a diffusion process of Tungsten atoms into this stationary gas film. Specifically, Matsuoka calculated the Tungsten evaporation rate

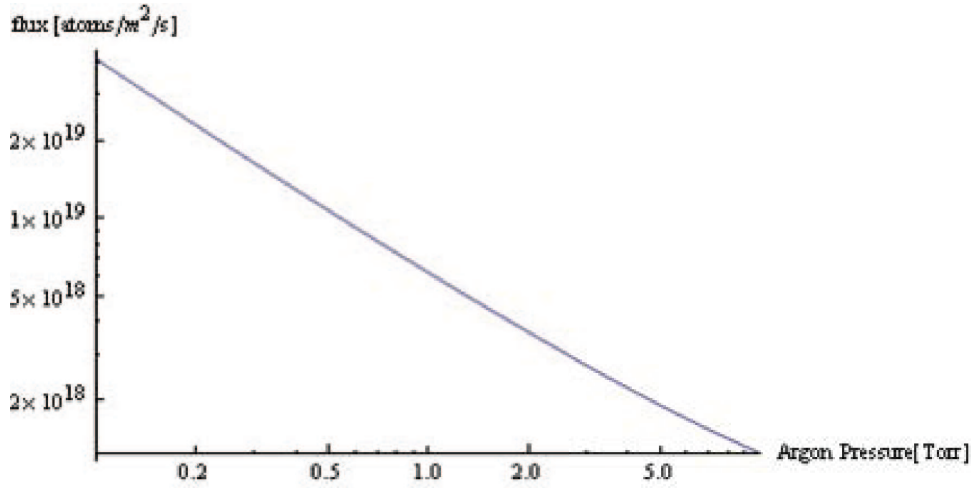

Figure 2.3: Pressure dependant evaporation rate of Tungsten atoms at 3000K in Log-Log scale.

under Argon pressure [Mat58]. Following his equation, we plot the pressure dependance of the evaporation rate of tungsten at the temperature of 3000K [Fig. 2.3].

With a given surface area of the tungsten filament, the evaporation rate under 1 torr of argon is $10^{15} atoms/s$. Typically, the total number of tungsten atoms evaporated from a single filament before it breaks is 10^{18}. A fraction of the tungsten atoms evaporated from the filament are entrained in a buffer gas jet that forms by passing through a converging diverging conical(half-angle 15 degree) nozzle with 1.5mm diameter at the throat and enters a vacuum region pumped by a turbo pump. The tungsten beam propagates about 20cm and reach a skimmer with 3mm diameter before it enters into the second high vacuum region with another turbo pump. A glass slide placed 30 cm after the skimmer collects the tungsten atoms for analysis. The deposited tungsten spot shown on Fig. 2.6(a) had a diameter of 6 mm and a thickness of 30 nm measured with a Profilometer, which corresponds to 5×10^{16} tungsten atoms. This is about 5% of the total tungsten atoms evaporated from a single filament. The composition of this thin film was analyzed by using scanning electron microscopy (SEM), which will be shown in the following subsection.

Converting the continuous tungsten atomic beam to a continuous tungsten carbide molecular beam can be accomplished by adding a small fraction of methane to the buffer gas. This allows for the chemical reaction $W + CH_4 \rightarrow WC + 2H_2$. One of the interesting aspects of this reaction is the fact that it happens not only in the gas phase of W atoms, but also at the surface of the W filament. The later reaction becomes a major issue for the case of high concentration of methane gas surrounding the W filament, as it creates WC and WC_2 layers at the surface of the filament, which eventually decreases the lifetime of the filament. This subject will be discussed in more detail in section 2.4.1.

2.1.2 SEM results

The glass slide with the thin film deposition was studied by scanning electron microscopy (SEM). The SEM machine produces a beam of electrons which interact with the atoms in the sample to produce a signal containing information of topology and composition. We have used the secondary electron scattering from the surface of the sample to achieve the image shown in Figure 2.4.

Tungsten carbide is known to crystalize in two different forms, one in hexagonal form and the other in cubic form [Wel84]. From Figure 2.4, we did not observe any of these forms. However, we were able to extract the atomic composition of the sample which is shown in Fig. 2.5. The figure shows the screen capture of the SEM analysis program with the result of composition inside the message box at the center. Figure 2.5 (a) reads, 8.7% Oxygen(O) and 91.3% Tungsten (W), and Figure 2.5 (b) reads, 9.66% Carbon (C), 8.51% Oxygen(O) and 81.83% Tungsten (W). A small fraction of oxygen was detected due to the sample being exposed to air after the deposition which causes the oxidation of the metallic film.

We were able to detect tungsten and carbon from the SEM, however, this was not a proof of gas phase reaction between tungsten and carbon, as the deposition process

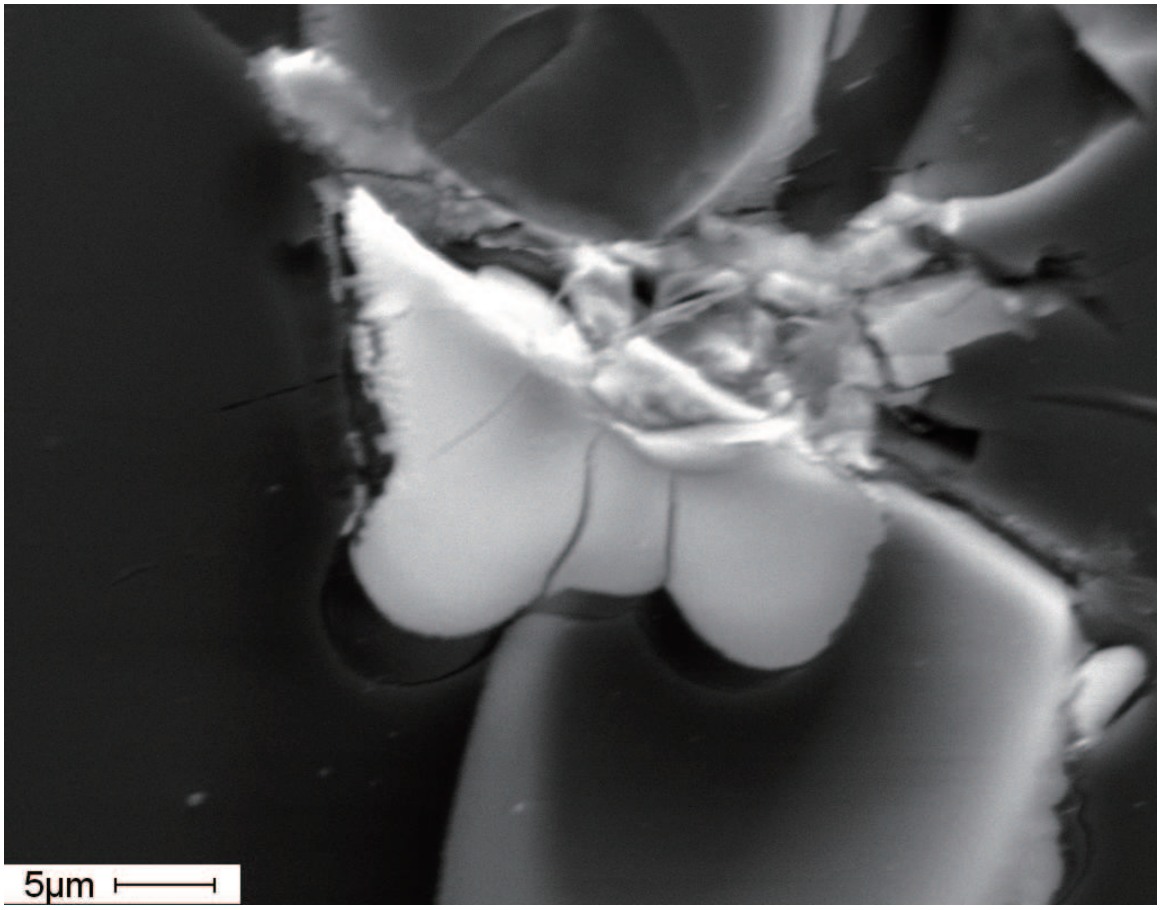

Figure 2.4: A SEM image taken with secondary electron emission from the deposition sample prepared by tungsten evaporation under methane gas.

(a)

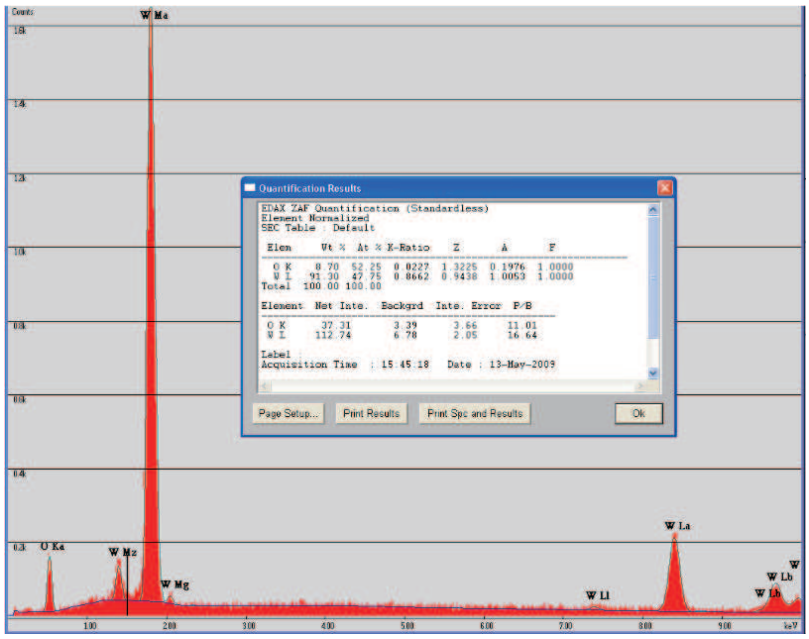

(b)

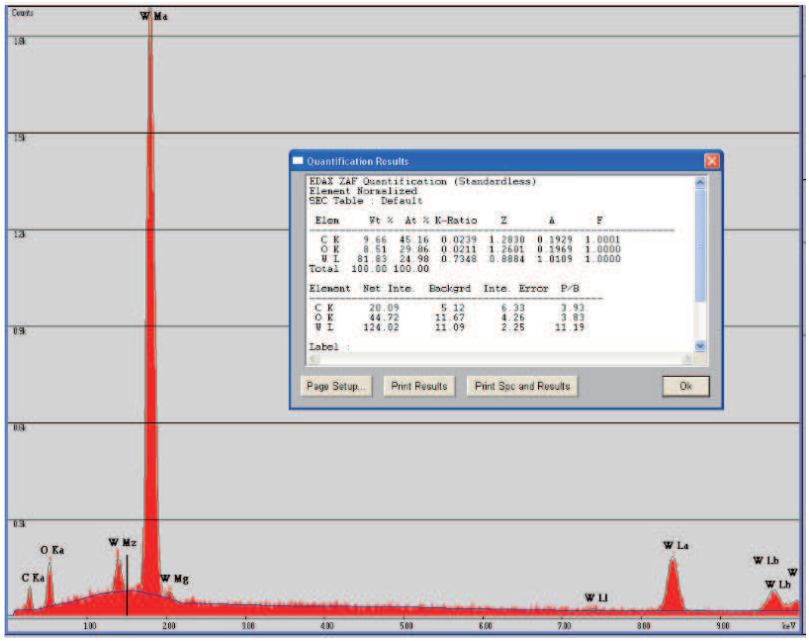

Figure 2.5: The SEM results with and without the methane gas present. As shown in (a), the thin film was mainly composed of Tungsten(W) with small fraction of Oxygen (O), due to oxidation of metal exposed to air. The deposition sample under methane gas present is shown in (b), which shows Carbon as well as Tungsten and Oxygen.

of each atom could have happened separately. More direct investigation of gas phase reaction is shown in the following subsection.

2.1.3 Mass spectroscopy: Study of gas phase reaction probability

In order to identify the tungsten carbide molecules in the gas phase, I installed the Residual Gas Analyzer (RGA) along the molecular beam line. The RGA is composed of an ionizer and a quadrupole electric guide. The ionizer is a thoriated tungsten filament with a current passing through it to produce electron emission, which is used for ionization of the surrounding gas. Once the gas is ionized, the quadrupole electric guide acts as a mass selective filter which only allows to enter certain ions at specific voltage conditions. And by scanning this voltage, we get a mass spectrum of the gas entering the RGA.

Figure 2.6 shows the result of the mass spectrums of both W and WC. In Fig. 2.6(b), we see clearly resolved 4 abundant isotopes of tungsten, which are ^{182}W, ^{183}W, ^{184}W, and ^{186}W. A fraction of W atoms would go through reaction with the methane gas to produce WC, which gives us a single broad peak ranging from 194 AMU to 198 AMU shown in Fig. 2.6(c). These are 4 unresolved peaks of ^{182}W^{12}C, ^{183}W^{12}C, ^{184}W^{12}C, and ^{186}W^{12}C, as carbon has only one abundant isotope with 99% abundance. Comparing the peak height of W with WC, we estimate the reaction probability of 1.6%, which is equivalent to generating 1 WC molecule out of every 60 W atoms.

2.2 Design considerations for optical spectroscopy with continuous supersonic beam source

In the previous section, we have shown the results of WC mass spectrum to confirm the chemical reaction within the continuous beam source. Our next step was to use laser induced fluorescence (LIF) spectroscopy for the detection of rovibrational

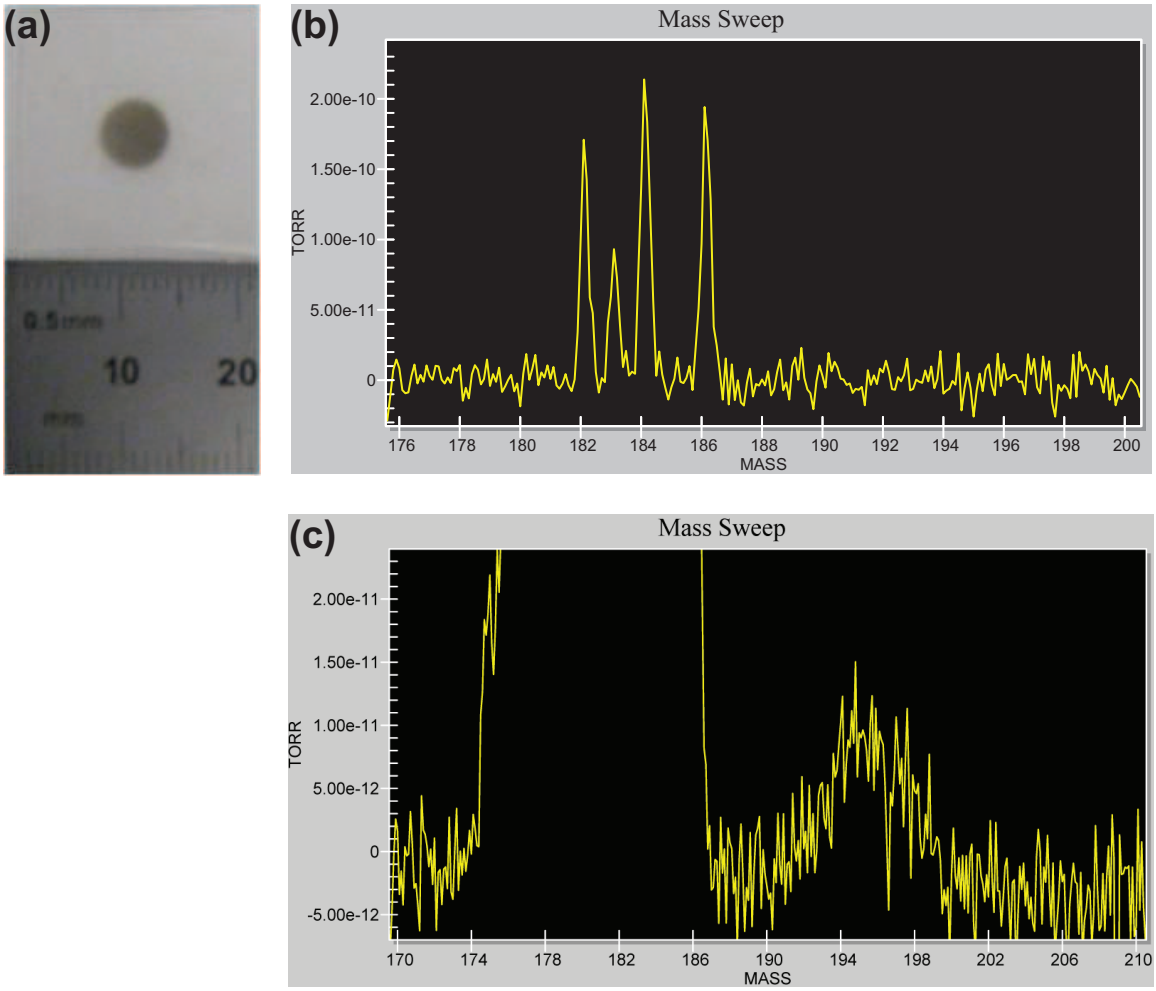

Figure 2.6: (a) Tungsten atoms sputtered onto a glass slide placed $\sim$ 30 cm downstream from a 3 mm diameter skimmer. (b) and (c) Quadrupole mass spectra of tungsten atoms (masses 182, 183, 184, & 186 amu) evaporated from a resistively heated tungsten filament in vacuum and tungsten carbide molecules (masses 194, 195, 196, & 198 amu) formed by resistively heating a tungsten filament in the presence of an argon + methane buffer gas.

ground state WC molecules, where the measurement of electron EDM would take place. There were several additional design considerations that we had to take into account for the optical detection of WC, which required modification of the continuous beam apparatus shown in Fig. 2.1.

In principle, one only needs to add a photo-multiplier tube (PMT), photon counter, and the probe laser that would cross the molecular beam. However, many more changes were gradually made based on things we have learned along the way. Here we will summarize all the problems that came up, and how we modified the apparatus to overcome those issues.

2.2.1 Cooling design: heat capacity considerations

The biggest issue was related to the cooling power of the continuous supersonic beam. The internal temperature of the WC molecules was not a relevant parameter for the mass spectroscopy, however, optical detection of the WC rovibrational ground state is closely related to how low the rotational and vibrational temperatures are. The hotter the molecule is, more of the higher lying rovibrational quantum states get populated, and only a small fraction of the molecules are left in the rovibrational ground state.

First we need to understand how supersonic expansion works. Supersonic expansion is achieved when a high pressure gas goes through a small orifice and expands into vacuum. During the process, the gas accelerates to overcome the local speed of sound, and both external and internal degrees of freedom cool down [GF74]. In general, cooling of the gas happens when it loses its thermal energy, which is only possible by either transferring it to another system or converting it to a different form. Therefore we can simplify any cooling process by combinations of "energy transfer" and "energy conversion".

The energy transfer process can be easily understood as dipping a hot object into

a cooling bath. If the bath has high enough thermal conductivity, the object would reach a temperature close to the bath temperature. There could also be different layers of cooling baths, where the primary cooling bath surrounds the secondary cooling bath in order to cool the object in the center.

On the other hand, supersonic expansion converts the thermal energy of the gas into direct kinetic energy of its own. Closer to the throat of the nozzle, the collision rate increases due to higher density of gas molecules, which also increases the energy conversion process. After expanding into vacuum, the collision rate decreases rapidly and the molecules fly out as a beam with lower thermal energy. This non-equilibrium process causes different degrees of freedom to have different temperatures [Weg74].

In reality both of these process occur within the nozzle source as shown in Fig. 2.7. Hot seeded species would first thermalize to the colder buffer gas temperature, and then eventually the thermal energy would get converted to forward kinetic energy. The energy transfer process of gas thermalization is dominant far away from the throat of the nozzle, and the energy conversion process of supersonic expansion gets more efficient at the high density region closer to the throat.

When creating WC molecules, the main problem comes from the tungsten filament source dissipating 150 Watts of power, which would heat up the walls of the nozzle. The temperature of the nozzle measured by a thermocouple went up to 600K after complete stabilization. The buffer gas would heat up from the nozzle wall, and eventually increase the seeded WC gas temperature as well. In other words, the energy transfer process shown in Fig. 2.7 was hurting us. To turn this around, we had to figure out a way to cool down the wall of the nozzle to balance out the heat coming from the filament. Our design had a multiple loop of copper pipe that would surround the nozzle as shown on Fig. 2.8, carrying water to cool the walls down to room temperature level. The effect of nozzle temperature on the translational temperature of tungsten atoms will be shown in subsection 2.3.2.

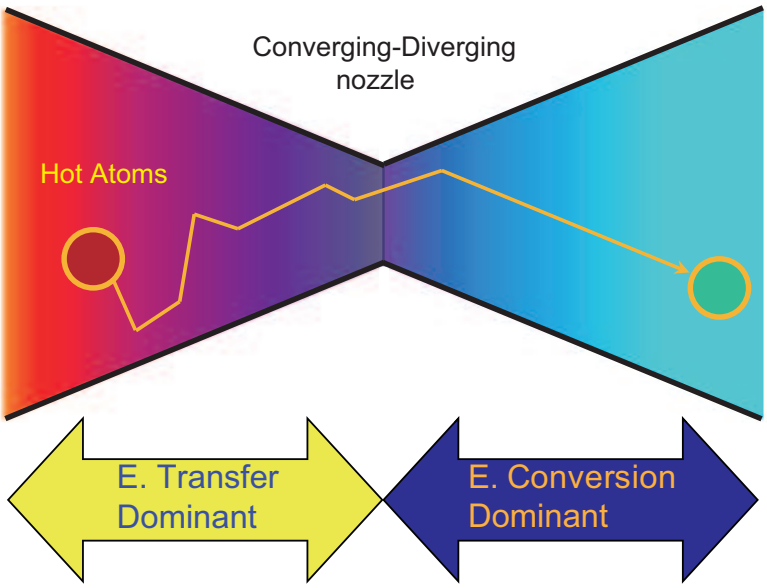

Figure 2.7: Diagram of energy transfer and energy conversion effect within the converging diverging nozzle.

2.2.2 Vacuum design: pumping capacity considerations

The second modification we made was based on insufficient pumping capacity of the continuous supersonic beam, which was limiting the mean free path of the molecules. The mean free path (MFP) of the molecules can be written as [Lid09],

$$MFP = \frac{k_b T}{\pi\sqrt{2} P d^2}, \tag{II.3}$$

where k_b is the Boltzman constant, T is the temperature (K), P is the pressure (Pa), and the molecules are treated as hard spheres of diameter d (m). With a given molecule under fixed temperature, the MFP inside each of our chambers is inversely proportional to pressure. With 1 Torr of argon gas passing through the nozzle, the MFP's can be calculated inside each vacuum chamber of our apparatus under fixed pumping capacities. The diagram showing different MFP's in different pressure zones of our previous beam source is illustrated in Fig. 2.9(a).

The MFP of the pre-expansion gas shown in the pink zone of Fig. 2.9 was con-

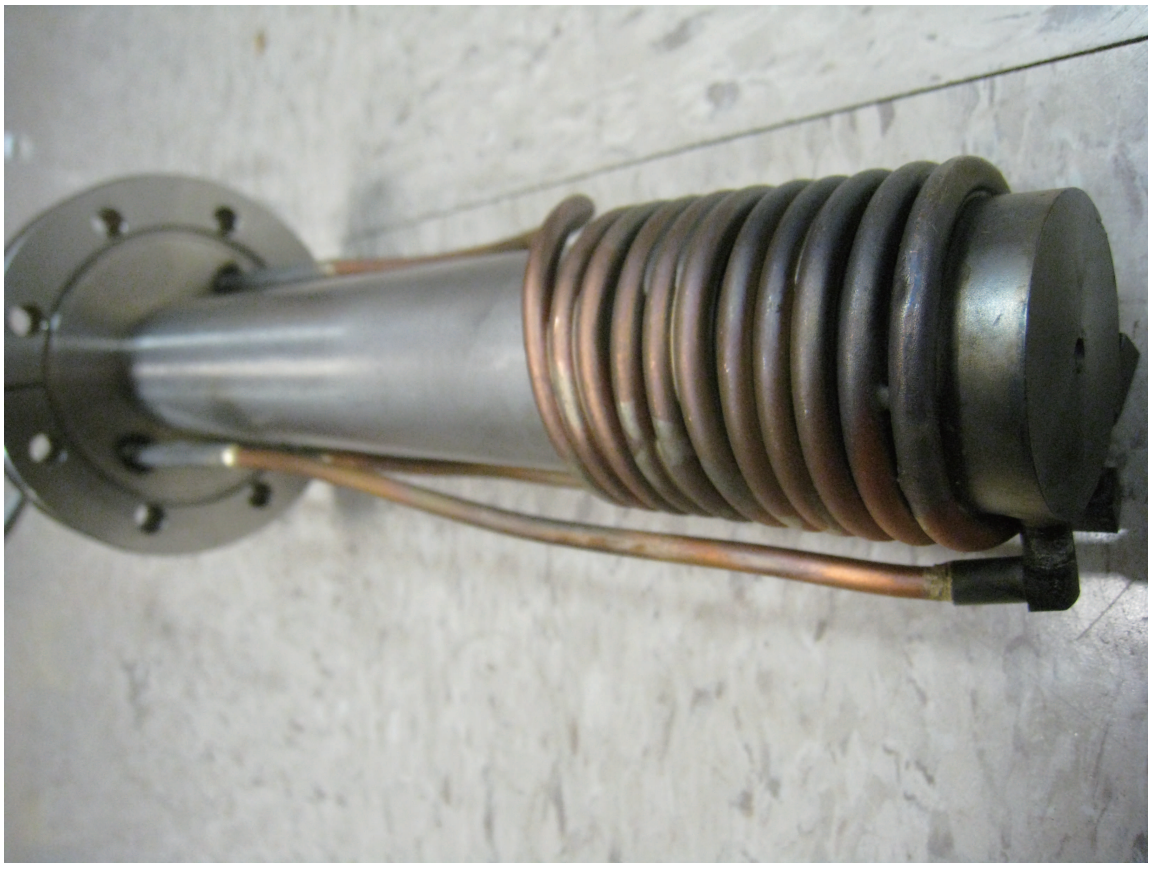

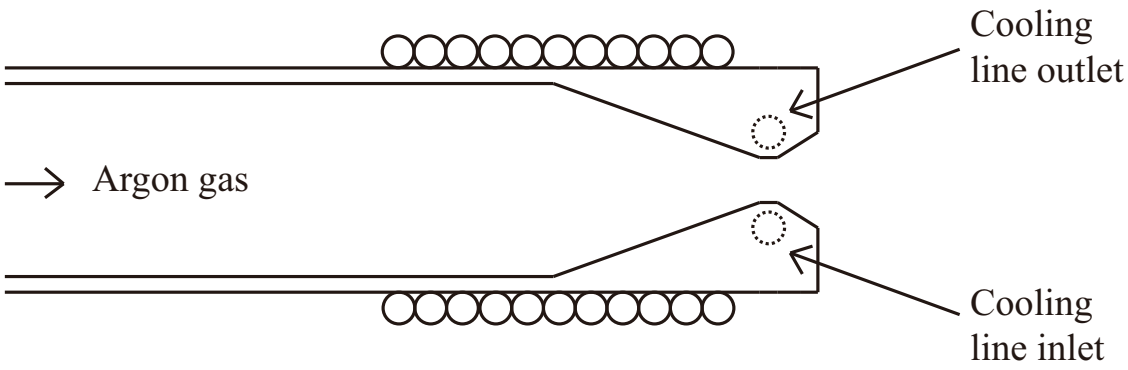

Figure 2.8: Diagram of water cooling system.

strained by the minimum buffer gas pressure for the supersonic expansion to work, which is to make the MFP much smaller than the nozzle diameter [Weg74]. For our case, argon buffer gas pressure had to be 1 Torr, which corresponds to 50 microns of MFP, and the condition is satisfied for a nozzle diameter of 1.5mm. The MFP of the following green(blue) zone is determined by equation,

$$C \times P = L \times P', \tag{II.4}$$

where C is the conductance of the nozzle(skimmer), L is the pumping speed in the green(blue) zone, P is the pressure in the pink(green) zone, and P' is the pressure in the green(blue) zone. This is essentially a mass conservation equation where the influx set by the conductance of the orifice has to be equal to the out-flux set by the pumping speed of the exhaust chamber. Due to the limited pumping capacity, the MFP of the green zone was much shorter than the nozzle-skimmer distance. As a result, we were losing a high fraction of the molecular beam flux. We wanted to reduce the nozzle-skimmer distance to fix this problem, which required a different nozzle design. Figure 2.9(b) illustrates the new design for the nozzle that would extend into the vacuum chamber, which reduces the nozzle-skimmer distance, resulting in a higher molecular flux to transmit.

2.2.3 Signal to noise: Nozzle and beam source geometry considerations

This subsection will describe a design consideration that is specific to the tungsten beam. As I was using a resistively heated filament to evaporate tungsten, there was black body radiation producing millions of background photon counts per second, which becomes a huge noise source in optical spectroscopy. We were using 6V and 25A for the heating, which is equivalent to having a 150 Watt light bulb inside your vacuum chamber when you are looking for a tiny resonant light emission from an atom.

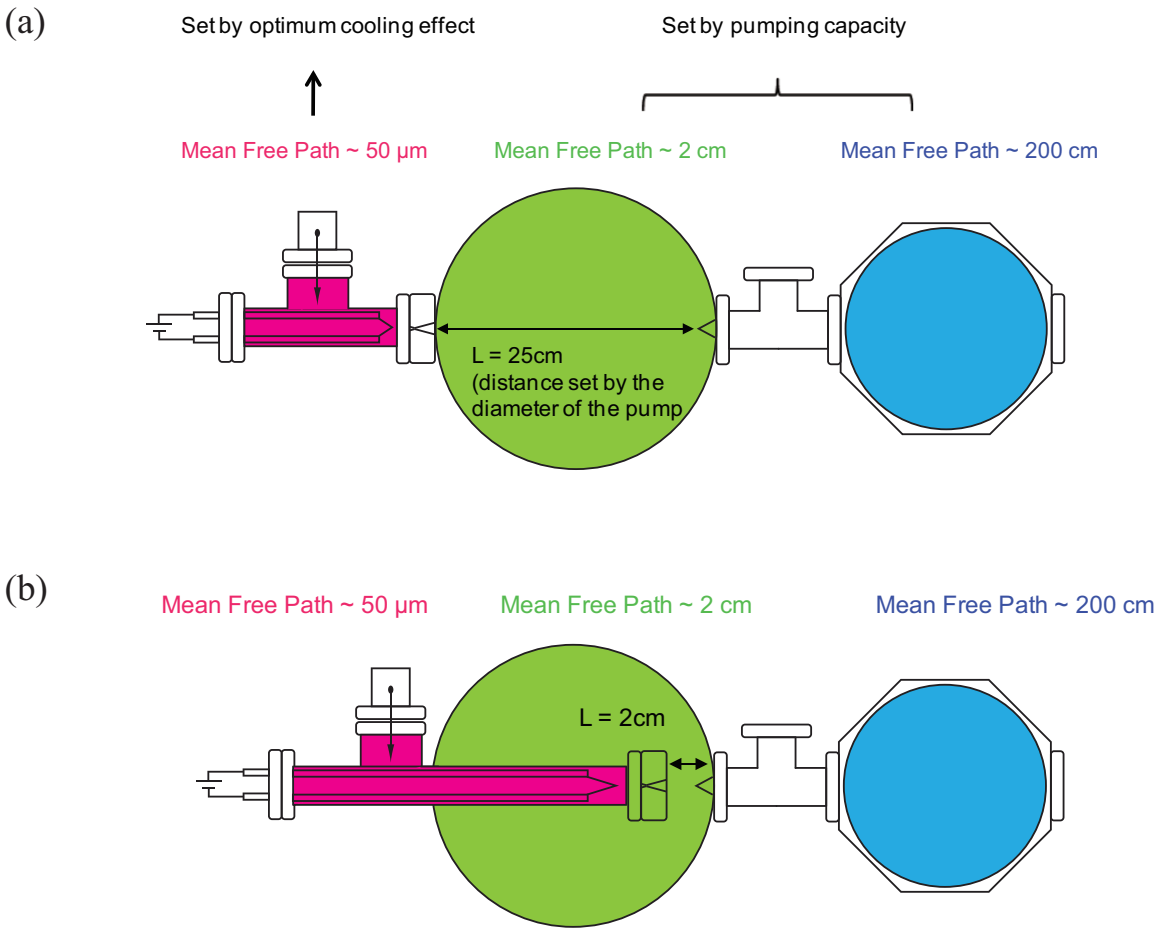

Figure 2.9: (a) Mean free path of continuous supersonic beam in each pressure zone for the previous beam apparatus (b) Mean free path of continuous supersonic beam in each pressure zone for the modified beam apparatus.

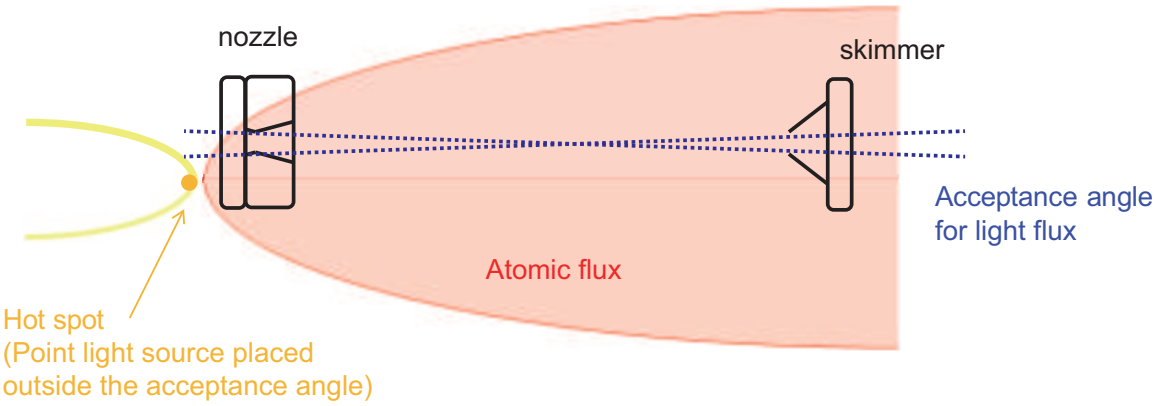

Figure 2.10: Illustration of difference in atomic flux and light flux propagation.

We resolve this problem by utilizing the fact that atoms are moving preferentially in the forward direction, while the light flux is being emitted radially. One could think of the tungsten atom's movement inside the buffer gas as a diffusion process in a forward moving frame. Therefore, by placing the filament outside the acceptance angle created by the nozzle orifice and the skimmer, the light background would be greatly reduced, while there would still be a considerable amount of atomic flux passing through. The illustration of this process is shown on figure 2.10. The key experimental trick was to bend the filament into a V-shape, where the tip would become effectively thinner with less electrical resistance. As that point would also become a hot spot which glows the brightest with the most amount of atomic flux coming out, the technique described in Fig. 2.10 becomes applicable. This was an important step for enhancement of signal to noise for LIF spectroscopy with the tungsten filament, where the background went from millions to ∼1000 photon counts per second.

There was an additional problem to solve, in terms of how far the filament has to be from the throat of the nozzle. The general rule of the filament being outside the acceptance angle shown on Fig. 2.10 should be kept for all cases, however, the distance between the filament and the nozzle was another optimization problem. When the

filament is too close to the nozzle, one might get enough flux coming out of the nozzle, but the tungsten atoms would not get enough number of collisions to cool down. If it is too far, the cooling effect would be enough, however, we would lose a considerable amount of atomic flux due to diffusion. The optimization point is where we get the highest atomic flux extraction with enough number of collisions for cooling.

First, we could calculate the number of collisions required between tungsten(W) and argon(Ar) buffer gas in order to reach a tungsten temperature of T [RVK09],

$$N = -\kappa \ln \left[\frac{T - T_{Ar}}{T_i} \right], \tag{II.5}$$

where $\kappa = (m_W + m_{Ar})^2/(2m_W m_{Ar})$, T_{Ar} is the buffer gas temperature, and T_i is the initial temperature of tungsten. For example, if we want to cool down the initial temperature of tungsten atoms at 3000K to within 1% of the argon buffer gas temperature at 300K, we get N$\sim$24. This converts to $\sim$1mm of distance when we have a MFP of 50 micron at argon pressure of 1 Torr. We will define this distance as the cooling length, and the location of the filament needs to be at least further away than this distance.

On the other hand, we need to consider how close the filament has to be in order to extract the most amount of atomic flux. This has to do with balancing the diffusion time constant with the supersonic time constant as shown on Fig. 2.11. In the figure, we have defined two time constants. The diffusion time constant T_1 is defined as the time it takes for the evaporated tungsten atoms to diffuse into the buffer gas, forming a sphere with radius r. The supersonic time constant T_2 measures how long it takes to pump out the volume enclosed in red lines in Fig. 2.11. We basically want to pump out the enclosed volume before the tungsten diffuses into a sphere with bigger radius than the radius of the nozzle aperture. We define the nozzle transmission factor T_1/T_2, and by setting this to 1, we can get the furthest filament-nozzle distance before we start losing atomic flux.

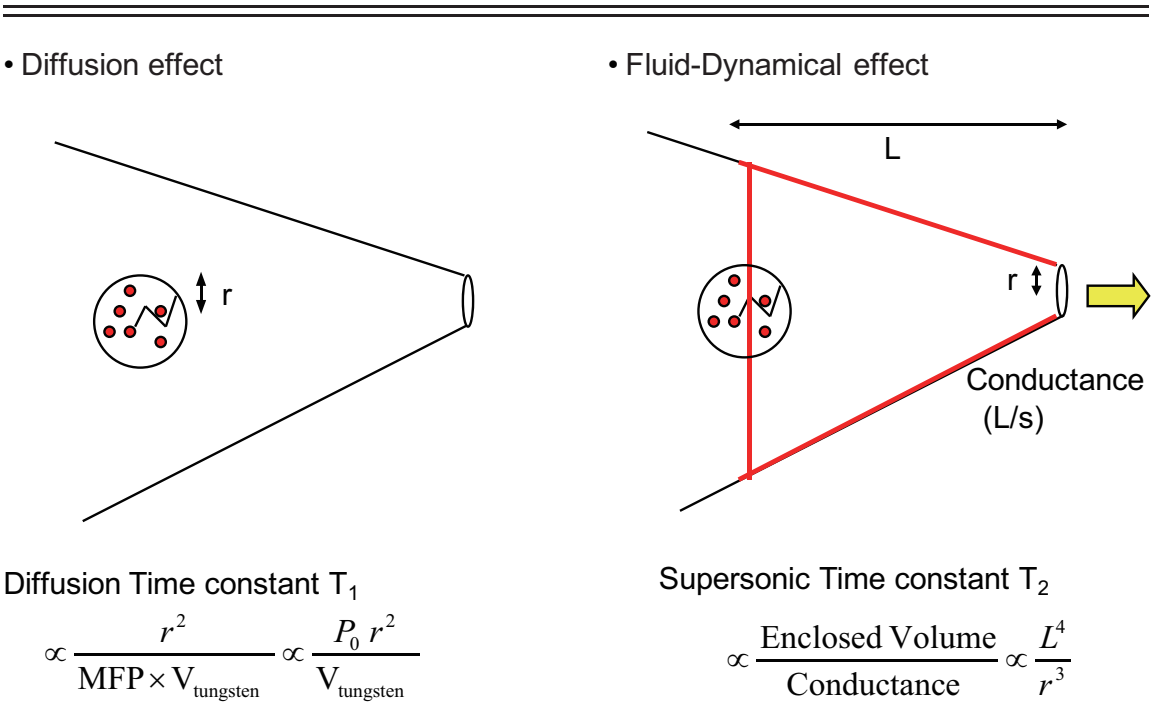

Figure 2.11: Diagram with definitions for diffusion time constant and supersonic time constant, which were used for calculation of nozzle transmission factor.

In our case, this distance with nozzle transmission of 1 was calculated to be 1.4mm, using the thermal velocity of tungsten at 3000K under 1 Torr of argon pressure with nozzle diameter of 1.5mm. Therefore combining this with the cooling length condition gives [1mm $<$ filament-nozzle distance $<$ 1.4mm]. The calculation gave us a certain range for the optimal distance, and further optimization was realized experimentally with W optical spectroscopy.

2.2.4 Modified apparatus for optical spectroscopy of continuous supersonic beam

Taking all the above modifications into account, we show a photo of the final version of the modified chamber in figure 2.12. This continuous beam source produced a high density, low divergent, and translationally cold W beam, which was a precursor for the WC beam. The laser induced fluorescing light was collected by a spherical lens into a PMT(Hammamatsu), which was connected to the photon counter, and the photon counts were recorded simultaneously as the wavelength meter(High Finesse WSU series) measures the frequency of the probe laser with an accuracy level of few MHz. The results of W optical spectroscopy under various experimental conditions will be shown in the next section.

2.3 Optimization of continuous supersonic beam from tungsten spectroscopy

In this section, we will show how we use optical spectroscopy of W atoms as a precursor for WC spectroscopy and also as an optimization tool for various supersonic beam parameters. From section 2.1.3, we have learned that about 1% of the tungsten atoms react with the methane gas to create WC. This means that one could roughly estimate the density of WC molecules in the system based on the atomic density measurement of tungsten under the methane gas pressure. As an accurate tungsten atomic density measurement, we used laser induced fluorescence (LIF) spectroscopy. Laser spectroscopy can also map out the velocity distribution of atoms from the Doppler effects of the fluoresced light. We use this information to optimize the supersonic beam.

During the supersonic expansion process, the internal temperature of the atoms cool down, therefore more of them would be in their electronic ground state. We have

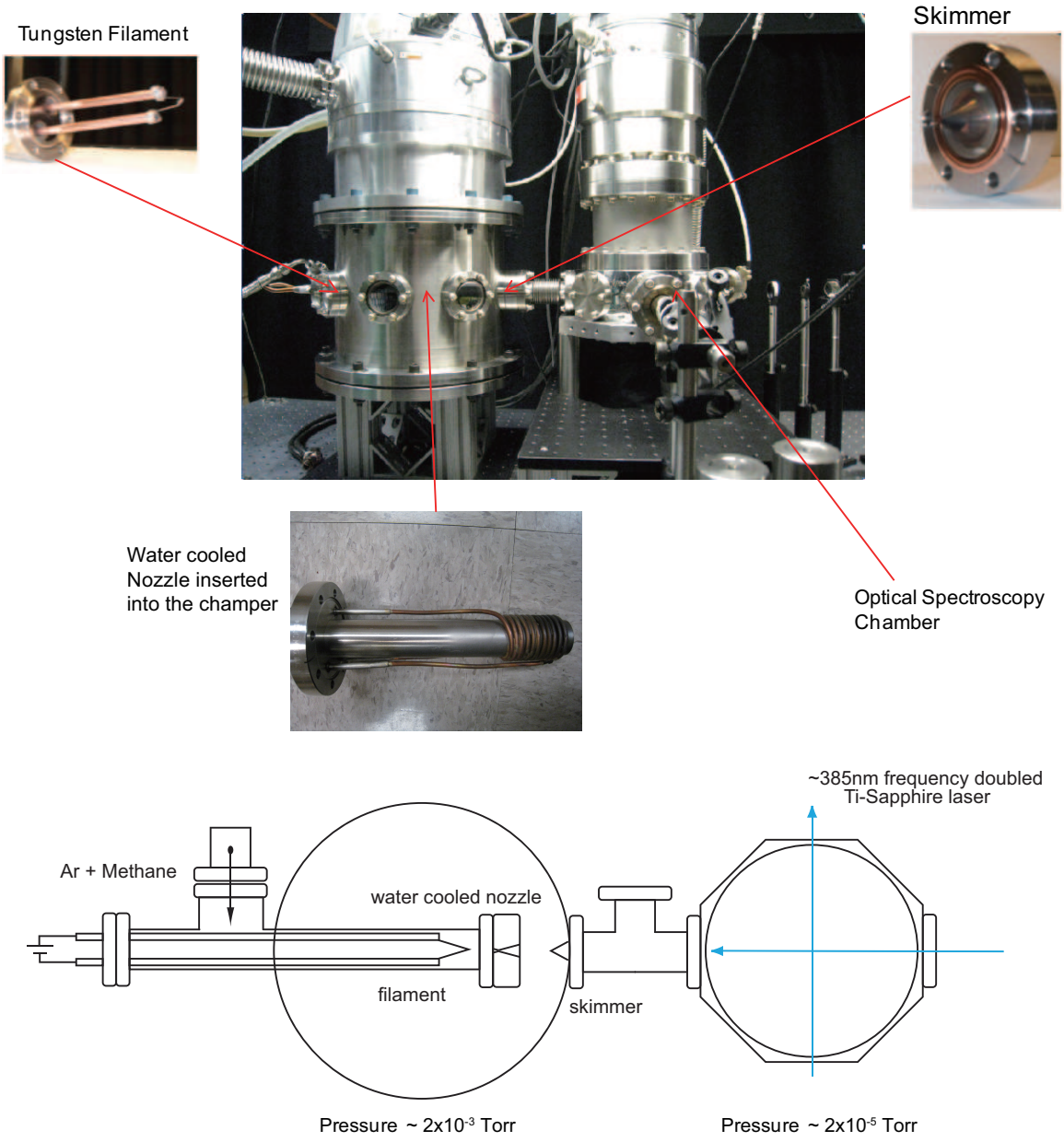

Figure 2.12: The photo of our modified continuous supersonic beam source for optical spectroscopy.

chosen to study the ${}^5D_0 \rightarrow {}^5F_1$ transition of tungsten at 385nm, as it was the strongest known transition to detect the ${}^5D_0$ electronic ground state [Wya10]. Throughout this section, we will only focus on extracting the tungsten supersonic beam properties from the optical spectra, and leave the isotope shifts and hyperfine structure analysis of the ${}^5D_0 \rightarrow {}^5F_1$ transition for chapter 3. The effects of experimental parameters such as the buffer gas species, stagnation pressure, and stagnation temperature will be shown.

2.3.1 Buffer gas species dependent beam properties

First question one needs to ask for the buffer gas cooling process is what buffer gas species to use. The most obvious choices are in the noble gas group, as their low chemical reactivity would inhibit reactions between the buffer gas and the seeded species. Within the noble gas group, further selection process is based on what the purpose of the experiment is. Going back to our discussion about frequency resolution of Ramsey spectroscopy in Chapter 1, longer coherence time and faster rate of measurement give better frequency resolution. Longer coherence time is related to how fast the atoms travel through the interaction region, which could be measured from the Doppler shift in axial LIF profile of the atomic beam. Faster rate of measurement is basically the detection rate of WC molecules in their rovibrational ground state, which is proportional to both W atomic density and cooling efficiency of the supersonic beam. However, as seen from eq. I.2, the $1/\sqrt{\dot{N}}$ dependence is not as attractive as the $1/\tau$ dependence. In other words, improving $\dot{N}$ by a factor of 10 would only increase the frequency resolution by a factor of 3, while the same factor of 10 improvement on τ gives factor of 10 better frequency resolution. Therefore, our main focus was to pick a buffer gas species that would give us a slower supersonic beam.

Here we compare tungsten supersonic beams created from two of the buffer gas

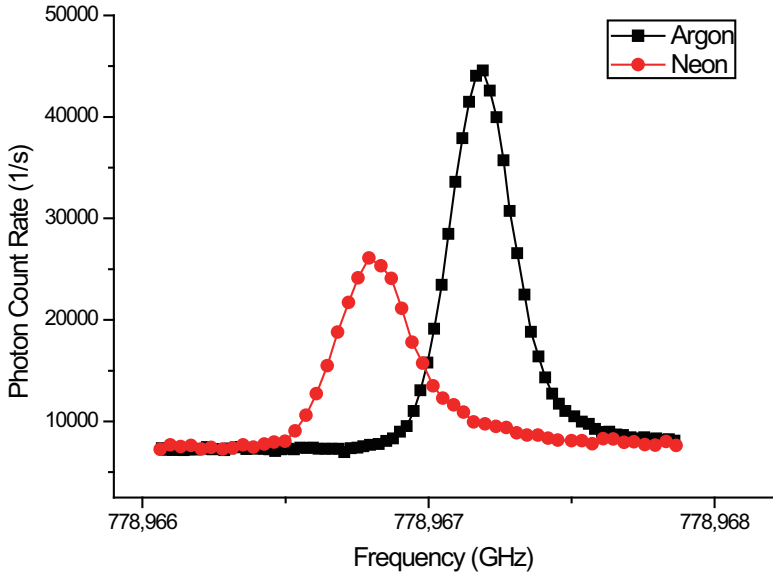

Figure 2.13: Axial tungsten LIF measurement for neon and argon buffer gas.

species of neon and argon. Helium gas was rejected as there is a large difference in mass between helium and tungsten, which would reduce the efficiency in momentum transfer of the cooling process. The test of krypton and xenon gas was put on hold due to much higher price. As we wanted to measure the axial tungsten atomic beam velocity, we let the probe laser to counter propagate with respect to the atomic beam direction and collect the Doppler shifted LIF photons with a PMT using the apparatus shown in Fig. 2.12. As the Doppler shift in frequency becomes negative in this case, higher axial bean velocity would push the axial LIF line center to the lower frequency side. The resulting frequency dependent photon counts of W spectra using 100Torr of neon and 1Torr of argon buffer gas sources are shown in Fig. 2.13. The pressure being used were determined by taking the MFP of each chamber into account, which were discussed in subsection 2.2.2.

From Fig. 2.13, we immediately noticed that argon buffer gas had a better tungsten extraction rate than the neon buffer gas, resulting in a stronger W transition line. We can also qualitatively tell that argon buffer gas produced a slower beam than the neon gas, indicated by less amount of Doppler shift toward the lower frequency side.

Combining these two factors, argon was the better choice than neon for our purpose of the electron EDM experiment. For better calculation of the axial beam velocity, one needs an extra piece of information from the LIF spectroscopy in perpendicular laser beam direction with respect to the atomic beam direction, which would give the zero Doppler shift position of the W transition line. A more quantitative description of these Doppler shifts will be shown in subsection 2.3.3.

2.3.2 Stagnation pressure and temperature dependent beam properties

The usual way of mapping out the three dimensional velocity distribution in an atomic beam with cylindrical symmetry is to perform laser spectroscopy in the parallel and perpendicular directions with respect to the beam propagation direction. The parallel and perpendicular laser beams would each probe the axial and radial velocity distribution of the atoms. Before getting into the effects of stagnation pressure and stagnation temperature, we will point out a particular difference between axial and radial velocity distributions for our case.

In general, the velocity distribution of atoms follow the Maxwell-Boltzmann distribution, which would represent the translational temperature of the system. There is an exception for this case, when there is a skimmer in use. As shown in Fig. 2.14, when the skimmer is placed along the atomic beam line for collimation of the beam, it selects out a narrow slice of the radial velocity distribution around the center radial velocity. Therefore, the radial velocity distribution would always look narrower than the axial velocity distribution. This effect has nothing to do with the temperature of the system, as it purely came from geometric selection of radial velocity class. In other words, one could measure the radial velocity distribution from laser spectroscopy, but it would not give any information about the true translational temperature of the beam. Since the effect would not be present in the axial velocity distribution, we can only use the axial velocity distribution as the translational temperature measurement.

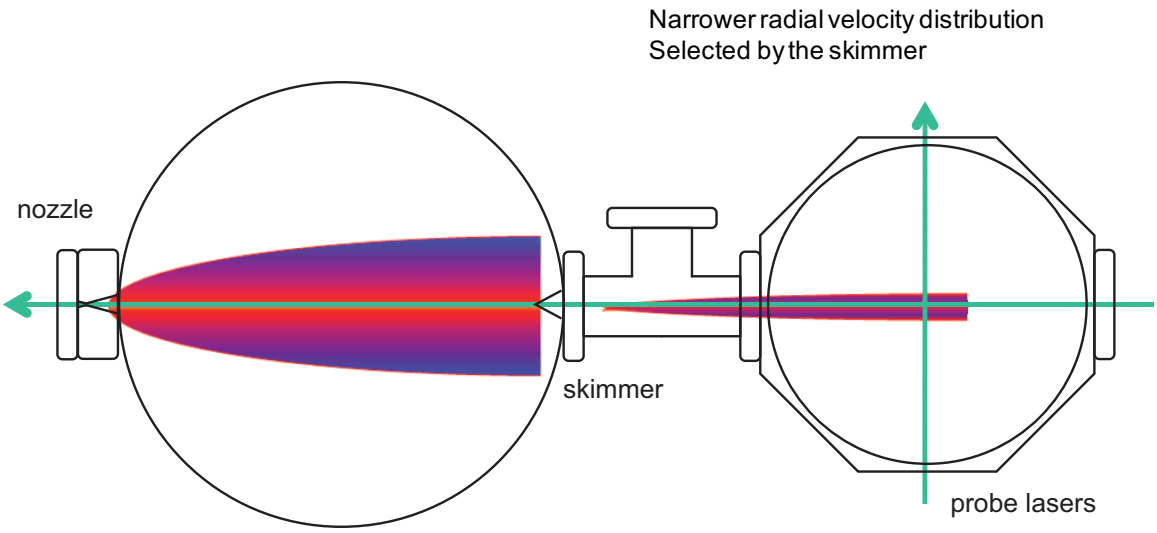

Figure 2.14: Diagram of the effect of skimmer on translational beam temperature measurement.

For the remaining part of the subsection, we will explain the optimization process of the supersonic beam. Following the above discussion about the axial LIF measurement containing the temperature information of the beam, we will limit our attention to axial measurements. There are three main pieces of information we could extract from the axial LIF measurement. The height of the measured line gives information about the atomic density, therefore we could use it as a measure of seeding efficiency of tungsten. The width of the line represents the translational temperature of the atomic beam, which allows us to use it as a measure of cooling efficiency. The third information comes from the Doppler shifted position of the axial LIF line center compared with the radial LIF line center, which is the measure of axial supersonic beam velocity. However, the axial velocity will not be considered as an optimization parameter, as there is a well defined fully boosted supersonic velocity for each buffer gas species under certain stagnation temperature [Weg74]. In some sense this was already optimized when we picked the gas species in the previous subsection. To summarize, we can monitor the axial LIF line profile to optimize both the seeding and the cooling efficiency. Since we want a cold intense beam of tungsten, we tune many experimental

parameters until we maximize the height of the line, while minimizing the width.

The seeding efficiency was controlled by filament-nozzle distance, where the optimized distance was calculated in subsection 2.2.3. As for the cooling efficiency, there were two different experimental knobs we tuned in the lab, and the effects of these are shown in Fig. 2.15. The first control comes from varying the argon buffer gas pressure. Higher buffer gas pressure gives more collisional cooling effect, where more thermal energy is transferred to direct kinetic energy in axial direction. By comparing the linewidths on Fig. 2.15(a), we see that this was indeed the case. The same plot also shows the subtle effect of higher axial velocity for higher buffer gas pressure, which is observed by the line center shifting to the lower frequency side for the higher pressure. The second control is on the temperature of the buffer gas. When the buffer gas temperature is lower, more thermal energy can be taken away from the seeded tungsten gas. We observed the obvious decrease in linewidth for lower buffer gas temperature which was shown on Fig. 2.15(b). Another noticeable effect was the decrease in axial velocity, which was due to decrease in total thermal energy of tungsten. This could also be understood as the energy transfer effect dominating over the energy conversion effect shown on Fig. 2.7.

Summarizing all the factors related to the electron EDM experiment, we want an intense, cold, and slow supersonic beam. We have seen the stagnation pressure and temperature mainly contributing to the cooling efficiency part. As for the stagnation pressure condition, we would increase the buffer gas pressure up to the point where we see the narrowest axial Doppler linewidth of the tungsten transition. If one continues to increase the pressure, the turbo pump would not be able to handle the gas load, and as the background gas builds up, one starts to see the axial Doppler linewidth getting wider. As for the stagnation temperature condition, everything is about how well one could design the cooling system for the wall of the nozzle. This would be an engineering problem taking flow rate and heat transfer rates into account.

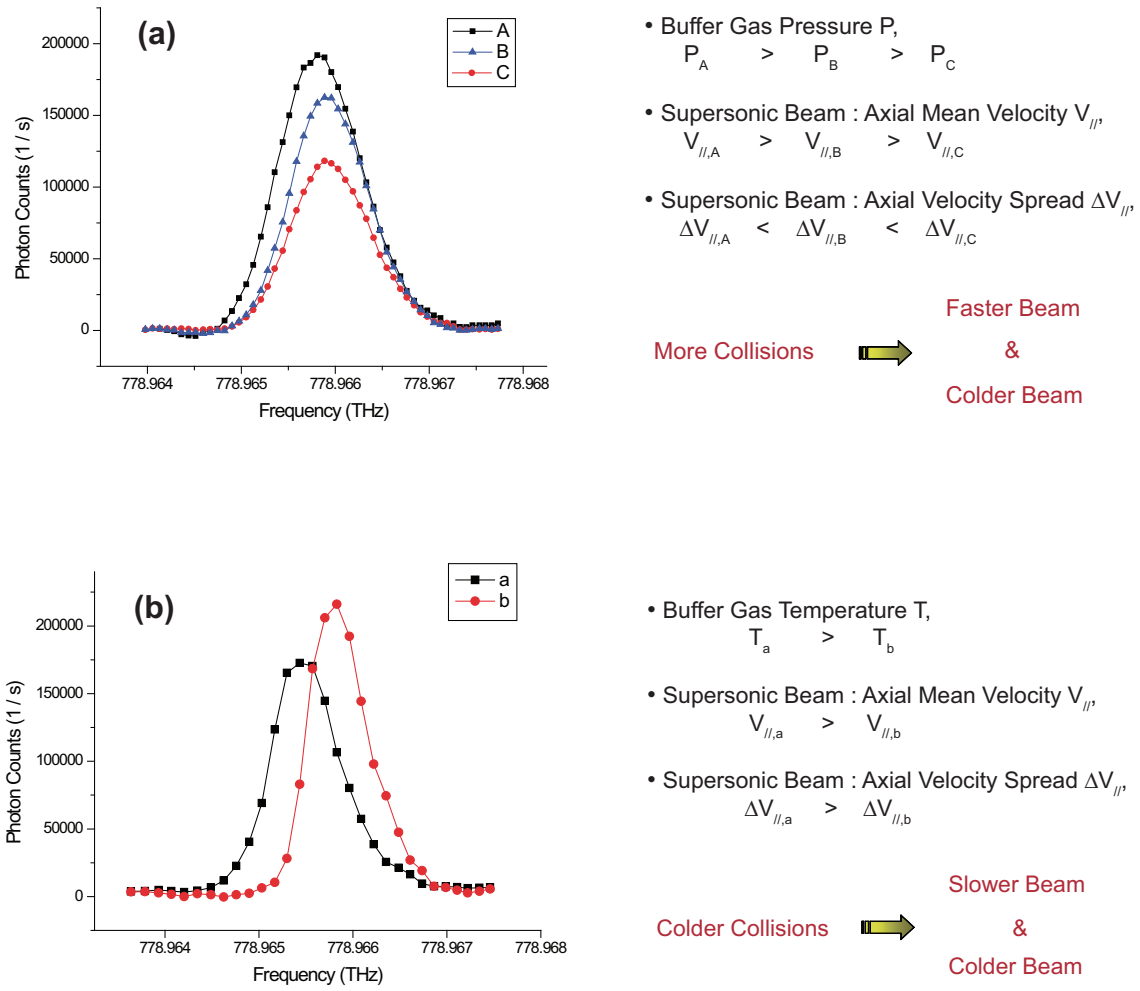

Figure 2.15: (a) Stagnation pressure dependent axial tungsten LIF profile (b) Stagnation temperature dependent axial tungsten LIF profile

2.3.3 Fully optimized W beam properties

Here we will show the fully optimized tungsten LIF spectroscopy results of two different cases of perpendicular and parallel laser beam direction with respect to the propagation direction of the atomic beam. The perpendicular laser beam would probe the radial velocity distribution of atoms where the line center would have zero Doppler shift as $\vec{k} \cdot \vec{v} = 0$, where $\vec{k}$ is the wavenumber of the photon and $\vec{v}$ is the velocity of the atoms. The Doppler broadened linewidth gives information about the radial velocity spread, which corresponds to the beam divergence. On the other hand, the parallel laser beam was counter propagating with respect to the atomic beam direction, showing the axial velocity distribution of tungsten atoms with the Doppler shifted line position measuring the axial mean velocity of the beam and the Doppler broadened linewidth representing the translational beam temperature. The radial and axial LIF spectra of fully optimized tungsten supersonic beam with argon buffer gas is shown in Fig. 2.16.

First we calculate the axial beam velocity to be 681m/s from the Doppler shift shown in Fig. 2.16. This corresponds to a buffer gas stagnation temperature of 450K, calculated from the equation for a fully boosted supersonic beam [Weg74],

$$v_{supersonic} = \sqrt{\frac{5}{2}\frac{2k_B T_0}{m}}, \tag{II.6}$$

where T_0 is the stagnation temperature and m is the mass of the buffer gas. This temperature was higher than the nozzle wall temperature, which was near room temperature from the water cooling effect. We believe the discrepancy is due to a temperature gradient between the temperature measurement point and the inner wall of the nozzle.

We could also extract the atomic beam divergence, $\delta v_{rad}/v_{axial}$, by converting the radial LIF Doppler linewidth into a radial velocity spread, δv_{rad}. The FWHM

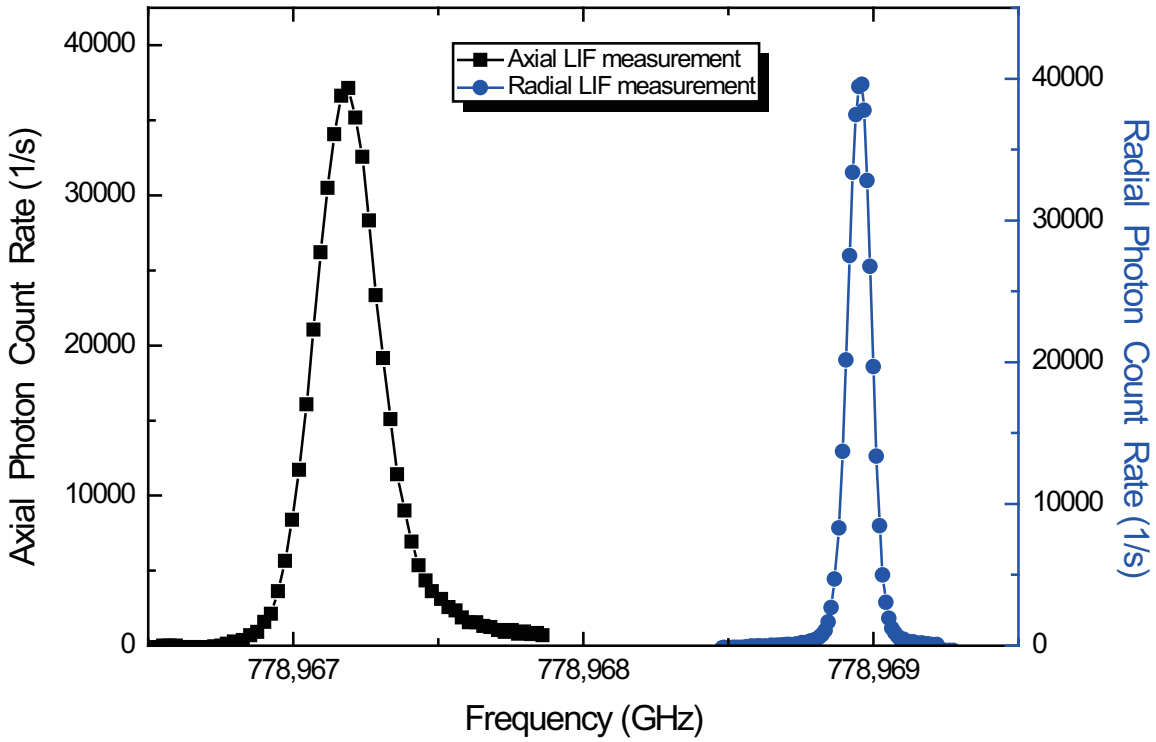

Figure 2.16: Laser induced fluorescence measurement of tungsten for axial and radial direction of the beam. We have subtracted out the background photon counts from both measurements for better comparison of height and shape.

linewidth of 93MHz was given by Gauss fitting the radial LIF measurement. From this, the radial velocity spread of 36m/s and the beam divergence of 0.05rad can be calculated.

On the other hand, the axial velocity spread measured from the axial LIF spectrum contains extra information of the translational beam temperature. As each of the frequency measurement from the LIF spectrum is actually a velocity measurement, one could fit the axial data with the following Maxwell-Boltzmann distribution function,

$$f(v_{axial}) = \sqrt{\frac{m'}{2\pi k_B T_{trans}}} \exp\left[\frac{-m' v_{axial}^2}{2k_B T_{trans}}\right], \tag{II.7}$$

where m' is the mass of the seeded species. Using the mass of tungsten, we get a translational temperature of 40K. As described in many literature [Weg74, Cam84], supersonic expansion cools down the rotational temperature equally well as the translational temperature. Therefore, this could be a good estimation of rotational temperature within a factor of 2.

As for the last relevant derived parameter, we will calculated the axial Mach number, which is defined as the ratio of axial beam velocity to the local speed of sound. Axial Mach number is often used as a good parameter to describe the performance of the supersonic beam. The following equation calculates the axial Mach number,

$$M = \frac{v_{axial}}{a} = \frac{v_{axial}}{\sqrt{\frac{5}{2}\frac{k_B T_{trans}}{m'}}}, \tag{II.8}$$

where a is the local speed of sound. From this, we calculate local speed of sound to be 67m/s, which gives an axial Mach number of $\sim$10. This is fully in the supersonic regime [Weg74], which is a direct proof showing that we have created a continuous supersonic beam of tungsten atoms.

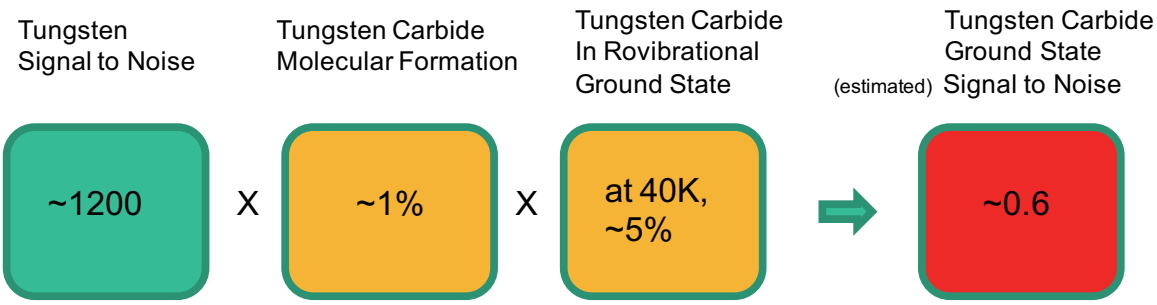

Figure 2.17: Flow chart for estimation of WC signal to noise level from W signal to noise.

2.4 Limitations and future directions of continuous supersonic beam

In the previous section, we have developed an internally cold and intense supersonic beam of W. Despite all the modifications described in subsection 2.2.4, we were not successful in optical detection of the WC rovibrational ground state with the continuous beam source. There were several remaining issues, and a chart of all the relevant factors are shown on Fig. 2.17. Based on the tungsten signal to noise level, we can roughly estimate the signal to noise level of WC using this chart. The chemistry part has been measured from the mass spectroscopy of subsection 2.1.3, and the fractional rovibrational ground state was estimated based on thermal distribution of molecules at the given rotational temperature. The numbers given here are just to estimate for the best case scenario, where we assume similar transition strength and background level for WC detection as for the W detection, and also project rotational temperature to be around the same level as the translational temperature. We start with an excellent signal to noise of 1200 for the W spectrum, however, two big hits from the chemistry factor and the cooling factor makes the WC signal to noise less than 1 even for the best case scenario. These limitations will be discussed in the following subsection, and a design proposal for the future generation continuous supersonic beam source will be presented in the last subsection.

2.4.1 Remaining limitations of the current continuous beam apparatus

There are several limitations of the current version of the continuous supersonic beam apparatus. As discussed in the previous subsection, two main factors that prevent us from detecting the WC rovibrational ground state are chemistry and cooling.

One could think of creating WC in vapor phase by either using acetylene (C_2H_2) or methane (CH_4) as the carbon agent, with the evaporation of tungsten [Pie92]. There were other vapor phase reactions studied, such as using tungsten hexachloride (WCl_6) [HOK78], tungsten hexafluoride (WF_6) [FS95], or tungsten hexacarbonyl ($W(CO)_6$) [KK04] for precursors, however, mainly for production of WC powders. Following the steps of the only previous optical study of WC [SSM02], we have chosen methane to react with tungsten. We have tried the photolysis technique [BLT83] as a way to enhance chemistry by exciting the W ground state $^5D_0$ up to the $^5F_1$ state with a 385nm CW laser. In this case, the photons are providing the energy required for the chemical reaction, however, we have not seen a noticeable enhancement effect. The study of enhancing the gas phase chemical reaction rate of WC would be a tough chemistry problem by itself, which is outside the field of our specialty, therefore will not be discussed here. Instead, we will describe one aspect of chemistry that hurts our system in a different way.

It turns out that methane not only reacts with the gas phase tungsten, but also reacts on a solid tungsten surface [Win75]. Fig. 2.18 describes how the reaction of methane on a tungsten surface could be an issue for the tungsten filament lifetime. As the WC deposition starts building up on top of the W filament, more current passes through the W core rather than the WC surrounding, which effectively makes the W filament thinner. When this process accumulates, there will be a thick outer layer of WC film within the filament, which would crack eventually due to the brittle nature of WC. The process takes about 1000 seconds to break the filament which severely limits the lifetime of the experiment. This was one of the major issues for optical

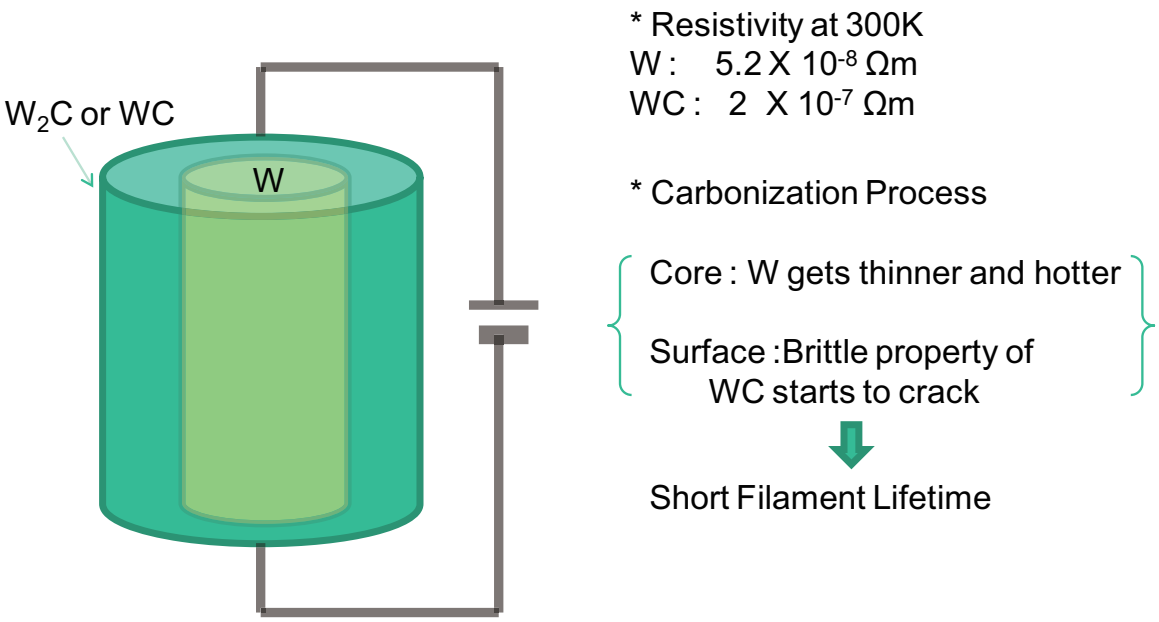

Figure 2.18: Diagram of the methane surface reaction on tungsten, which decreases the lifetime of the filament.

detection of WC rovibrational ground state as we could not use longer integration time for our frequency scans to reduce the noise level.

As for the cooling factor, we started from 3000K of hot tungsten atoms down to 40K of translational temperature, which shows a good amount of cooling, however, not enough for the purpose. In general, the cooling effect is known to improve with increasing P_0D [Sco88], where P_0 is the stagnation pressure and D is the nozzle diameter. Also, with a fixed pumping capacity one could prove that the nozzle flow rate is proportional to P_0D^2. With the previous two relations, we finally get,

$$\textbf{Cooling Effect} = P_0D \propto \frac{1}{D}. \tag{II.9}$$

This simple relation, first recognized by Camprague [Cam84], states that we could improve our cooling effect even at a fixed pumping capacity, just by decreasing the nozzle diameter. We will show a design proposal of micro-nozzle continuous supersonic beams in the following subsection.

2.4.2 Future direction for continuous beam apparatus

Here we will show a new design proposal for a continuous supersonic beam apparatus, incorporating the micro-nozzle idea. The design is shown in Fig. 2.19, where the discharge between two sharpened W pins is used as the evaporation method instead of the resistively heated filament. This is mainly to avoid the methane surface reaction issue which was limiting the lifetime of the filament source. The discharge source would be limited by a different factor, which is the sharpness of the W pin. As the whole purpose of the device is to evaporate tungsten at the tip of the pin, that point would eventually become dull, and the discharge will not be concentrated at the point. We would have to re-sharpen the W pin after a certain point. However, we believe the time scale of pin replacement would be much longer than the time scale of active methane coating killing the filament.

One of the technical difficulties was machining a small hole on a thin slice of boron nitride insulators. Boron nitride is one of the few machinable high temperature insulators, but it is extremely brittle [LSH89]. We were limited by our machining abilities to only get down to 150 microns of nozzle diameter. This is still a factor of 10 decrease in nozzle diameter, which was 1.5mm for the filament source. From eq. II.9, we expect an increase of cooling effect by a factor of 10, and also a big enhancement in the fractional rovibrational ground state of WC shown in Fig. 2.17. However, around this time we started building the second generation pulse supersonic beam source, which showed a lot of promise, so we eventually spent less amount of effort pursuing the proposed discharge continuous beam source. We will only leave the design proposal here, as a future direction for continuous supersonic beams of metallic carbides. There has been a similar proposal of discharge beam source used for different applications [CKM10].

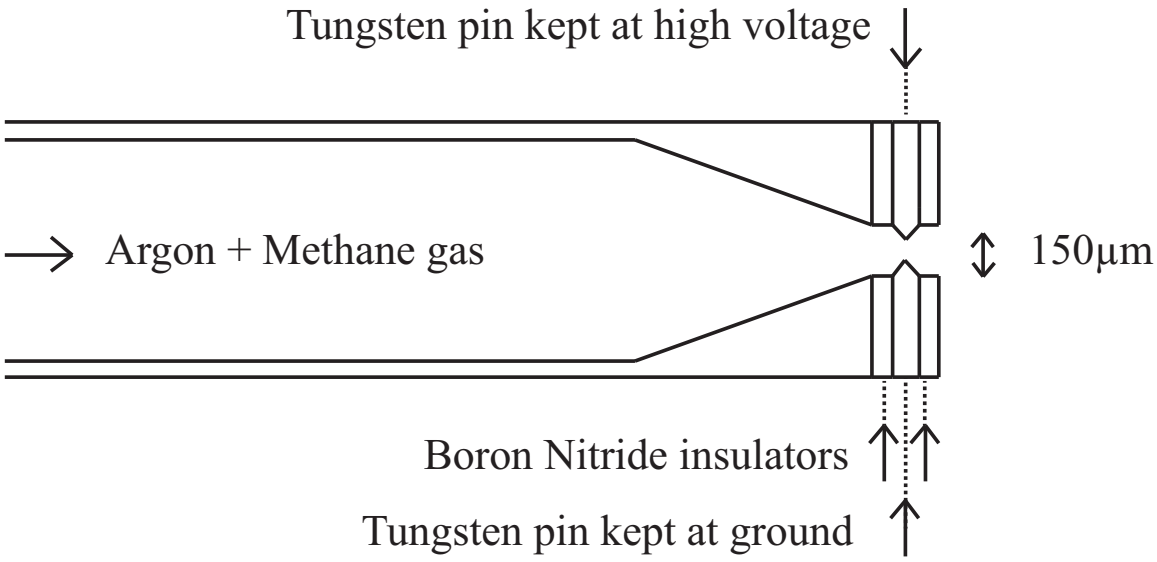

Figure 2.19: Sketch for W discharge continuous beam source.

CHAPTER III

Second Generation Experiment: Pulse Supersonic Beam Source Measurements

In the previous chapter, we described the first generation beam source, where we used a resistively heated tungsten filament to produce a high flux supersonic beam of tungsten. However, as shown in subsection 2.4.1, there were several limitations that did not allow us to optically detect the rovibrational ground state of WC. This chapter will show how we overcome these issues with a pulse supersonic beam technique [DDPS81], and successfully detect the WC rovibrational ground state through LIF spectroscopy. We will first give a brief review of the technique, and move on to show W and WC LIF spectra taken with the pulse supersonic beam apparatus.

3.1 Advantages of pulse supersonic beam source

The cooling effect of supersonic expansion is known to be proportional to the stagnation pressure [Sco88]. In subsection 2.4.1, we have discussed a way to improve cooling by using a micro nozzle. On the other hand, higher stagnation pressure could also be realized by a pulse form of supersonic beam. Hagena [Hag63] was the first to propose the use of magnetically controlled pulse nozzles. Along with the pulse nozzle technique, Smalley [DDPS81] integrated laser vaporization technique to create pulse

supersonic beams of metal clusters. This so called Smalley type pulse supersonic beam method has several advantages over the continuous beam method for creating a WC beam with low internal temperature.

The main advantage is the superior cooling effect coming from delivery of high stagnation pressure within the pulse. The highest stagnation pressure that a continuous supersonic beam source could deliver was set by eq. II.4. For the case of a pulse supersonic beam source [Sco88], a duty factor f gets multiplied to the left hand side of eq. II.4 to become,

$$f \times C \times P_0 = L \times P_1, \tag{III.1}$$

where $f = \rho\Delta t$ with the pulse repetition rate ρ and pulse duration Δt. Therefore, even with the same pumping capacity L, one could decrease f in order to increase the stagnation pressure P_0. Conventional pulse beam sources have repetition rates of 10$\sim$100Hz and pulse durations between 10μs and 1ms. Operating the pulse beam source at 10Hz and 100μs would allow one to increase the stagnation pressure within the pulse by a factor of 1000 compared to the continuous beam source. In reality, the volume of the chamber also needs to be considered for scattering of the gas pulse from the chamber walls, which is discussed in more detail by Scoles [Sco88].

There is an additional advantage of the pulse beam source particularly for creating WC molecules. We have previously discussed a way to reduce the blackbody radiation coming from the W filament beam source in subsection 2.2.3. Although the technique described in Fig. 2.10 greatly reduced the noise level in the LIF spectrum, we still had about 1000 photon counts/s of light background coming from imperfect shielding of the glowing W filament. A pulse supersonic beam source combined with the gated photon counting technique could completely eliminate this problem. As described in Fig. 3.1, the pulse of light flux that comes from the laser vaporization process travels much faster than the pulse of molecular beam flux, which temporally separates two of

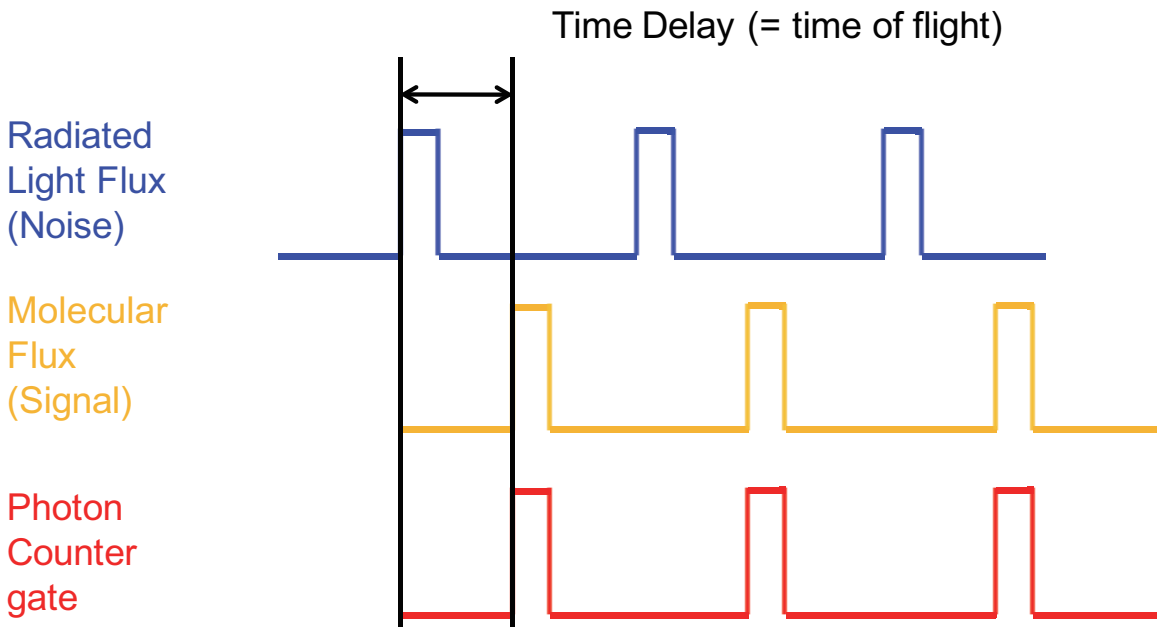

Figure 3.1: Diagram of the gated photon counting technique used with a pulse beam source.

them by the time of flight of the molecules. By temporally matching the gate of the photon counter exactly to the molecular beam pulse, one could selectively count the LIF photons coming from the molecular pulse, and eliminate the light background.

3.2 Pulse supersonic beam apparatus

In order to achieve higher cooling efficiency of the molecules and a lower light background level for LIF spectroscopy, we have built a new pulsed supersonic beam apparatus. First the tungsten gets vaporized from a rod (American Elements, 99.9% purity) by the third harmonic of the Nd:YAG pulse laser (Quantel), while the solenoid gas valve (Parker, general valve series 999) entrains the atoms with a pulse of $350psi$ of Argon buffer gas pressure. The WC molecules were generated by adding 10% methane to the buffer gas, which allows for the chemical reaction $W + CH_4 \rightarrow WC + 2H_2$ to happen. The molecules get cooled down through buffer gas collisions, resulting in low internal temperatures. The turbo pump with 1500L/s of pumping speed maintained

the operating pressure to be 5×10^{-6} Torr inside the vacuum chamber. The diagram of the experimental apparatus is shown in Fig. 3.2.

As for the W transitions, a tunable cw Ti-SAPH laser (Coherent MBR110) generated the IR light, which was frequency doubled with a LBO crystal inside a cavity (Coherent MBD200) to produce light in the 380 nm - 410 nm range. This wide range of tunability enabled us to probe three different W electronic transitions. The probe laser was focused with an intensity of $\sim 1mW/cm^2$ at the intersection point where the laser beam is crossing the atomic beam perpendicularly. The laser induced fluorescing light was collected by a spherical lens into a water cooled photo-multiplier tube (Hammamatsu) connected to the photon counter. The photon counts were recorded simultaneously as the wavelength meter (High Finesse WSU series) measures the frequency of the probe laser with an accuracy level of a few MHz, which will be discussed in the last part of this section.

For tungsten carbide, a tunable cw diode laser (Toptica DL pro) at the wavelength of 484nm-487nm range covered the $[20.6]\Omega = 2, v' = 4 \leftarrow X^3\Delta_1, v" = 0$ transition of WC. The probe laser was focused with an intensity of $\sim 100mW/cm^2$ at the intersection point where the laser beam is crossing the molecular beam perpendicularly. The laser induced fluorescing light was collected and the corresponding frequency information was recorded in a similar way described above. The uncertainty of frequency measurements are defined in two different cases, which are the measurement of absolute frequency and the measurement of relative frequency shift.

The uncertainty of absolute frequency depends on the stability of the frequency reference which the wavelength meter synchronizes to. The current settings use a frequency stabilized HeNe laser (SIOS-02 series) with a stability of $\sim 10MHz$, which was claimed by the manufacturer. In other words, there could be an inconsistency at the same level in absolute frequency measurement. We show in Fig. 3.3, where the absolute frequency of the $^{182}W^{12}C$, R(1) $[20.6]\Omega = 2, v' = 4 \leftarrow X^3\Delta_1, v" = 0$

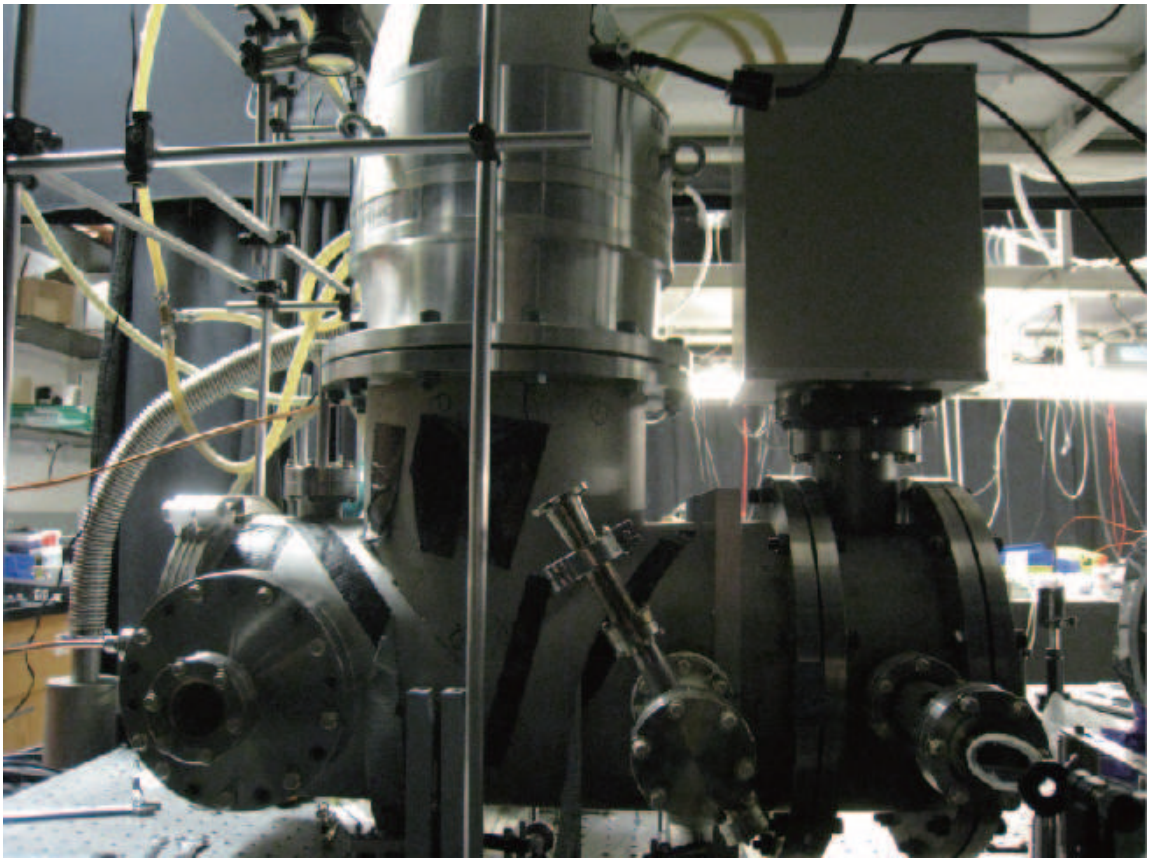

Figure 3.2: Diagram of tungsten carbide pulse supersonic beam apparatus

Table 3.1: Experimental sources of error in frequency measurement.

Source of Error	Estimate
Statistical Error	1.6MHz
Fractional Systematic Error in Relative Frequency	6×10^{-4}
Systematic Error in Absolute Frequency	20MHz

transition was measured over a period of several months to show this effect. From the plot, we saw an 1σ uncertainty of about 20MHz over a 4 month period. This is assigned as a systematic error in absolute frequency.

What we are more interested in is the uncertainty of relative frequency shift, as our main concern is to measure the differences in energy levels coming from various interaction Hamiltonians of WC. If we were to measure a relative frequency shift between two peaks, the systematic shift coming from the HeNe reference would cancel out when we take the frequency difference. Therefore we are only left with the uncertainty that could come from the interferometer part of the wavelength meter. We estimate the uncertainty of relative frequency shift by comparing the isotope shifts of the ${}^1S_0 \rightarrow {}^3P_1$ transition of Ytterbium (Yb) measured from our wavelength meter with the measurements from a different group [PSK$^+$09]. The process is shown in Appendix A, where we have assigned 1.6MHz of statistical uncertainty and 6×10^{-4} of fractional systematic uncertainty for our relative frequency shift measurements. All of these uncertainties are listed in Table 3.1. Both statistical and systematic uncertainties are taken into account for 1σ errors of our experimental results in the following section.

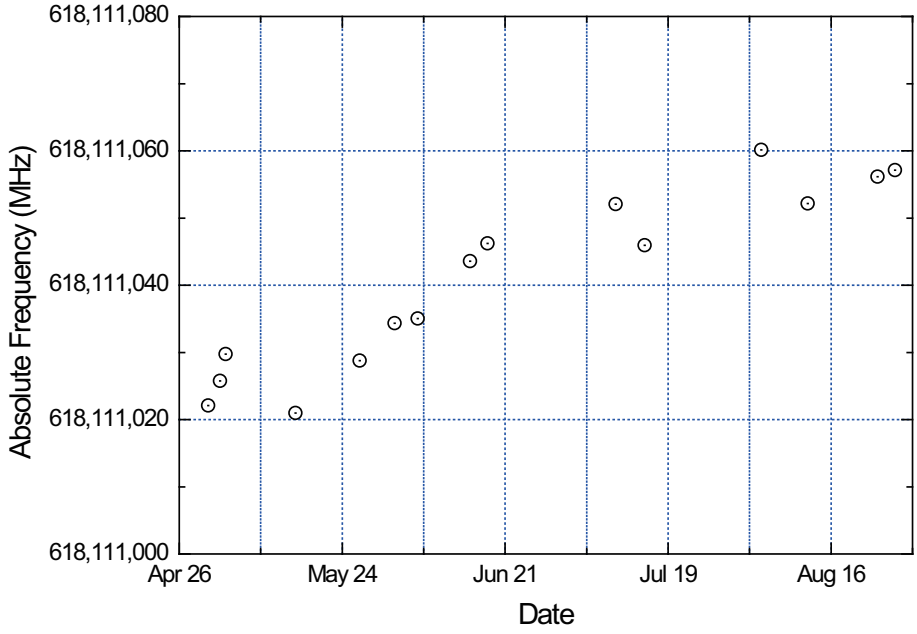

Figure 3.3: The $^{182}W^{12}C$, R(1) line position of the $[20.6]\Omega = 2, v' = 4 \leftarrow X^3\Delta_1, v" = 0$ transition has been measured over a 4 month period in 2011.

3.3 Tungsten transition measurements

Using the pulse supersonic beam apparatus shown in Fig. 3.2, we have measured three different electronic transitions of tungsten through high resolution LIF spectroscopy. The initial motivation for the study of the tungsten transition was to optimize the pulse supersonic beam conditions. These optimization processes that were introduced in section 2.3 only require information on the width and strength of the W transition, and does not require detailed isotope shift or hyperfine shift analysis. However, we found out that high resolution spectroscopic study of tungsten is also of interest in various fields of physics [Mor00, B$\ddot{8}$2, ASW88, ASTW88, N^+96, F^+01], even outside the scope of electron EDM experiments. This drove us to investigate several lesser-known tungsten transitions in more detail.

In general, since tungsten is a 5d shell atom, its isotope shift and hyperfine structure allow enhanced understanding of nuclear structure in the deformed region on the

nuclear chart. Büttgenbach [B82] analyzed the hyperfine structure of 4d- and 5d-shell atoms to study contact interaction terms. Aufmuth [ASTW88] extracted the nuclear parameter λ from tungsten optical isotope shifts.

More recently there has been great interest in using tungsten as plasma facing material in controlled fusion [N+96]. Particularly, the International Thermonuclear Experimental Reactor (ITER) plans to use W tiles on the divertor plasma [F+01], along with the spectroscopic diagnostic system [SCMW03] to estimate the tungsten influx rate for plasma edge modeling. According to Skinner [Ski09], the $^7S_3 \rightarrow {}^7P_4$ transition of neutral tungsten at 400.9 nm is considered promising due to its high transition probability. However, there is a complication in spectroscopic diagnostics due to singly ionized tungsten lines (W II) coincidentally at nearly the same wavelength as the neutral lines (W I), causing line blending issues [Ski09]. Another problem is incomplete information on the $^7S_3 \rightarrow {}^7P_4$ transition, as the latest study did not reveal the hyperfine structure due to limited resolution [ASTW88]. This would lead to further difficulties in accurate modeling of the tungsten influx rate at ITER.

In this section, we will present isotope shifts and hyperfine structure measurements of three neutral tungsten transitions in the near UV range. Laser induced fluorescence (LIF) spectroscopy on an atomic beam was performed on the $^5D_0 \rightarrow {}^5F_1$ transition at 384.9 nm, the $^7S_3 \rightarrow {}^7P_4$ transition at 400.9 nm and, the $^7S_3 \rightarrow {}^7P_3$ transition at 407.4 nm. The magnetic dipole hyperfine constant of the $^7S_3$ level is compared with the prior report [BDT79], and three new measurements are made for the constants of $^7P_3$, $^7P_4$ and $^5F_1$ levels. The isotope shifts of the 384.9 nm transition is presented for the first time here and the isotope shifts of 400.9 nm and 407.4 nm were measured with approximately 10 times higher precision compared with the previous results. High resolution isotope shift study of these three transitions enabled us to extract the nuclear parameters λ and λ_{rel}, which were compared with the previous results [ASTW88]. Also, the completely resolved tungsten spectrum at 400.9 nm is

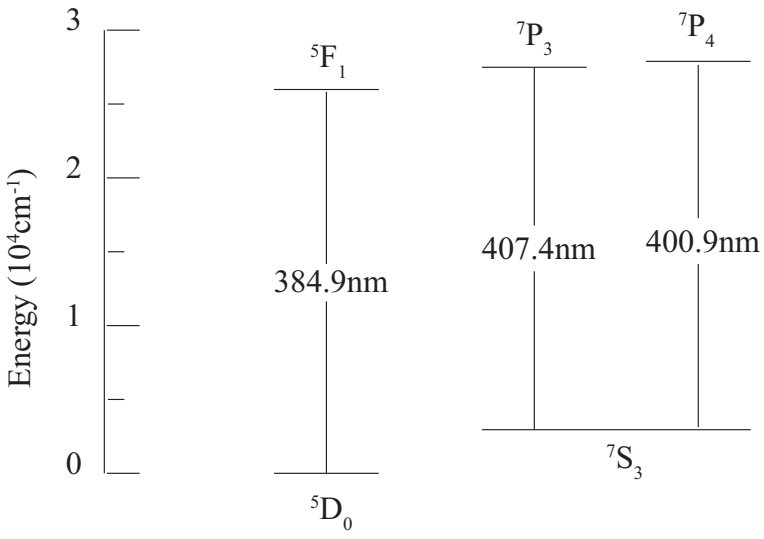

Figure 3.4: Tungsten transitions and related energy levels.

directly related to the application at ITER [Ski09].

3.3.1 Experimental results

Three of the measured W optical transitions are shown in figure 3.4 with their relevant energy levels. The 384.9 nm transition is from the $^5D_0$ ground electronic state with the $5d^46s^2$ configuration to the $^5F_1$ excited state with $5d^36s^26p$ configuration [Wya10]. Two other transitions of 400.9 nm and 407.4 nm share the same low lying metastable state of $^7S_3$ with $5d^56s$ configuration, and excited states of $^7P_4$ and $^7P_3$ both having $5d^46s6p$ configuration [Wya10].

Tungsten has four even isotopes of ^{180}W,^{182}W,^{184}W,^{186}W, with nuclear spin of 0, and one odd isotope of ^{183}W, with nuclear spin of 1/2 giving rise to hyperfine structure. As shown in Figs. 3.5− 3.7, 400.9 nm, 407.4 nm, and 384.9 nm transitions have three, four, and two allowed electric dipole hyperfine transitions, respectively.

Previous studies of the 400.9 nm and 407.4 nm transition reported 20 $\sim$ 30MHz precision on isotope shift measurements with the hyperfine structures being unresolved [ASTW88]. In this work, we have achieved 10 times higher precision on the iso-

tope shift measurements of both transitions, and the hyperfine structures are clearly resolved as well. These are shown in Fig. 3.5 and 3.6. The ratio of the peak amplitudes agreed within 10% level of the natural abundance ratio combined with the hyperfine line strengths, which was calculated from the Clebsch-Gordan coefficients. The small disagreement comes from the fluctuation of atomic beam intensity. The linewidth of the measurements were mainly limited by Doppler broadening, with a Gaussian linewidth of 5MHz. We extract the line positions of each isotope from individual Gaussian fits, except for the merged peaks of ^{183}W(b) and ^{183}W(c) in fig. 3.6, which we fit to two Gaussians simultaneously. The fit gave a frequency uncertainty of 200kHz in line positions which is negligible compared with the measurement uncertainty described in the previous section.

As seen in figure 3.7, the isotope shifts of the 384.9 nm transition were partly unresolved due to limited resolution, and ^{180}W with 0.12% natural abundance is believed to be masked underneath the hyperfine state (b) of ^{183}W. As some of the peaks weren't resolved, we had to take a different approach to analyze the isotope shifts. The first step was to take an average of multiple scans of the transition, in order to eliminate the beam fluctuation effect and get an exact line profile. After this, we used a multi parameter Gaussian fit to extract the isotope and hyperfine shifts. Based on the natural abundance ratio and the intensity rule for the hyperfine transitions, we identified two peaks on the wing side in figure 3.7 as the hyperfine states of ^{183}W. Also, we noticed the center of gravity of ^{183}W lying closer to the right side of the unresolved center peak, which indicates negative isotope shifts for the 384.9 nm transition. With the above constraints for peak assignments, the least square fit was performed to match the experimental data. The least square fitting curve is shown as a red dashed line with a Gaussian linewidth of 5MHz which overlaps well with the experimental data shown in black hollow circles. The blue solid line is the result of the simulation with a linewidth of 0.5MHz to show the line positions,

and the yellow dotted line is the center of gravity position of ^{183}W. The ^{180}W isotope was excluded from the fit, as the experimental data does not have enough resolution to constrain its position. We note that regardless of the peak assignments, the upper limits of 20 MHz/amu for the isotope shifts and 80MHz for the hyperfine splitting of the $^5F_1$ state, can be deduced from figure 3.7. No previous study of isotope shifts exists for the 384.9 nm transition, however, Gluck [Glu65] has reported 0 isotope shifts for this transition with a frequency resolution of 30 MHz, which is consistent with our result within their uncertainty of measurement.

3.3.2 Hyperfine structure analysis

The hyperfine structure of the ^{183}W isotope is only cause by the magnetic dipole interaction as it has a nuclear spin of 1/2 [Kop58]. In this case, the hyperfine energy levels are given by,

$$E_F = E_J + hA\frac{F(F+1) - J(J+1) - I(I+1)}{2}, \tag{III.2}$$

where h is Planck's constant and A is the magnetic hyperfine constant. The shifted energy levels due to this hyperfine interaction are shown on Figs. 3.5– 3.7. The hyperfine frequency splitting within the electronic state becomes,

$$\delta\nu_{hyperfine} = A\left(J + \frac{1}{2}\right). \tag{III.3}$$

It is straightforward to extract the magnetic hyperfine constant A from measured frequency splittings using equation III.3. As some of the hyperfine splittings are measured in multiple transitions, such as the splitting of the $^7S_3$ state, we take the weighted mean of the measurements from different transitions to get A, which are shown in Table 3.2. We report three new hyperfine constants for $^7P_3$, $^7P_4$, $^5F_1$ states, and the constant for the $^7S_3$ state is compared with the previous result [BDT79].

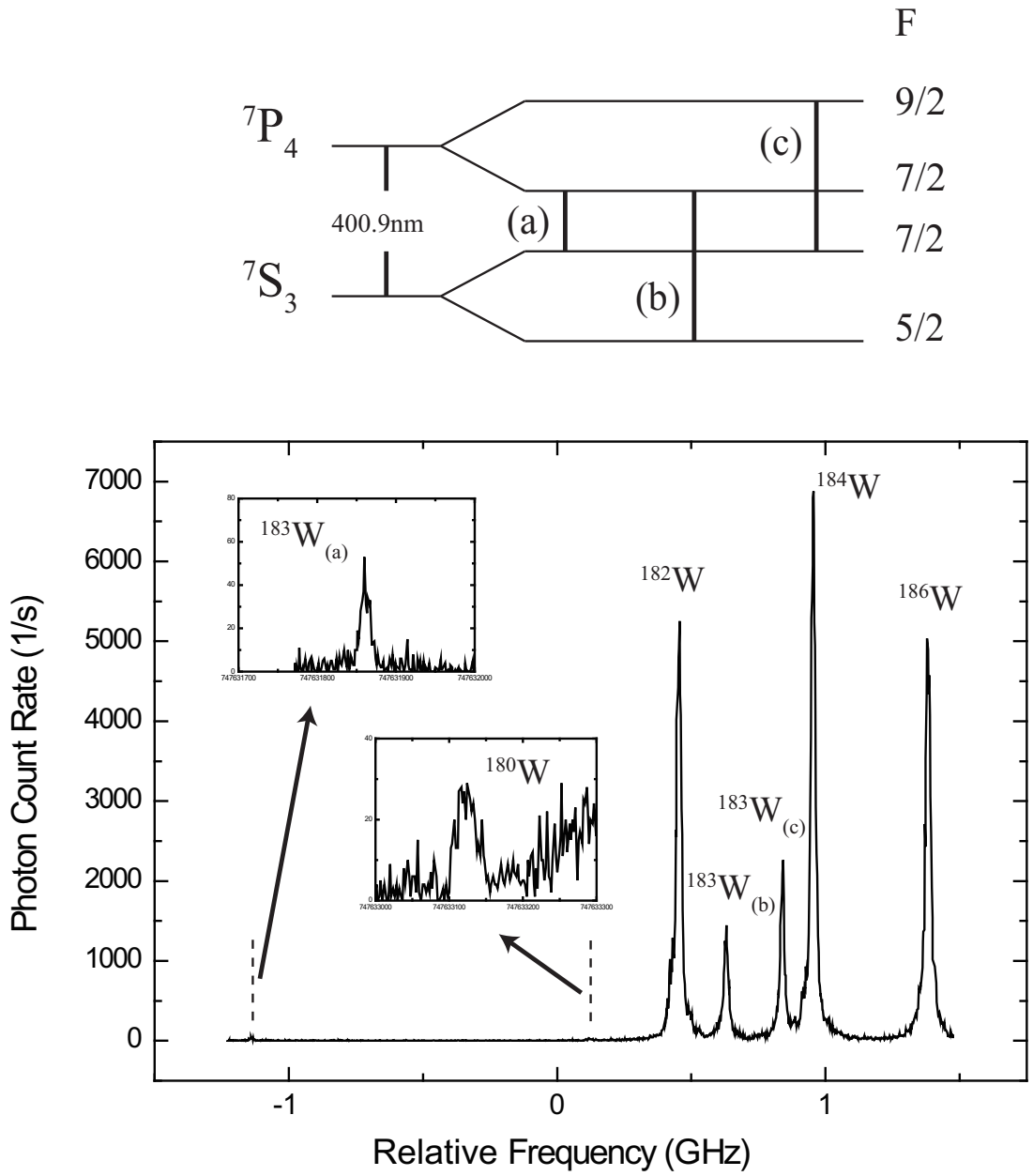

Figure 3.5: $^7S_3 \rightarrow {}^7P_4$ tungsten transition measured by laser induced fluorescence spectroscopy. Dashed lines show the positions of the smaller peaks.

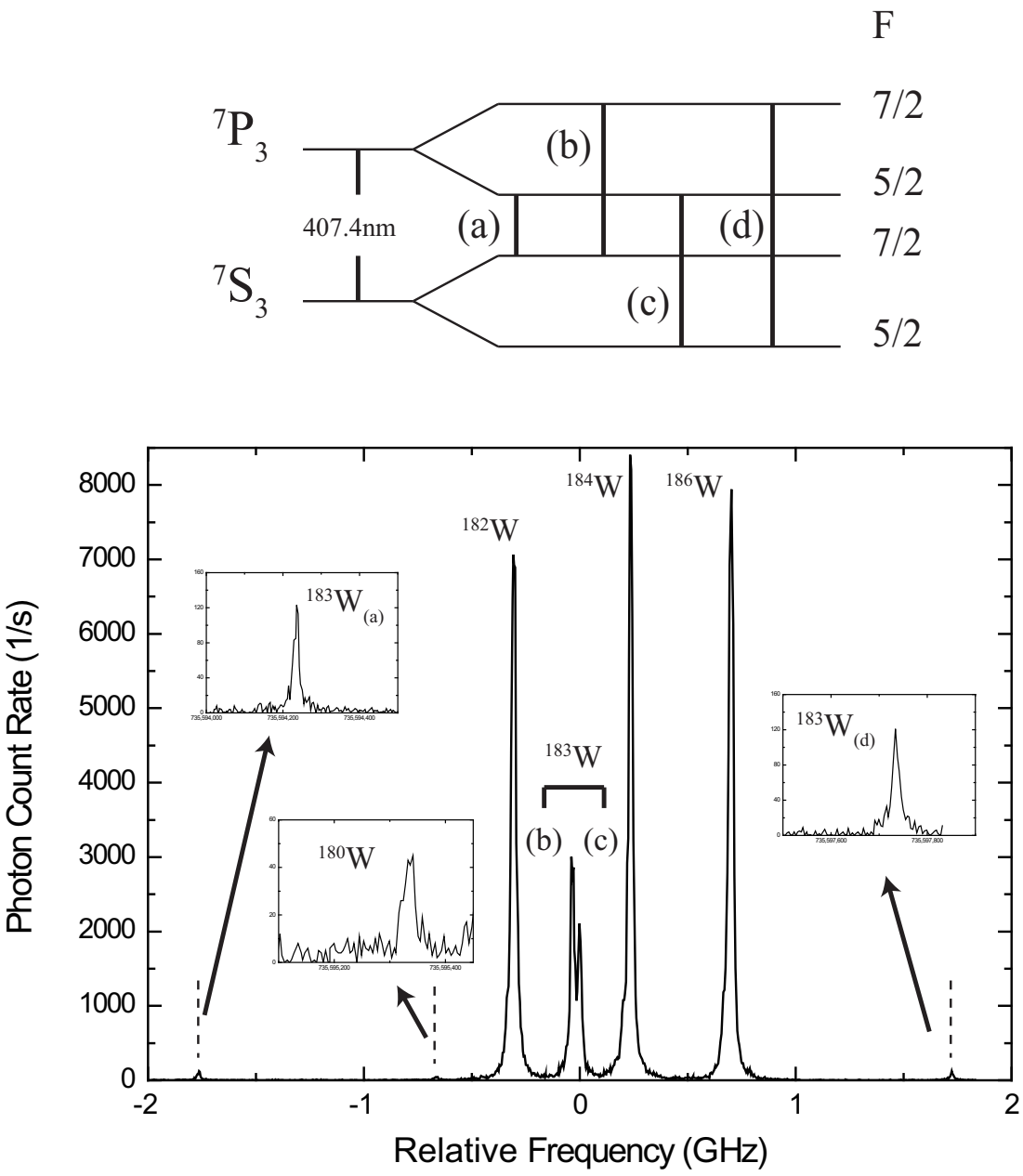

Figure 3.6: $^7S_3 \rightarrow {}^7P_3$ tungsten transition measured by laser induced fluorescence spectroscopy. Dashed lines show the positions of the smaller peaks.

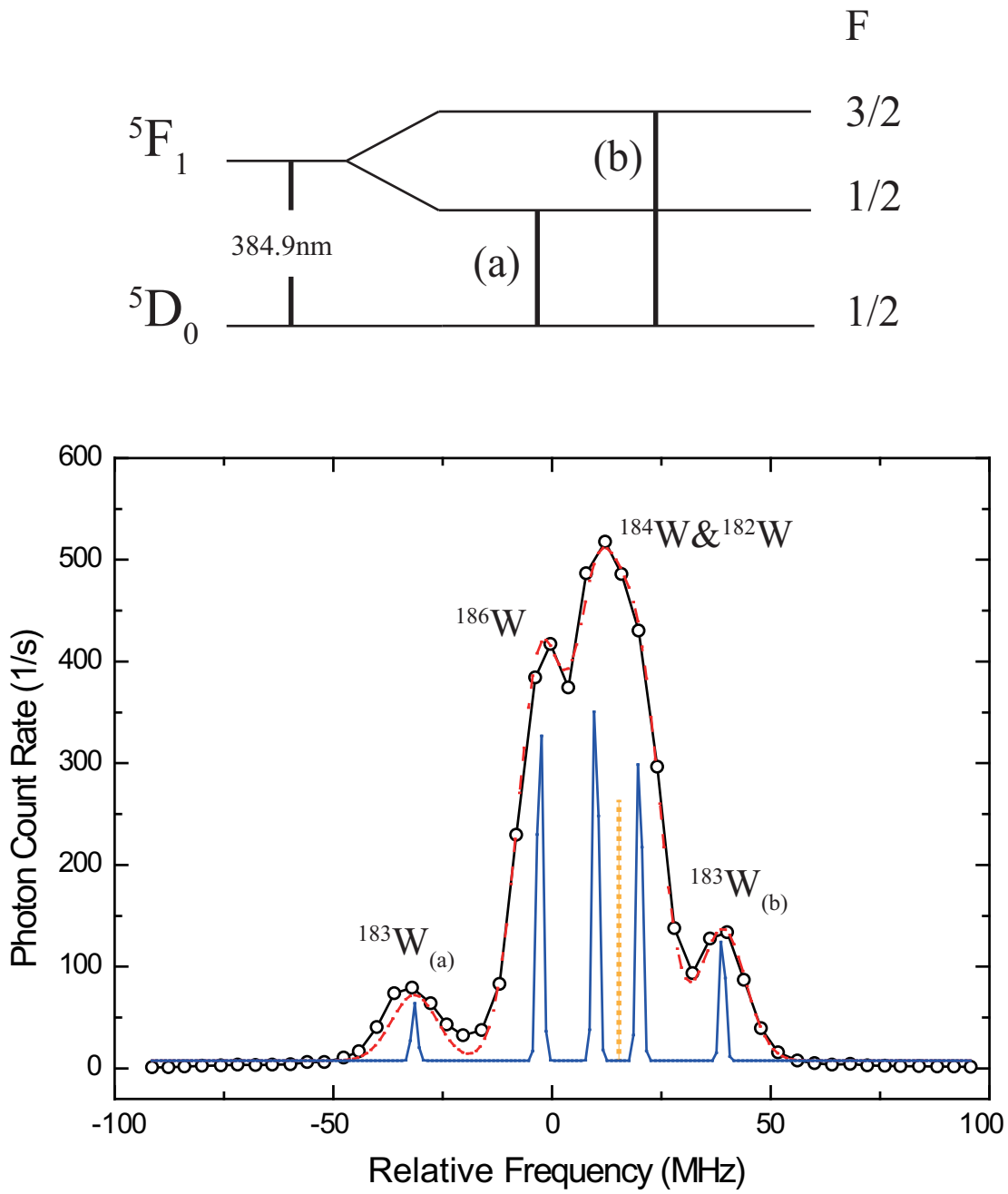

Figure 3.7: $^5D_0 \rightarrow {}^5F_1$ tungsten ground state transition measured by laser induced fluorescence spectroscopy. Black hollow circles are the experimental data, the red dashed line is the least square fit, the blue solid line is the simulated line positions, and the yellow dotted line is the center of gravity position for ^{183}W.

Table 3.2: The magnetic dipole hyperfine constant A was measured and compared for $^7S_3$, $^7P_3$, $^7P_4$, and $^5F_1$ electronic states of Tungsten. The 1 σ errors are shown inside the parentheses in units of the last decimal quoted.

	Hyperfine constant A (MHz)	
Electronic States	This work	Ref. [BDT79]
$5d^5 6s\ ^7S_3$	505.5(4)	505.592(12)
$5d^4 6s6p\ ^7P_3$	496.2(6)	
$5d^4 6s6p\ ^7P_4$	440.5(6)	
$5d^3 6s^2 6p\ ^5F_1$	47.1(11)	

Good agreement is found within the error of the measurement for the $^7S_3$ state.

Wyart suggested $5d^4 6s6p$ as the dominant configuration for $^7P_3$, $^7P_4$ states, and $5d^3 6s^2 6p$ configuration for the $^5F_1$ state [Wya10]. Our measurements of larger constants A in the cases of the $^7P_3$ and $^7P_4$ states compared with the case of the $^5F_1$ state support Wyart's configurations. This is due to the open shell 6s electron from the $5d^4 6s6p$ configuration having bigger contributions to A than the $5d^3 6s^2 6p$ configuration.

3.3.3 Isotope shift analysis

The theory of atomic isotope shifts is well developed in many publications [Sel69, HS74, Kin84, AHS87]. Here, we closely follow the notations of Aufmuth [AHS87]. The isotope shift between two isotopes with mass number A and A' of an optical transition i can be written as,

$$\delta\nu_i^{AA'} = \delta\nu_{i,MS}^{AA'} + \delta\nu_{i,FS}^{AA'}, \tag{III.4}$$

where MS stands for Mass Shift and FS for Field Shift. The Mass shift is further separated into Normal Mass Shift (NMS) and Specific Mass Shift (SMS), both coming from the change in nuclear mass.

$$\delta\nu_{i,MS}^{AA'} = \delta\nu_{i,NMS}^{AA'} + \delta\nu_{i,SMS}^{AA'} \tag{III.5}$$

$$= (M_{i,NMS} + M_{i,SMS})\,\tfrac{A'-A}{AA'} \tag{III.6}$$

The Field Shift (FS) originates from the change in volume and shape of the nucleus. Therefore it is directly related to the changes in mean square nuclear charge radii $\delta\langle r^2\rangle$. This relation is shown below,

$$\delta\nu_{i,FS}^{AA'} = F_i\lambda^{AA'} \tag{III.7}$$

$$\lambda^{AA'} = \delta\langle r^2\rangle^{AA'} + \tfrac{C_2}{C_1}\delta\langle r^4\rangle^{AA'} + \tfrac{C_3}{C_1}\delta\langle r^6\rangle^{AA'} + \cdots \tag{III.8}$$

$$\approx \delta\langle r^2\rangle^{AA'} \tag{III.9}$$

$$F_i = E_i f(Z), \tag{III.10}$$

where E_i, $f(Z)$ are the electronic and relativistic correction factors defined in ref. [AHS87] and C_n/C_1 ratios are tabulated by Seltzer [Sel69].

The NMS can be calculated directly as shown by ref. [HS74],

$$M_{i,NMS} = \frac{\nu_i}{1836.1}, \tag{III.11}$$

where ν_i is the atomic transition in MHz. However, the SMS needs to be extracted

from the King plot [Kin84], which requires isotope shifts from two different transitions, one of them being the reference transition with a known SMS. The $ns^2 - nsnp$ transitions are often used as a reference transition because its SMS can be evaluated semi-empirically [HS74]. As we haven't measured any $ns^2 - nsnp$ transitions in this work, we used the ($5d^46s^2\ ^5D_1 - 5d^46s6p\ ^7F_1$) 543.5 nm transition measured from W.G. Jin [JWI+94] as a reference transition to make the King plots of our measured transitions. These King plots are shown in figure 3.8 where the axes are the modified isotope shifts of each transition defined as,

$$\delta\nu_i^{mod} = (\delta\nu_i - \delta\nu_{i,NMS})\frac{AA'}{A' - A}. \tag{III.12}$$

From the linear fit, we obtain the relations,

$$Slope = \frac{E_i}{E_{543.5nm}}, \tag{III.13}$$

$$Intercept = M_{i,SMS} - M_{543.5nm,SMS} \times \frac{E_i}{E_{543.5nm}}. \tag{III.14}$$

The SMS of the 543.5 nm transition is estimated by a semi-empirical relation,

$$\delta\nu^{AA'}_{543.5nm,SMS} = (0 \pm 0.5)\delta\nu^{AA'}_{543.5nm,NMS}, \tag{III.15}$$

which is only valid for $ns^2 - nsnp$ transitions [HS74]. Combining equations $12 - 14$, we can calculate the SMS of our measured transitions. Knowing the NMS and the SMS, the FS is readily calculated from eq. III.4 and III.6. The extracted values of the NMS, the SMS and the FS for 384.5 nm, 400.9 nm and 407.4 nm transitions are given in Table 3.3. As discuss previously, isotope shifts of the 384.9 nm transition are given by the least square Gaussian fitting method.

From Eqs. III.7 and III.10, the Field Shift is linked to the nuclear parameter

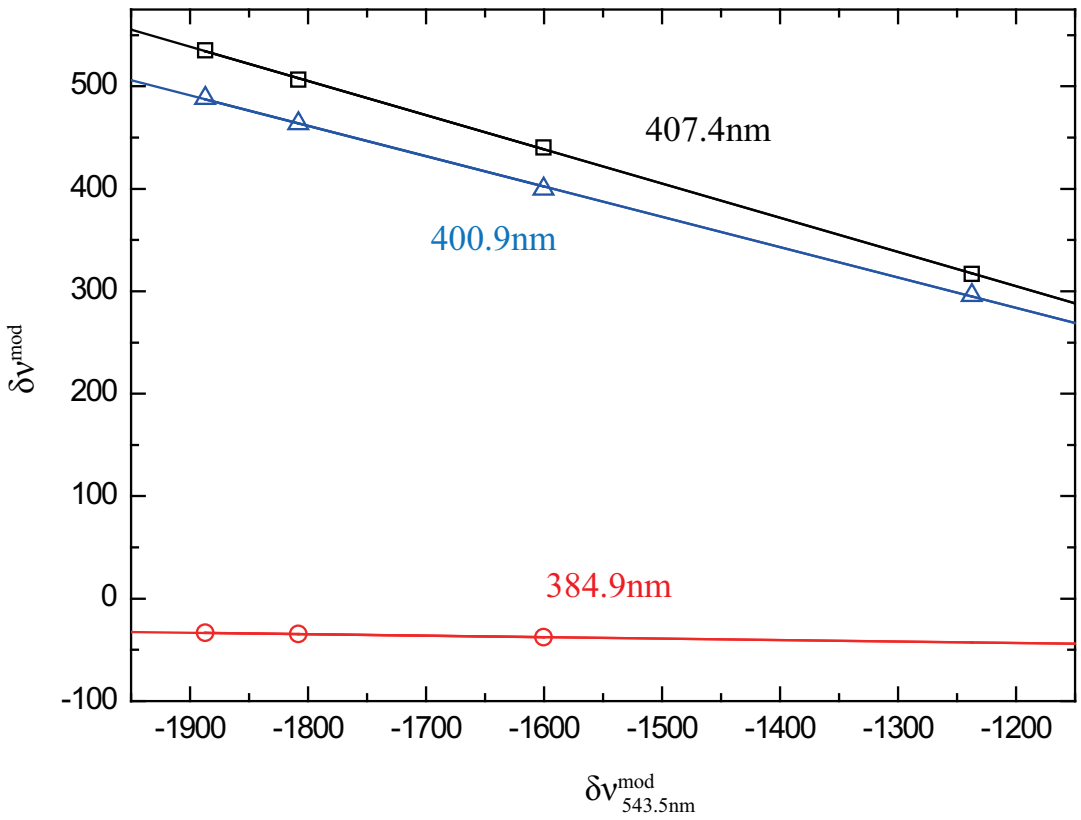

Figure 3.8: King plot of the modified isotope shifts of the 384.9 nm, 400.9 nm and 407.4 nm transitions with the 543.5 nm transition from W.G. Jin [JWI+94] as the reference transition. A factor of $\frac{2}{184\times186}$ was multiplied to both axes for display purposes, which is to get the units in MHz. The ^{180}W isotope was not measured for the 384.9 nm transition. Straight lines passing through the symbols are the least square fit results. Experimental uncertainties are all within the symbols.

Table 3.3: NMS, SMS, FS, and $\lambda^{AA'}$ are shown for 384.9 nm, 400.9 nm and 407.4 nm Tungsten transitions. 1σ errors are shown inside the parentheses. For $\lambda^{AA'}$, we show two independent errors, where the first parenthesis shows the experimental uncertainty from the field shift measurement and the second parenthesis showing theoretical uncertainty of F_i from equation III.7.

Transition (nm)	Isotopes (A,A')	$\delta\nu_i^{AA'}$ (MHz)	$\delta\nu_{i,NMS}^{AA'}$ (MHz)	$\delta\nu_{i,SMS}^{AA'}$ (MHz)	$\delta\nu_{i,FS}^{AA'}$ (MHz)	$\lambda^{AA'}$ (fm^2)
384.9	184,186	-12.7(1.6)	24.8	-60.2(0.9)	22.6(1.9)	0.0808(68)(57)
	182,184	-10.0(1.6)	25.3	-61.5(0.9)	26.1(1.9)	0.0932(68)(65)
	182,183	-4.5(1.6)	12.7	-30.9(0.9)	13.7(1.9)	0.0489(68)(34)
400.8	184,186	423.6(2.1)	23.8	-71.4(3.7)	471.2(4.3)	0.0810(7)(57)
	182,184	498.4(2.1)	24.3	-72.9(3.8)	547.0(4.3)	0.0929(7)(65)
	182,183	263.2(2.1)	12.2	-36.7(2.1)	287.7(2.9)	0.0489(5)(34)
	180,182	334.0(2.1)	24.9	-74.6(3.9)	383.7(4.4)	0.0651(7)(46)
407.4	184,186	463.6(2.9)	23.4	-95.5(4.1)	535.7(5.0)	0.0803(7)(56)
	182,184	541.4(2.9)	23.9	-97.6(4.2)	615.1(5.1)	0.0932(8)(65)
	182,183	286.9(2.9)	12.0	-49.1(2.4)	323.9(3.8)	0.0490(6)(34)
	180,182	355.6(2.9)	24.5	-99.8(4.3)	430.9(5.2)	0.0653(8)(46)

$\lambda^{AA'}$ through E_i and $f(Z)$. The electronic factors $E_{384.9nm}$, $E_{400.9nm}$ and $E_{407.4nm}$ are derived from eq. III.13, with an electronic factor $E_{543.5nm} = 0.40882$ calculated by Aufmuth [ASW88]. The relativistic correction factor $f(Z)$ was calculated by ref. [AHS87] using the isotope shift constant of Blundell [BBP$^+$85]. The extracted $\lambda^{AA'}$ from three different transitions are shown in the last column of Table 3.3. All the results show good agreement within the errors. Two independent sources of errors of $\lambda^{AA'}$ are shown inside the parentheses, with the first parenthesis showing the experimental uncertainty from the field shift measurement and the second parenthesis showing theoretical uncertainty of F_i. The theoretical uncertainty in F_i comes from fractional error in the process of calculating E_i and $f(Z)$, which is estimated to be 5% for all three transitions [Hei85]. However, the experimental uncertainty of the field shift varies for different transitions.

In order to see the individual error contributions during the process of the FS derivation, we combine Eqs. III.4, III.6, III.13 and III.14, to get,

$$\delta\nu_{i,FS}^{AA'} = \delta\nu_i^{AA'} - \delta\nu_{i,NMS}^{AA'} - \frac{AA'}{A'-A} \times Intercept - \delta\nu_{543.5nm,SMS}^{AA'} \times Slope. \quad \text{(III.16)}$$

We analyze different sources of uncertainties in eq. III.16 for all three transitions, which are shown in Table 3.4 for the case of the isotope shift between ^{184}W and ^{186}W. Note that the second term of the right hand side of eq. III.16, is a well defined value from eq. III.11, and therefore has no error. Rows 1 through 3 of Table 3.4 show uncertainties that are linked to experimental uncertainty of our frequency measurements. However the uncertainty described in the last row, which contains the SMS of the reference line, only relies on the semi-empirical relation of eq. III.15. This becomes the dominating error contribution in the case of the 400.9 nm and 407.4 nm transitions. Therefore, improving the experimental errors alone, which only affects

Table 3.4: The sources of uncertainties in $\delta\nu_{i,FS}^{184,186}$ from different transitions of tungsten.

	Transitions (nm)		
Source of Uncertainty	384.9	400.9	407.4
Statistical Uncertainty of $\nu_i^{184,186}$ (MHz)	1.6	1.6	1.6
Systematic Uncertainty of $\nu_i^{184,186}$ (MHz)	0.06	1.2	2.4
Uncertainty of $\frac{AA'}{A'-A}\times$ Intercept of King plot (MHz)	0.9	1.1	1.4
Uncertainty of $\nu_{543.5nm,SMS}^{184,186}\times$ Slope of King Plot (MHz)	0.2	3.6	3.9

first three rows of Table 3.4, would not further decrease the uncertainty of the FS of the 400.9 nm and 407.4 nm transitions. A better estimation of the SMS is required for further improvement.

Since the extracted $\lambda^{AA'}$ in Table 3.3 showed good agreement among different transitions, we take the weighted mean of these to report the final values of $\lambda^{AA'}$ and compare with the previous results of ref. [AHS87] in Table 3.5. The errors are presented in the same manner as before, showing the experimental uncertainty inside the first parenthesis and the theoretical uncertainty inside the second parenthesis. We notice that experimental uncertainties are much smaller than the theoretical uncertainties for all isotope pairs.

From the above discussion, it is clear that the limiting factor for high precision $\lambda^{AA'}$ measurement mainly comes from the uncertainty in estimation of the Specific Mass Shift through a semi-empirical relation, and the theoretical uncertainties in the Field Shift. First we discuss the possibility of the SMS calculation. Instead of using the King plot approach, there have been several attempts of multi-configuration

calculations of the SMS [MS82, FB82, CLS84]. However, as pointed out by Aufmuth [AHS87], a reliable prediction was never made. Following the approach of ref. [CLS84], the specific mass effect perturbs the energy of the electronic state ψ between mass A and A' by an amount of,

$$\Delta E_{SMS}(\psi) = \frac{A' - A}{AA'} \left\langle \psi \left| \sum_{i>j} \mathbf{p}_i \cdot \mathbf{p}_j \right| \psi \right\rangle, \tag{III.17}$$

where $\mathbf{p}_i$ is the momentum of the i^{th} electron. Thus, the frequency difference in the upper state of ψ_u and the lower state of ψ_l can be written as,

$$\delta\nu^{AA'}_{u\to l,SMS} = \frac{\Delta E_{SMS}(\psi_u) - \Delta E_{SMS}(\psi_l)}{h}. \tag{III.18}$$

Similarly, we can write down an expression for the field effect perturbing the energy of ψ between mass A and A' by,

$$\Delta E_{FS}(\psi) = \frac{\pi a_0^3 \left|\psi(0)^2\right|}{Z} f(Z)\lambda^{AA'}, \tag{III.19}$$

where $|\psi(0)^2|$ is the non-relativistic electron charge density at the nucleus and $f(Z)$ is the same relativistic correction factor which was mentioned above. The frequency difference between the upper state of ψ_u and the lower state of ψ_l becomes,

$$\delta\nu^{AA'}_{u\to l,FS} = \frac{\Delta E_{FS}(\psi_u) - \Delta E_{FS}(\psi_l)}{h}. \tag{III.20}$$

If one could calculate the SMS and FS of the three studied transitions by using the relativistic electronic wavefuctions of $\psi_{^7S_3}$, $\psi_{^7P_3}$, $\psi_{^7P_4}$, and $\psi_{^5F_1}$, we could expect to have an improvement of precision in the $\lambda^{AA'}$ measurement.

However, at the current state, the best way to reduce the fractional error of the nuclear parameter is by defining a relative $\lambda^{AA'}$ as,

Table 3.5: $\lambda^{AA'}$ and $\lambda_{rel}^{AA'}$ compared with previous results from ref. [AHS87]. 1σ errors are shown inside the parentheses. For our results, the first parenthesis shows the experimental uncertainty from the field shift measurement and the second parenthesis showing theoretical uncertainty of E_i and $f(Z)$ from equation III.10.

	Weighted $\lambda^{AA'}$ (fm^2)		Weighted $\lambda_{rel}^{AA'}$	
Isotopes (A,A')	This work	Ref. [AHS87]	This work	Ref. [AHS87]
184,186	0.0807(5)(33)	0.084(7)	1	1
182,184	0.0931(5)(38)	0.097(8)	1.1537(11)	1.154(4)
182,183	0.0488(4)(20)	0.051(5)	0.6047(22)	0.607(5)
180,182	0.0652(5)(26)	0.068(8)	0.8079(14)	0.808(23)

$$\lambda_{rel}^{AA'} = \frac{\lambda^{AA'}}{\lambda^{184,186}}. \tag{III.21}$$

The fractional error of $\lambda_{rel}^{AA'}$ is much smaller than $\lambda^{AA'}$, which can be seen in the last two columns of Table 3.5. The results are in very good agreement with ref. [AHS87], with $3 \sim 16$ times better precision.

3.4 Tungsten carbide transition measurements

In this section, we will shift gears to talk about the $[20.6]\Omega = 2, v' = 4 \leftarrow X^3\Delta_1, v" = 0$ transition of WC measured from the pulse supersonic beam apparatus shown in Fig. 3.2. As shown in Figure 3.9, molecules have rich internal structure where there are rotational and vibrational levels within electronic energy states. The optical detection scheme of the electron EDM state, which is at the rovibrational ground state, is shown in the same figure. High cooling efficiency and low light background level of the pulse supersonic beam source allowed us to successfully detect this rovibrational ground state of WC through LIF spectroscopy. The main experimental

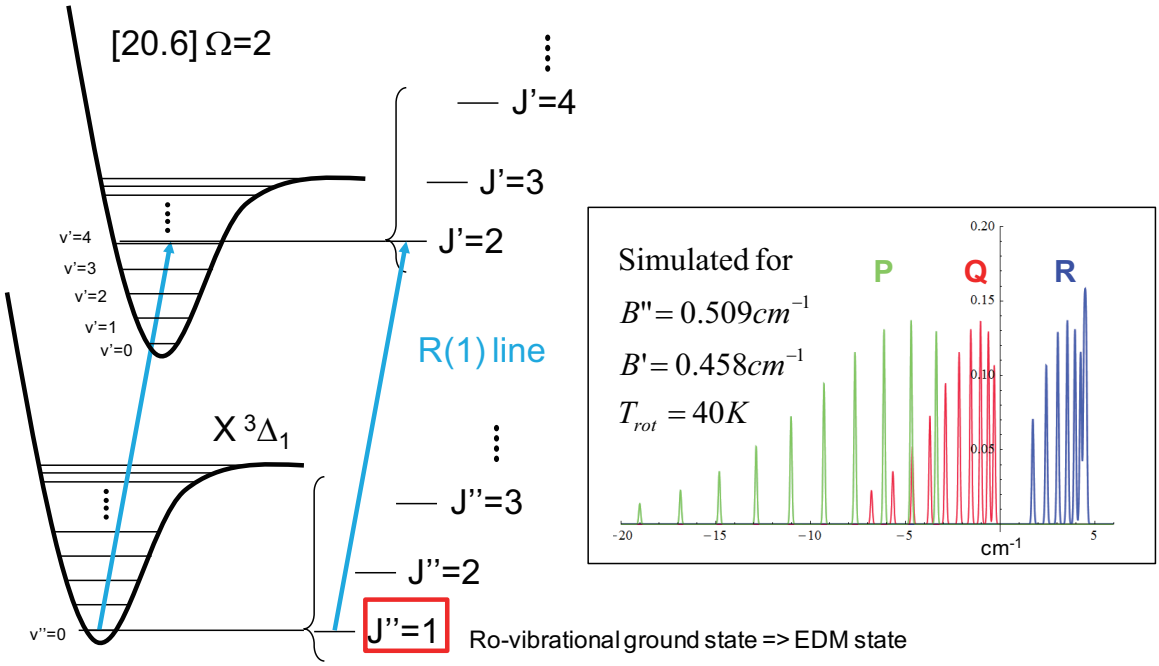

Figure 3.9: The optical detection scheme of the electron EDM state. The inset shows a simulated WC rotational spectra at rotational temperature of 40K.

results of the measured hyperfine constants and Ω-doublet constants of the transition will be presented here. Both of these measurements are closely related to the systematic uncertainties of the EDM experiment, which will be discussed in chapter 4.

3.4.1 Experimental results

Tungsten has four major isotopes of ^{182}W, ^{183}W, ^{184}W, ^{186}W, while Carbon has only one major isotope of ^{12}C with close to 99% abundance. The ^{180}W isotope will not be discussed as we did not have enough signal to noise to detect its 0.12% natural abundance. As a result, four WC isotopes are observed for each rotational transition. The LIF signal was detected with $1 \sim 10$ photon counts per second, which we have averaged over 20 seconds of integration time per data point to get better signal to noise. The background level is dominated by the randomly scattered probe laser light going into the PMT. The strength of the signal varied on a daily basis at the 30%

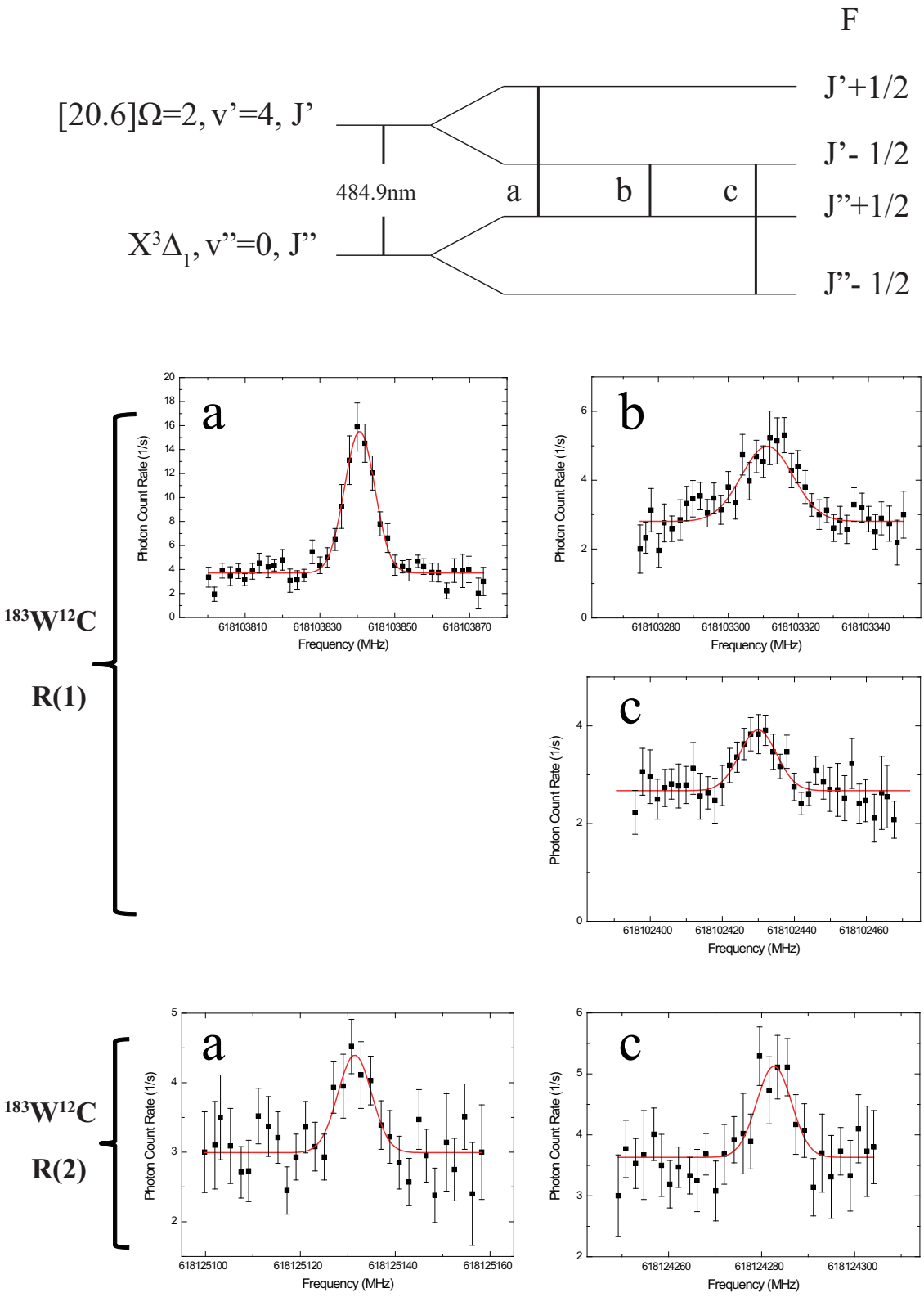

Figure 3.10: R(1) and R(2) lines on $[20.6]\Omega = 2, v' = 4 \leftarrow X^3\Delta_1, v" = 0$ transition was measured for $^{183}W^{12}C$. The photon count rates are averaged over 20 seconds of integration time within the 2MHz frequency bin. 1σ error bars are shown for the photon count rates and the red solid line corresponds to the least square Gaussian fit.

level, depending on the optimization of the WC beam quality.

We measured the R branch ($\Delta J = +1$) of the $[20.6]\Omega = 2, v' = 4 \leftarrow X^3\Delta_1, v" = 0$ transition at $485nm$, where the results of $^{183}W^{12}C$ in Fig. 3.10 show the Hyperfine structure and the results of $^{184}W^{12}C$ in Fig. 3.11 show the Ω-doublet structure. We observed the same Ω-doublet structure in $^{182}W^{12}C$ and $^{186}W^{12}C$ isotopes as well, which will be shown in the Appendix B.

Each of the individual lines had a Doppler Broadened linewidth of $\sim 10MHz$. A least square Gaussian fit was used to extract the center frequency of the line. The fitting error for the center frequency was on the order of sub MHz, therefore, the uncertainties from the wavelength meter discussed in the previous section were the dominant sources of error. The list of our measured line positions are shown with proper error assignments and compared with the previous results of ref. [SSM02] in Table 3.6. The center of gravity position is shown for the $^{183}W^{12}C$ isotope, as it has a hyperfine structure. For the Ω-doublet structure observed in R(4) and R(5) transitions, the center frequency between the double peak is listed on the table. Sickafoose's data [SSM02] shows the fitted line positions with the residuals from the fit given in the parentheses in the units of the last significant digit.

The $^{183}W^{12}C$ isotope has a non-zero nuclear spin, which gives rise to hyperfine structure. Only the magnetic dipole interaction is present as it has a nuclear spin of 1/2 [Kop58]. From the selection rule, there are three allowed electric dipole transitions of $\Delta F = 0, \pm 1$ for each R line. We have measured 5 out of 6 hyperfine transitions in $^{183}W^{12}C$, R(1) and R(2) lines, which are shown in Fig. 3.10. The $^{183}W^{12}C$ isotope has a relatively low natural abundance of 14% compared to other isotopes, therefore, only up to the R(2) transition was detected. Also, the $^{183}W^{12}C$ b transition of the R(2) line has a relatively small Clebsch-Gordan coefficient which made it undetectable with our signal to noise. The intensity ratios of these transitions are calculated to be $[I_a : I_b : I_c = 9 : 1 : 5]$ for R(1) and $[I_a : I_b : I_c = 20 : 1 : 14]$ for R(2).

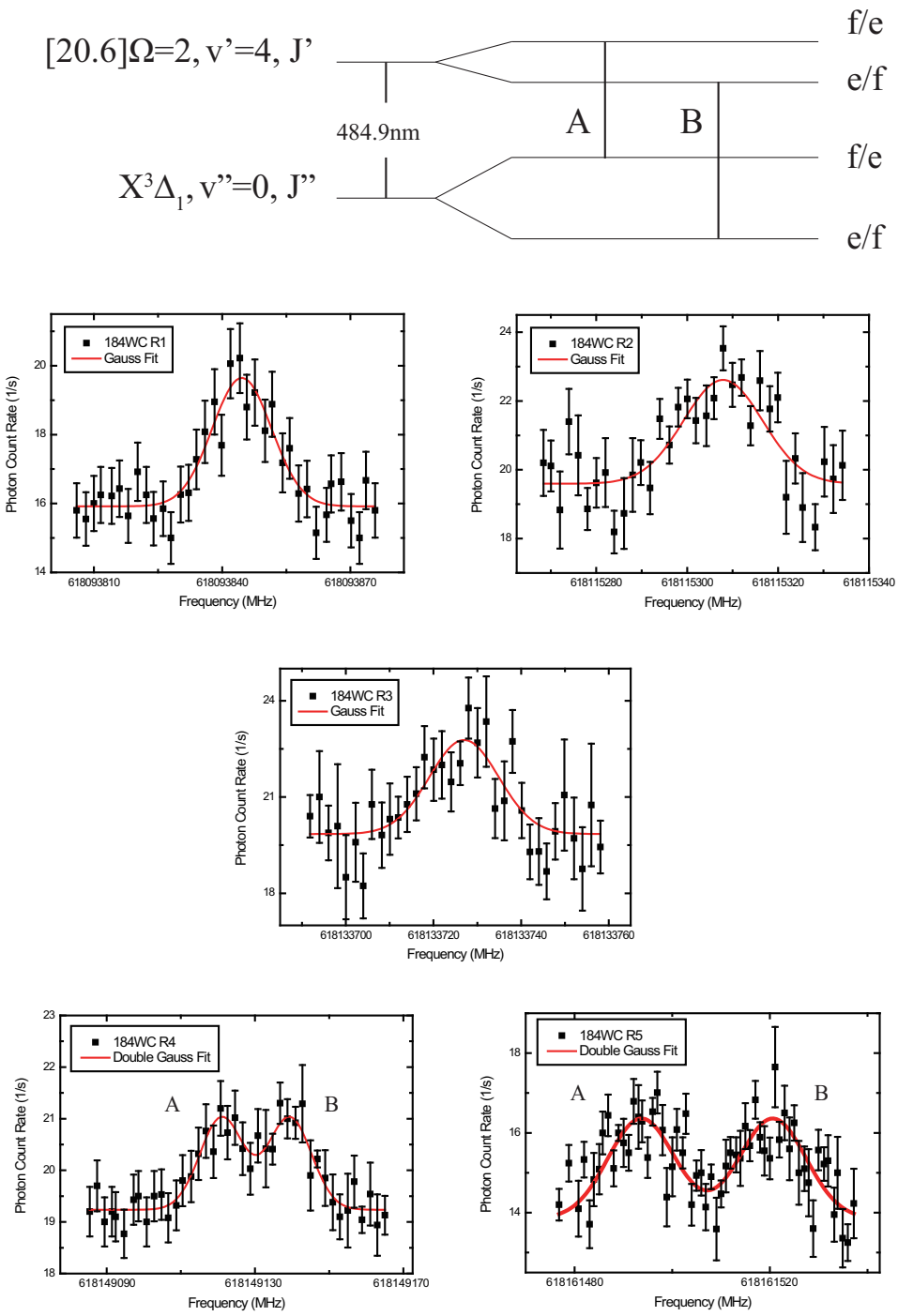

Figure 3.11: The R(1) $\sim$ R(5) lines of the $[20.6]\Omega = 2, v' = 4 \leftarrow X^3\Delta_1, v" = 0$ transition for $^{184}W^{12}C$ are shown. The photon count rates are averaged over 20 seconds of integration time within the 2MHz frequency bin. 1σ error bars are shown for the photon count rates and the red solid line corresponds to the least square Gaussian fit.

Table 3.6: Absolute frequencies of measured lines in the $[20.6]\Omega = 2, v' = 4 \leftarrow X^3\Delta_1, v" = 0$ transition are compared with ref. [SSM02]. The center of gravity position is shown for $^{183}W^{12}C$ isotopes. As for the R(4) and R(5) transitions, where we start to see an Ω-doublet structure, the center of two peaks is used. The 1 σ errors are shown inside the parentheses in the order of first parenthesis with the statistical uncertainty and the second parenthesis with the systematic uncertainty in absolute frequencies. Only the 1 σ fitting error was provided from ref. [SSM02]

Measured Line	This Work (MHz)	Ref. [SSM02] (MHz)
$^{182}W^{12}C$, R(1)	618,110,996(1.6)(20)	618,110,980(690)
$^{182}W^{12}C$, R(2)	618,132,466(1.6)(20)	618,132,416(540)
$^{182}W^{12}C$, R(3)	618,150,892(1.6)(20)	618,151,362(-180)
$^{182}W^{12}C$, R(4)	618,166,298(1.6)(20)	618,166,802(-480)
$^{182}W^{12}C$, R(5)	618,178,709(1.6)(20)	618,178,613(-270)
$^{183}W^{12}C$, R(1)	618,103,338(1.6)(20)	618,102,617(-30)
$^{183}W^{12}C$, R(2)	618,124,778(1.6)(20)	618,123,992(-30)
$^{184}W^{12}C$, R(1)	618,093,845(1.6)(20)	618,093,443(540)
$^{184}W^{12}C$, R(2)	618,115,308(1.6)(20)	618,115,208(180)
$^{184}W^{12}C$, R(3)	618,133,727(1.6)(20)	618,133,345(390)
$^{184}W^{12}C$, R(4)	618,149,130(1.6)(20)	618,149,624(-570)
$^{184}W^{12}C$, R(5)	618,161,507(1.6)(20)	618,162,095(-780)
$^{186}W^{12}C$, R(1)	618,077,509(1.6)(20)	618,076,625(660)
$^{186}W^{12}C$, R(2)	618,098,953(1.6)(20)	618,098,509(240)
$^{186}W^{12}C$, R(3)	618,117,361(1.6)(20)	618,117,186(-30)
$^{186}W^{12}C$, R(4)	618,132,760(1.6)(20)	618,132,805(-210)
$^{186}W^{12}C$, R(5)	618,145,138(1.6)(20)	618,145,397(-420)

Figure 3.11 shows the five lowest R lines of the $^{184}W^{12}C$ isotope for the given transition. Both the $X^3\Delta_1$ state and the $[20.6]\Omega = 2$ have nearly degenerate spin states of opposite parity called the Ω-doublet, where there are two allowed electric dipole transitions among them for each R transitions. Following the notations of Brown [BCM87], we label them $e/f \leftrightarrow e/f$. Due to the J dependence of the doublet interaction, $H_{doublet} \propto J(J+1)$, we only see the doublet structure when the interaction term becomes larger than our Doppler limited linewidth. As a result, we saw the doublet structure only at higher J line transitions, which are R(4) and R(5) transitions.

3.4.2 Hyperfine constant

As discussed previously, the hyperfine structure of $^{183}W^{12}C$ isotope is only caused by the magnetic dipole interaction, which can be written as,

$$H = h \times \frac{F(F+1) - J(J+1) - I(I+1)}{2J(J+1)}, \tag{III.22}$$

where h is the magnetic hyperfine constant. The hyperfine frequency splitting within the electronic state becomes,

$$\delta\nu = h\left(\frac{J+\frac{1}{2}}{J(J+1)}\right). \tag{III.23}$$

It is straightforward to extract the magnetic hyperfine constants of the ground and excited state of the transition using equation III.23, with given hyperfine frequency splittings among the peaks of Fig. 3.10. The only problem we had to solve was to assign measured frequency splittings to the correct hyperfine transition (i.e. whether the splitting corresponds to the $|a-b|$, $|b-c|$, or $|c-a|$ transition). We have used the least square fitting method for all combinations of assignments, and picked the assignment which gave us the smallest residuals for the fit. Using the

Table 3.7: Relative frequency shifts of measured hyperfine splittings of the $^{183}W^{12}C$ in $[20.6]\Omega = 2, v' = 4 \leftarrow X^3\Delta_1, v" = 0$ transition. The 1 σ errors are shown inside the parentheses in the order of first parenthesis with the statistical uncertainty and the second parenthesis with the systematic uncertainty in relative frequencies. The residuals from the fit are shown in the third column.

Measured Line	Splitting (MHz)	Fit Residual (MHz)
$^{183}W^{12}C$, R(1), $\|a-b\|$	528(1.6)(0.3)	-2.3
$^{183}W^{12}C$, R(1), $\|b-c\|$	882(1.6)(0.5)	-1.5
$^{183}W^{12}C$, R(2), $\|a-c\|$	849(1.6)(0.5)	-9.8

wrong assignment made a significant increase in the residuals, which allowed us to reject it. The result of three independent frequency splittings with the correct assignments are shown in Table 3.7. Based on this assignment, we report the measured hyperfine constants to be $h_{3\Delta_1,v"=0} = -1171(4)$MHz and $h_{[20.6]\Omega=2,v'=4} = 1258(6)$MHz with 1σ fitting errors shown inside the parentheses. Detailed comparison with the calculated hyperfine constant will be shown in Chapter IV.

3.4.3 Ω-doublet constant

Both the $X^3\Delta_1$ state and the $[20.6]\Omega = 2$ state of WC have parity eigenstates in each of its J rotational levels, which are known as the Ω-doublet. These doublet structures have been studied by Brown [BCM87], where they have proposed a labeling convention of $|e\rangle$ levels for parity $+(-1)^J$ and $|f\rangle$ levels for parity $-(-1)^J$. The coupling between the rotational and electronic motion lifts the degeneracy of the parity eigenstates, causing energy splittings for states with $\Omega \neq 1$. Following ref. [BCM87], we write down the Hamiltonian for both states as,

$$H_{^3\Delta_1} = \pm\tilde{o}_{^3\Delta_1} J(J+1), \tag{III.24}$$

$$H_{[20.6]\Omega=2} = \pm\tilde{o}_{[20.6]\Omega=2}(J-1)J(J+1)(J+2), \tag{III.25}$$

where $\tilde{o}_{^3\Delta_1}$ and $\tilde{o}_{[20.6]\Omega=2}$ are the Ω-doublet constants. With this, the doublet frequency splitting shown in Fig. 3.11 can be fitted using,

$$\delta\nu = \pm 2\tilde{o}_{^3\Delta_1} J(J+1) \pm 2\tilde{o}_{[20.6]\Omega=2}(J-1)J(J+1)(J+2). \tag{III.26}$$

where the ± signs indicate 4 different possibilities of $\{+,+\}$, $\{+,-\}$, $\{-,+\}$, and $\{-,-\}$ for the fit. We note that the $\{-,+\}$, $\{-,-\}$ cases would give the same fit result as the $\{+,+\}$, $\{+,-\}$ cases, only with the opposite signs for the constants. As we only care about the magnitude of the doublet constants, this reduces the possibilities to 2 cases. The least square fit for two different cases of $\{+,+\}$ and $\{+,-\}$ both showed small residuals, and also revealed that the $2\tilde{o}_{^3\Delta_1} J(J+1)$ term is much larger than the $2\tilde{o}_{[20.6]\Omega=2}(J-1)J(J+1)(J+2)$ term. In other words, the first term was the main contribution to the observed frequency splitting. That made the second term irrelevant whether it was added or subtracted from the first term.

Fitting the Ω-doublet frequency splittings observed in the R(4) and R(5) lines of $^{182}W^{12}C$, $^{184}W^{12}C$, $^{186}W^{12}C$ isotopes gave the ground state Ω-doublet constant $\tilde{o}_{^3\Delta_1}$, and the upper bound of the excited state Ω-doublet constant $\tilde{o}_{[20.6]\Omega=2}$, which are shown in Table 3.8. Details of the fitting procedure, and the LIF measurements of the $^{182}W^{12}C$, $^{186}W^{12}C$ isotopes are shown in Appendix B. The isotope dependent doublet constants are all within the error bars of our extracted constants. The measured Ω-doublet constant $\tilde{o}_{^3\Delta_1}$ is used for the estimation of the difference in g-factors between the doublet levels, which will be discussed in detail in Chapter IV.

Table 3.8: The Ω-doublet constants of the $^3\Delta_1$ and $[20.6]\Omega = 2$ states are shown and compared. Ref. [WS12] shows the Ω-doublet constants of $^3\Delta_1$ for $^{184}W^{12}C$. The 1 σ fitting error is shown inside the parentheses for both experimental values.

Ω-doublet Constant	This Work (kHz)	Ref. [WS12] (kHz)
$\tilde{o}_{^3\Delta_1}$	418(18)	400(13)
$\tilde{o}_{[20.6]\Omega=2}$	< 1	

CHAPTER IV

Systematic and Statistical Uncertainties

In this Chapter, we will discuss the systematic and statistical uncertainty of the electron EDM experiment with WC molecule. The magnetic hyperfine constants and the Ω-doublet constants of the WC molecule reported in the previous chapter will be analyzed and related to the systematic uncertainties of the electron EDM measurement. The flux and the rotational temperature of the molecular beam are characterized, which sets the limit of the statistical sensitivity of the electron EDM experiment.

4.1 Systematic uncertainty

Thinking about an ideal case of an EDM measurement helps one to understand the systematic uncertainties in EDM experiments. Following eq. I.1, ideally we want a perfectly well known electric field being applied to the electron for the "signal" part, and a perfect electric field reversal relative to the magnetic field for the "noise" cancelation part. As this is not possible in reality, we need to estimate how well we know the electric field, and how accurately we could cancel out the magnetic field shifts in our system. With the WC system, the former is related to the magnetic hyperfine constant, and later is related to the Ω-doublet structure of the $^3\Delta_1, v" = 0$ ground state, which will be discussed mainly in this section.

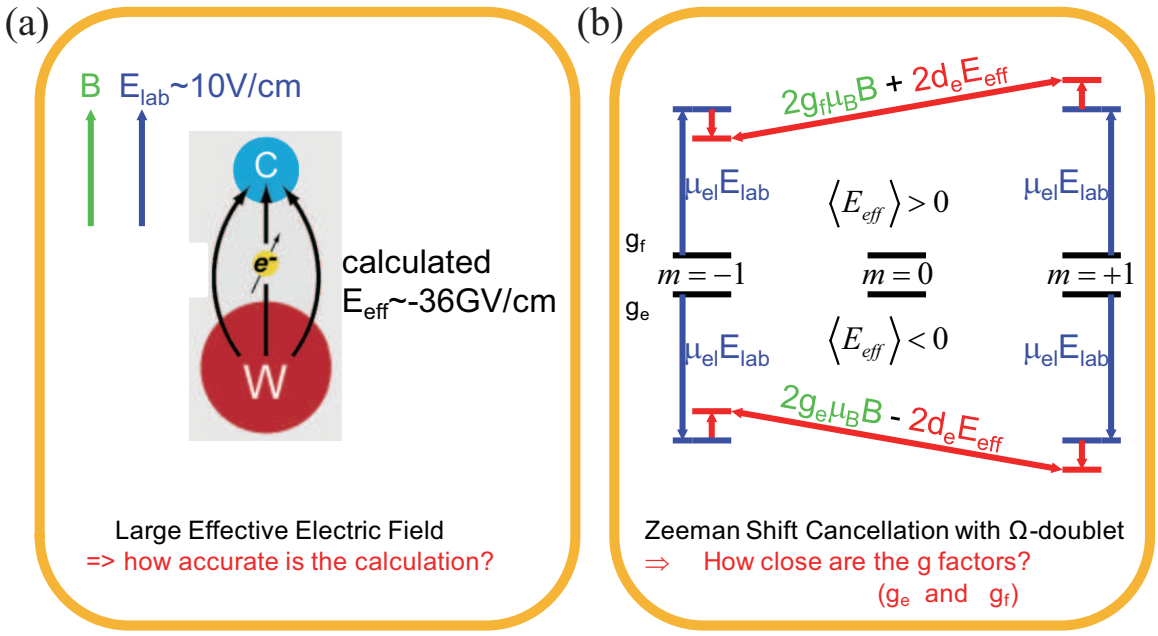

Figure 4.1: (a)Diagram of $\mathcal{E}_{\text{eff}}$ calculation and its uncertainty (b)Diagram of Zeeman shift cancelation scheme in the WC electron EDM experiment and its uncertainty.

4.1.1 Overview of systematic uncertainty analysis for the WC electron EDM experiment

The $X^3\Delta_1$ ground state of the WC molecule carries two main advantages for measuring the electron EDM, as shown in Fig. 4.1. The first advantage comes from the large $\mathcal{E}_{\text{eff}}$ being applied to the valence electrons of the molecule, which is due to the heavy tungsten nucleus. The second advantage is the use of internal comagnetometer [LMP+09] illustrated in Fig. 4.1(b), where we could cancel out the Zeeman shift term, which is the common mode in the top and bottom levels of the Ω doublet structure, and only leave the Stark shift term, which is proportional to d_e.

On the other hand, there are also uncertainties for two of these aspects and therefore careful analysis is required. As for the $\mathcal{E}_{\text{eff}}$, since there is no direct way of measuring the electric field inside the molecule, the uncertainty purely comes from the calculation itself. The calculation of $\mathcal{E}_{\text{eff}}$ require information on the electron wavefuc-

tion at the heavy nucleus of the molecule [San66]. Therefore it is strongly related to the hyperfine structure. In other words, comparing the calculated hyperfine constant with the experimental result could be a qualitative test of self consistency in the theoretical calculation of $\mathcal{E}_{\text{eff}}$.

The Zeeman shift cancelation scheme shown in Figure 4.1 also has room for systematic uncertainty, as the small difference in g-factors between the top and bottom doublet would result in imperfect cancelation. The magnitude of this systematic uncertainty can be written as $2\mu_B B\Delta g$, where μ_B is the Bohr magneton, B is the laboratory magnetic field, and Δg is the difference between g_e and g_f shown in Fig. 4.1. Petrov [Pet11] has shown that Δg is closely related to the energy splitting between the top and bottom levels of the Ω doublet. Utilizing this relation, we can calculate Δg based on Ω-doublet measurement, and assign systematic uncertainty to the electron EDM experiment.

4.1.2 Systematic uncertainty from $\mathcal{E}_{\text{eff}}$

In chapter III, we have reported the hyperfine constants of both the ground $^3\Delta_1, v" = 0$ state and excited $[20.6]\Omega = 2, v' = 4$ state. The part that we are interested in is the ground state hyperfine constant $h_{^3\Delta_1, v"=0}$, as it contains information of the WC electron wavefunction near the tungsten nucleus. As the $\mathcal{E}_{\text{eff}}$ field comes from the relativistic effect being applied to the WC valence electrons near the heavy nucleus [San66], the calculation of $\mathcal{E}_{\text{eff}}$ in a specific electronic state is closely linked to the calculation of the hyperfine constant in the same state. Therefore, the comparison of the calculated WC hyperfine constant $h_{^3\Delta_1, v"=0}$ with the experimental results could serve as a qualitative test of self consistency in the calculation of $\mathcal{E}_{\text{eff}}$.

To perform *ab initio* calculation of the WC molecule, a generalized relativistic effective core potential (GRECP) [TM99, MZT10] for the tungsten atom was generated. As a result, 60 core electrons ($1s{-}4f$) of W were explicitly excluded from

the correlation treatment. A basis set for W was constructed using the generalized correlated scheme [MTEK01] and it consists of $7s$-, $9p$-, $6d$-, $4f$- and $2g-$type contracted gaussians; such a basis is usually written as [7,9,6,4,2]. The aug-cc-pVTZ basis set [Dun89] reduced to [5,4,2,1] was used for carbon.

To evaluate $\mathcal{E}_{\text{eff}}$, one needs to compute the following parameter of the P,T-odd molecular Hamiltonian (discussed in Refs. [KFD$^+$87, KL95, TMP$^+$06]):

$$W_d = \frac{1}{\Omega d_e}\langle\Psi|\sum_i H_d(i)|\Psi\rangle, \tag{IV.1}$$

where Ψ is the wave function of the considered state $^3\Delta_1$, and Ω is the projection of total electronic momentum on the molecular axis directed from W to C,

$$H_d = 2d_e \begin{pmatrix} 0 & 0 \\ 0 & \boldsymbol{\sigma E} \end{pmatrix}, \tag{IV.2}$$

$\boldsymbol{E}$ is the inner molecular electric field, and $\boldsymbol{\sigma}$ are the Pauli matrices. In these designations, $\mathcal{E}_{\text{eff}} = W_d|\Omega|$.

The hyperfine constant $A_{||}$ for the $^3\Delta_1$ state is [1],

$$A_{||} = \frac{\mu_{\text{W}}}{I\Omega}\langle\Psi_{^3\Delta_1}|\sum_i \left(\frac{\boldsymbol{\alpha}_i \times \boldsymbol{r}_i}{r_i^3}\right)_z |\Psi_{^3\Delta_1}\rangle \tag{IV.3}$$

where $\mu_{\text{W}} = 0.11778471\mu_{\text{N}}$ [MCH$^+$93].

To calculate matrix elements IV.1 and IV.3, we used a two-step scheme, where one performs a correlation calculation for the valence and outer core electrons with the GRECP, followed by the nonvariational one-center restoration of the wave function at the inner core region of W (see [TMP$^+$06] for more details). A twenty electron correlation calculation was performed using the spin-orbit direct multireference configuration interaction (SODCI) approach [ALB04], accounting for the spin-orbit selection proce-

[1] For the case of $\Omega = 1 \rightarrow A_{||} = h$; for the case of $\Omega = 2 \rightarrow A_{||} = h/4$

Table 4.1: The hyperfine constants of $^{183}W^{12}C$ in the $[20.6]\Omega = 2, v' = 4 \leftarrow X^3\Delta_1, v" = 0$ transition is shown and compared. The 1 σ fitting error is shown inside the parentheses for both experimental values. The calculated value is believed to be correct at the 10% level.

Hyperfine Constant	This Work (MHz)	Ref. [WS11b] (MHz)	Calculated (MHz)
$h_{^3\Delta_1}$	-1171(4)	-1363(17)	-1192(?)
$h_{[20.6]\Omega=2}$	1258(6)		

dure [TMAB01]. As a basis set of one-electron functions for the SODCI calculation, we used the eigenvectors (natural orbitals) of some one-electron density matrix calculated at the scalar-relativistic coupled-clusters level with single and double cluster amplitudes using the CFOUR code [SGH+11].

$\mathcal{E}_{\text{eff}}$ and $A_{||}$ were calculated at R(W-C)=3.2248 a.u., which is close to the equilibrium distance. The calculated $A_{||}$ value is ~ -1192MHz and the $\mathcal{E}_{\text{eff}}$ value is ~ -36GV/cm. The sign of $\mathcal{E}_{\text{eff}}$ implies the field pointing in the opposite direction of the defined molecular axis. The influence of interaction with the low-lying electronic state $^3\Delta_2$ on the hyperfine structure will be discussed in the following subsection along with the Ω-doublet analysis.

We report the measured hyperfine constants of $h_{^3\Delta_1, v"=0}$ and $h_{[20.6]\Omega=2, v'=4}$ in Table 4.1. For the hyperfine constant of the $^3\Delta_1, v" = 0$ state, we compare our result with the previous results of Wang's [WS11b], which had a slightly larger uncertainty then our case. As seen from Table 4.1, our result of $h_{^3\Delta_1}$ had great agreement with the theoretical calculation. However, it disagreed with ref. [WS11b] at the 10% level. The disagreement was relatively large considering the uncertainties assigned on each experimental hyperfine constant. On the other hand, all three results of the $h_{^3\Delta_1}$ con-

stant are consistent at the 10% level. These results give information on the ground state electronic wave function at the nucleus of the molecule, which is strongly related to the effective electric field calculation of the valence electrons in WC. Therefore, the consistency between measured and calculated hyperfine constant of WC could be a qualitative test of effective electric field calculations.

4.1.3 Systematic uncertainty from Δg

The dominant systematic uncertainty of the electron EDM measurement with YbF molecules, which holds the current experimental limit, came from imperfect $\mathcal{E}_{\text{lab}}$ reversal combined with r.f. phase detuning [HKS+11]. The systematic error from this effect was at the 10^{-28} e-cm level. However, this will not be present in our case. Instead of reversing $\mathcal{E}_{\text{lab}}$ for the Zeeman shift cancelation, our measurement scheme shown in Fig. 4.1(b) uses the Ω-doublet levels of the $^3\Delta_1$ state, which are closely spaced spin states of opposite parity [LMP+09]. Our systematic uncertainty would come from a different source, which is the small difference in g-factors between the top and bottom doublet levels. The upper bound for this systematic uncertainty can be written as $2\mu_B B\Delta g$.

As mentioned previously in the introduction chapter, Δg is closely related to the energy splitting between the top and bottom levels of the Ω-doublet [Pet11]. We use the constant $\tilde{o}_{^3\Delta_1}$ reported in subsection 3.4.3 for the calculation of the g-factors of the top and bottom levels of the Ω-doublet. We need to consider the influence of interaction with the low-lying electronic state $^3\Delta_2$ on the hyperfine structure and g-factors of the $^3\Delta_1$ state of WC, where rough ten-electron calculations were performed (core states of $5s^25p^6$ of tungsten and $1s^2$ of carbon were excluded from the correlation treatment). The calculated off-diagonal *electronic* matrix elements are,

Table 4.2: Calculated values of the HFS as a function of J for the $^3\Delta_1$ state of WC. The second(third) and fifth(sixth) columns are the results obtained without(with) interaction from the $^3\Delta_2$ state taken into account.

J			J		
1	882.5	882.5	16	72.4	42.2
2	495.5	492.4	17	68.2	36.2
3	347.5	342.2	18	64.6	30.6
4	268.3	260.8	19	61.2	25.5
5	218.7	209.2	20	58.2	20.6
6	184.6	173.2	21	55.5	16.1
7	159.8	146.5	22	53.1	11.7
8	140.9	125.6	23	50.8	7.6
9	126.0	108.8	24	48.7	3.7
10	113.9	94.9	25	46.8	0.1
11	104.0	83.1	26	45.1	-3.7
12	95.6	72.9	27	43.4	-7.2
13	88.5	63.9	28	41.9	-10.5
14	82.4	55.9	29	40.5	-13.8
15	77.1	48.7	30	39.1	-17.0

$$\Delta/2 = B'\langle \Psi_{^3\Delta_1} | J^e_- | \Psi_{^3\Delta_2} \rangle \ = 0.8 \text{ cm}^{-1}, \tag{IV.4}$$

$$\frac{\mu_W}{I}\langle \Psi_{^3\Delta_1} | \sum_i \left(\frac{\boldsymbol{\alpha}_i \times \boldsymbol{r}_i}{r_i^3} \right)_- | \Psi_{^3\Delta_2} \rangle \ = 2742 \text{ MHz}, \tag{IV.5}$$

$$G_\perp = \langle \Psi_{^3\Delta_1} | J^e_- + S^e_- | \Psi_{^3\Delta_2} \rangle = 3.1. \tag{IV.6}$$

The required diagonal *electronic* matrix elements and excitation energies are taken from experiment: $B' = 0.509$ cm^{-1}, $A_\parallel = -1171$ GHz (this work), $G_\parallel = 0.022$ [WS11a], $D = 1.53$ a.u. [WS11b], $E_{^3\Delta_2} - E_{^3\Delta_1} = 1194$ cm^{-1} [RHJ08].

In table 4.2, the hyperfine splittings (HFS) calculated from E($F = J-1/2$)−E($F = J+1/2$) are given for each rotational level of the $^3\Delta_1$ state of WC. The hyperfine struc-

ture results were obtained by numerical diagonalization of the Hamiltonian, which was described in Ref. [Pet11]. Interaction with the $^3\Delta_2$ state equally influences the properties of the $|e\rangle$ and $|f\rangle$ states, whereas the interactions with 0^+ and 0^- states would lead to different properties between the $|e\rangle$ and $|f\rangle$ states. However, the influence of the latter interactions on the HFS is not considered in the present study due to the complexity of the WC spectrum. The experimental value of the Ω-doublet allows us to write,

$$B'^2 \left(\sum_n \frac{\langle \Psi_{^3\Delta_1} | J_+^e | \Psi_{n0^+} \rangle^2}{E_{^3\Delta_1} - E_{n0^+}} - \sum_m \frac{\langle \Psi_{^3\Delta_1} | J_+^e | \Psi_{m0^-} \rangle^2}{E_{^3\Delta_1} - E_{m0^-}} \right) = \pm 0.4 \text{ MHz}. \tag{IV.7}$$

Due to a large number of electronic states in the WC spectrum, it is hard to reproduce this value in *ab initio* calculations. However, we have estimated from our calculations that the matrix elements $\langle \Psi_{^3\Delta_1} | S_+^e | \Psi_{n0^\pm} \rangle$ are much smaller than $\langle \Psi_{^3\Delta_1} | J_+^e | \Psi_{n0^\pm} \rangle$ by absolute value. Therefore, we can write,

$$\sum_n \frac{2B' \langle \Psi_{^3\Delta_1} | J_+^e | \Psi_{n0^+} \rangle \langle \Psi_{^3\Delta_1} | J_+^e + S_+^e | \Psi_{n0^+} \rangle}{E_{^3\Delta_1} - E_{n0^+}} - \sum_m \frac{2B' \langle \Psi_{^3\Delta_1} | J_+^e | \Psi_{m0^-} \rangle \langle \Psi_{^3\Delta_1} | J_+^e + S_+^e | \Psi_{m0^-} \rangle}{E_{^3\Delta_1} - E_{m0^-}} \approx \pm 5 \cdot 10^{-5}. \tag{IV.8}$$

The ± sign in eqs. (IV.7) and (IV.8) comes from the fact that it has not been experimentally determined whether it is the $|e\rangle$ or $|f\rangle$ state that belongs to the lower Ω-doublet level. Taking this into account, the difference of the g-factors can be written as $|g_e - g_f| = 5 \cdot 10^{-5} \cdot J(J+1)$. It can also be shown that interaction with the $^3\Delta_2$ state leads to the same $J-$dependence of the g-factors for $|e\rangle$ and $|f\rangle$ levels:

$g_{e(f)} = 0.022 + \Delta G_{\perp}/2(E_{^3\Delta_2} - E_{^3\Delta_1}) \cdot (J+2)(J-1)$.

The smaller the difference between g_e and g_f is, the smaller the systematics would be coming from spurious magnetic fields. This difference depends on the electric field, which is shown in Fig. 4.2. Let us analyze the behavior of g-factors in this plot. At first glance, one expects that the difference between g_e and g_f could be made zero by increasing the electric field, since the external electric field mixes $|e\rangle$ and $|f\rangle$ levels. However, this only happens for the $|J = 1, F = 1/2, |M_F| = 1/2\rangle$ hyperfine levels of $^{183}W^{12}C$, which will be explained in subsection 4.1.4. Without a proper perturbation term from the hyperfine interaction, the difference between g-factors would eventually diverge as the electric field increases, which has been observed from PbO molecules [BHJD09]. This behavior was explained by M.G. Kozlov (see acknowledgements in [BHJD09]).

Applying the same analysis to the case of WC molecules, when the $J = 2$ level is mixed into $J = 1$ by the external electric field, the g-factor of the lower Ω-doublet level will have a slight decrease at very low electric field, and continuously increase as the field increases (here we suggest that the electronic g-factor is positive). In the absence of an external electric field, it was found that the initial value for the g-factor of the lower Ω-doublet level is larger than the g-factor of the higher one [DKD04]. Taking these two factors into account, one could understand the g-factor curves in Fig. 4.2(a) for isotopes with zero nuclear spin. Without the hyperfine interaction, the difference between g-factors would eventually diverge at higher electric fields. However, this was not shown in Fig. 4.2(a) due to a limited plot range for comparison purposes.

It can also be shown that whenever signs of the sums in Eqs. (IV.7) and (IV.8) are the same, the lower Ω-doublet level will have a larger g-factor (independently from the parity of its state). This is true for WC since $\langle \Psi_{^3\Delta_1} | S^e_+ | \Psi_{n0^\pm} \rangle$ is much smaller than $\langle \Psi_{^3\Delta_1} | J^e_+ | \Psi_{n0^\pm} \rangle$ by absolute value. Therefore, we arrive at the same conclusion

that g-factors divergence at high electric field for WC isotopes with zero nuclear spin.

In Fig. 4.2 the calculated g-factors for the J=1 Ω-doublet levels of the $^3\Delta_1$ state of WC are given as functions of electric field. Here, for simplicity we assume that the value of $g = 0.022$ [WS11a] belongs to a high Ω-doublet level of spinless isotopes. Further experimental investigation would be required to confirm this. However, even if it were the opposite case, it would only shift all the curves in the figure slightly down, leaving their relative positions unchanged.

The maximum EDM induced Stark splitting $2\mathcal{E}_{\text{eff}} \cdot d_e$ is only reached for a fully polarized molecule. For a finite electric field, the Stark splitting obtained from numerical calculations is plotted in Fig. 4.3.

As shown in Fig. 4.2(a), we can get $\Delta g = 0.00002$ for isotopes with zero nuclear spin at $\mathcal{E}_{\text{lab}} = 10\text{V/cm}$, which is enough laboratory electric field to fully polarize the WC molecule. Using this estimation of Δg, we get $\sim 100\mu\text{Hz}$ of systematic shift with $\sim \mu\text{G}$ control of the magnetic field. This would limit our EDM sensitivity at $\delta d_e \approx 10^{-29}$ e-cm level when $\mathcal{E}_{\text{eff}} \sim -36\text{GV/cm}$.

4.1.4 Further suppression of systematic uncertainty from Δg

There is an additional interesting feature shown in Fig. 4.2(a), where the g-factors cross at $\mathcal{E}_{\text{lab}} = 2V/cm$ for the $|J = 1, F = 1/2, |M_F| = 1/2\rangle$ hyperfine levels of the $^{183}\text{W}^{12}\text{C}$ isotope due to hyperfine interaction. For the $|J = 1, F = 1/2, |M_F| = 1/2\rangle$ and $|J = 1, F = 3/2, |M_F| = 1/2\rangle$ states, the perturbing state is the nearest hyperfine energy level, which is simply each other ($|J = 1, F = 3/2, |M_F| = 1/2\rangle$ is the perturbing state for $|J = 1, F = 1/2, |M_F| = 1/2\rangle$ and vice versa). Note that for $A_{||} < 0$, the $|J = 1, F = 1/2, |M_F| = 1/2\rangle$ level is higher than the $|J = 1, F = 3/2, |M_F| = 1/2\rangle$ level. Therefore, the energy denominator for the $|J = 1, F = 1/2, |M_F| = 1/2\rangle$ levels in perturbation theory will have the opposite sign compared to the molecule without hyperfine structure. Accordingly, if the mixing by the external electric field of

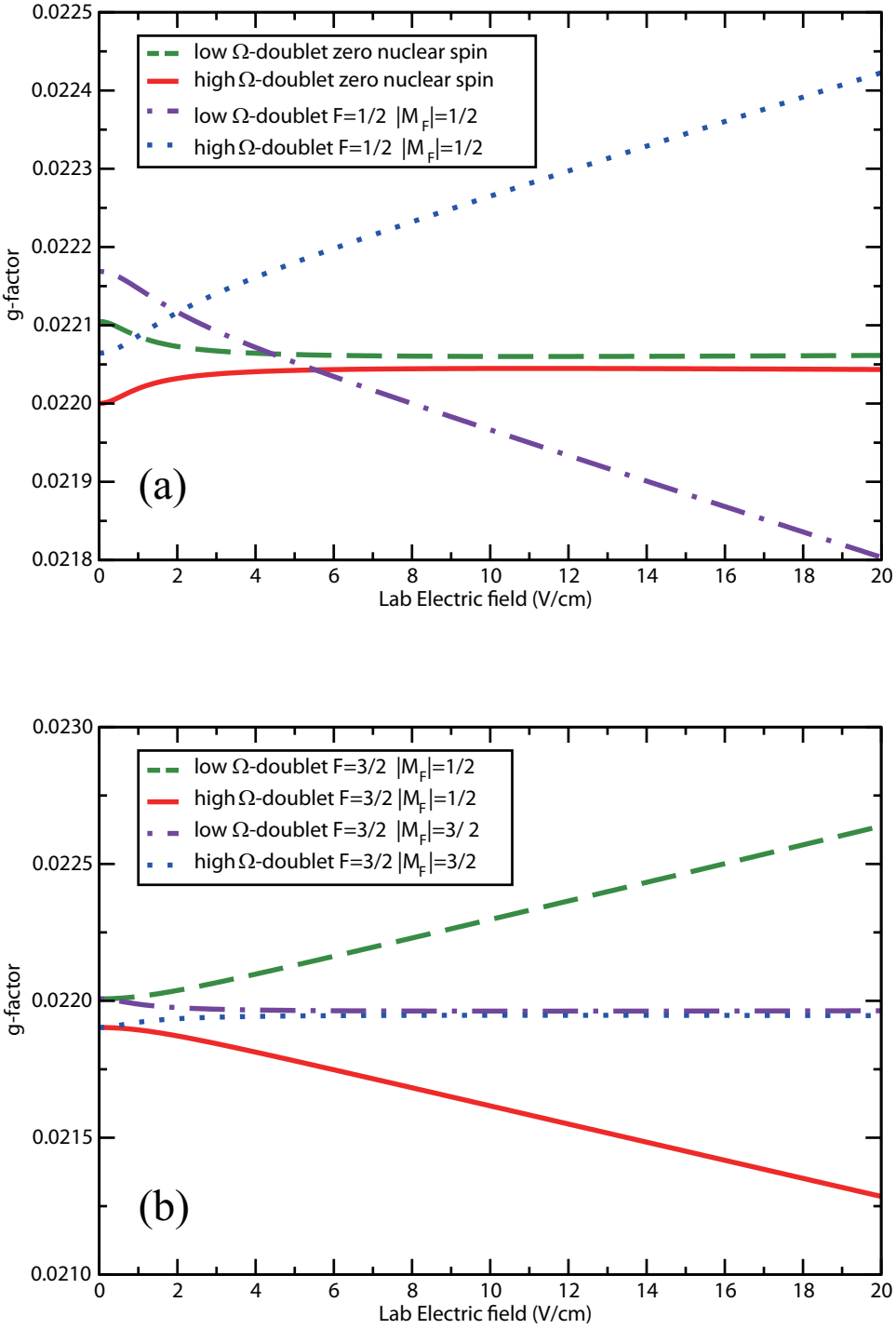

Figure 4.2: (a)Calculated g-factor curves for the $|J = 1, F = 1/2, |M_F| = 1/2\rangle$ hyperfine levels of $^{183}W^{12}C$, and $J = 1$ rotational levels of WC isotope with zero nuclear spin. There is a g-factor crossing point at 2V/cm for the $|J = 1, F = 1/2, |M_F| = 1/2\rangle$ hyperfine levels of $^{183}W^{12}C$. (b)Calculated g-factor curves for the $|J = 1, F = 3/2, |M_F| = 1/2\rangle$ hyperfine levels of $^{183}W^{12}C$, and the $|J = 1, F = 3/2, |M_F| = 3/2\rangle$ hyperfine levels of $^{183}W^{12}C$

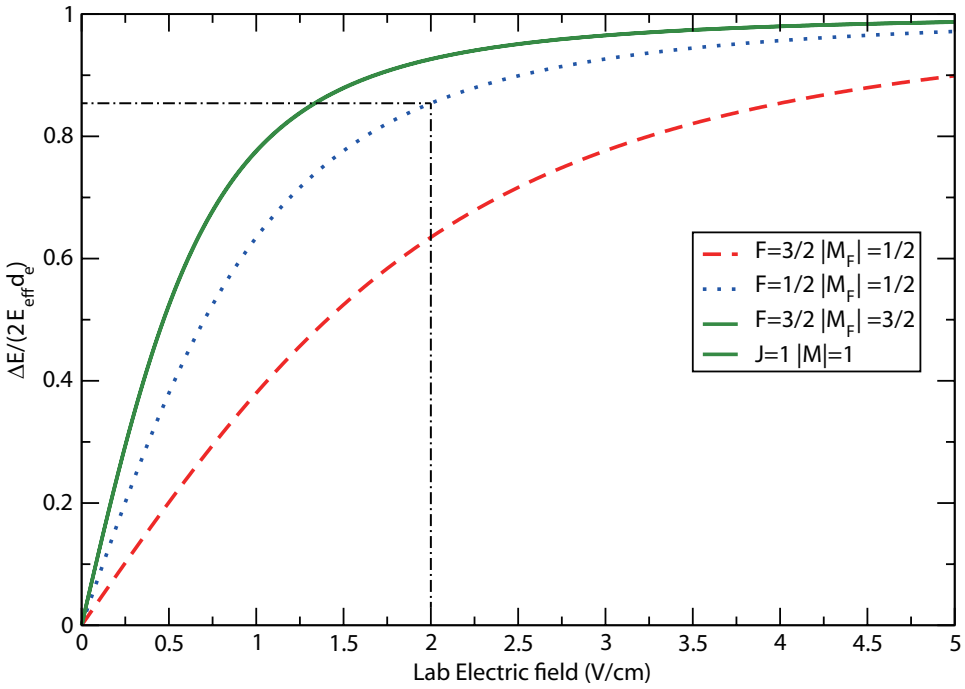

Figure 4.3: Calculated EDM induced Stark splitting between $\pm M_F$ levels of the $|J = 1, F = 1/2\rangle$; $|J = 1, F = 3/2\rangle$ and $J = 1$ states. All the curves are normalized by the maximum EDM induced Stark splitting, $2\mathcal{E}_{\text{eff}} \cdot d_e$. The dot-dash line shows the EDM induced Stark splitting between $\pm M_F$ levels of $|J = 1, F = 1/2\rangle$ state at $\mathcal{E}_{\text{lab}} = 2V/cm$.

the $|J = 1, F = 3/2, |M_F| = 1/2\rangle$ level is taken into account, the lower Ω-doublet level of the $|J = 1, F = 1/2, |M_F| = 1/2\rangle$ state will have a smaller g-factor with increasing electric field. As the initial value for the g-factor of the lower Ω-doublet level is larger than the g-factor of the higher Ω-doublet level, the corresponding curves for g_e and g_f are crossed. On the other hand, for the $|J = 1, F = 3/2, |M_F| = 1/2\rangle$ level, the perturbing state is the higher lying $|J = 1, F = 1/2, |M_F| = 1/2\rangle$ state. Therefore the g-factor curves shown in Fig. 4.2(b) do not cross for the $|J = 1, F = 3/2, |M_F| = 1/2\rangle$ level. The perturbing state of the $|J = 1, F = 3/2, |M_F| = 3/2\rangle$ level is the hyperfine state of the much higher lying $J = 2$ level, which is the $|J = 2, F = 3/2, |M_F| = 3/2\rangle$ state. As a result, the g-factor curves of the $|J = 1, F = 3/2, |M_F| = 3/2\rangle$ level in Fig. 4.2(b) resembles the g-factor curves for isotopes with zero nuclear spin shown in Fig. 4.2(a).

Utilizing the g-factor crossing point of the $|J = 1, F = 1/2, |M_F| = 1/2\rangle$ hyperfine levels of the $^{183}W^{12}C$ isotope, one could further suppress systematic uncertainty coming from Δg. There are two main factors to check before we could consider using this crossing point for the electron EDM measurement.

The most important factor to check is, how much $\mathcal{E}_{\text{eff}}$ field we would get at the g-factor crossing point with a given $\mathcal{E}_{\text{lab}}$. As the crossing point lies at $\mathcal{E}_{\text{lab}} = 2\text{V/cm}$, which is not enough laboratory electric field to fully polarize the WC molecule, we would not get the full $\mathcal{E}_{\text{eff}} \sim -36\text{GV/cm}$. However, as shown on Fig. 4.3, $\mathcal{E}_{\text{lab}} = 2\text{V/cm}$ applied to the $|J = 1, F = 1/2, |M_F| = 1/2\rangle$ state would still give 85% of EDM induced Stark splitting, compared to the fully polarized case. In other words, we only lose 15% of the $\mathcal{E}_{\text{eff}}$ field, and in return we get effectively zero difference in g-factors, which would suppress the systematics even further.

The second factor to consider is the slope of the g-factor curves at the crossing point. As we have limited $\mathcal{E}_{\text{lab}}$ stability, the uncertainty in $\mathcal{E}_{\text{lab}}$ would get transferred to the uncertainty in g-factors at the crossing point. A simple calculation of $2\times$ "$\mathcal{E}_{\text{lab}}$

field stability"×"the slope of the g-factor curve at the crossing point" would give Δg. With ∼mV/cm control of the $\mathcal{E}_{\rm lab}$ field, we get $\Delta g = 0(5) \times 10^{-8}$, where the number inside the parenthesis shows the uncertainty due to $\mathcal{E}_{\rm lab}$ field stability. In this particular example, Δg is at least ~ 500 times smaller than the case of isotope with zero nuclear spin. As a result, the systematics coming from Δg would also be suppressed by the same factor.

There is a minor drawback of this EDM measurement scheme in terms of statistics. One is due to the relatively low natural abundance of 14% for the ^{183}W isotope, which is about half of the most abundant ^{184}W isotope with zero nuclear spin. The other drawback comes from the small Clebsch-Gordan coefficient for the hyperfine transition. As discussed previously, the intensity ratios of the hyperfine transitions in the R(1) line follows $[I_a : I_b : I_c = 9 : 1 : 5]$, and the $|J = 1, F = 1/2\rangle$ EDM state can only couple to the $|J = 2, F = 3/2\rangle$ excited state, which corresponds to the c transition, the second strongest. With these two factors, the electron EDM measurement scheme using the g-factor crossing points of the $|J = 1, F = 1/2, |M_F| = 1/2\rangle$ hyperfine levels of the ^{183}W isotope would suffer a factor of 2 loss in statistics compared with the EDM measurement using a spinless isotope. However, this is a small loss compared to the factor of 500 gain in systematic uncertainty, therefore it would become a useful alternative electron EDM measurement scheme with enhanced comagnetometer performance. Similar effect can be expected from an electron EDM experiment using the ^{2}07PbO isotope with a hyperfine interaction. However, the g-factor crossing point of the ^{2}07PbO isotope happens at a higher $\mathcal{E}_{\rm lab}$ of 11V/cm, and it would also have a bigger loss in $\mathcal{E}_{\rm eff}$ field at the 25% level due to insufficient polarization of the molecules.

4.2 Statistical uncertainty

Due to the reasons explained in the previous section, we believe the WC electron EDM measurement would be limited by statistics rather than the systematic uncertainties at this point. In this section, we analyze the beam properties in order to show the achievable level of statistical sensitivity limit of the electron EDM measurement, and also discuss possible ways to improve this limit.

4.2.1 Beam properties related to statistics

The spectrum of the WC molecule gives much information about the beam properties. The height of each peak in Fig. 3.10 and 3.11 represents the molecular flux at a given electronic, vibrational, and rotational quantum state. Conversely, knowing the quantum states and the scattering rate of the transition, we can estimate the density of molecules within the detection volume. The Doppler broadened linewidth can be used for calculation of the beam divergence, and the axial velocity can be calculated from the time delay between the triggering of the gas valve and the PMT gate.

As the proposed electron EDM measurement scheme uses the WC molecules in their rotational and vibrational ground state of the $X^3\Delta_1$ state [LMP$^+$09], estimation of fractional rotational ground state population becomes important. Intuitively, more molecules would be in their rovibrational ground state as the internal temperature of the beam cools down by the buffer gas collision. From statistical physics, the probability of the rotational ground state population within the $X^3\Delta_1, v" = 0$ state at temperature T can be calculated from the following equation,

$$P(J", T) = \frac{(2J" + 1)Exp[-\frac{hc}{kT}[BJ"(J" + 1)]]}{\sum_{J=0}^{J_{max}}(2J + 1)Exp[-\frac{hc}{kT}[BJ(J + 1)]]}, \qquad \text{(IV.9)}$$

where B is the ground state rotational constant given by ref. [SSM02]. Figure 4.4 shows the fractional rovibrational ground state ($v' = 0, J' = 1$) population at different

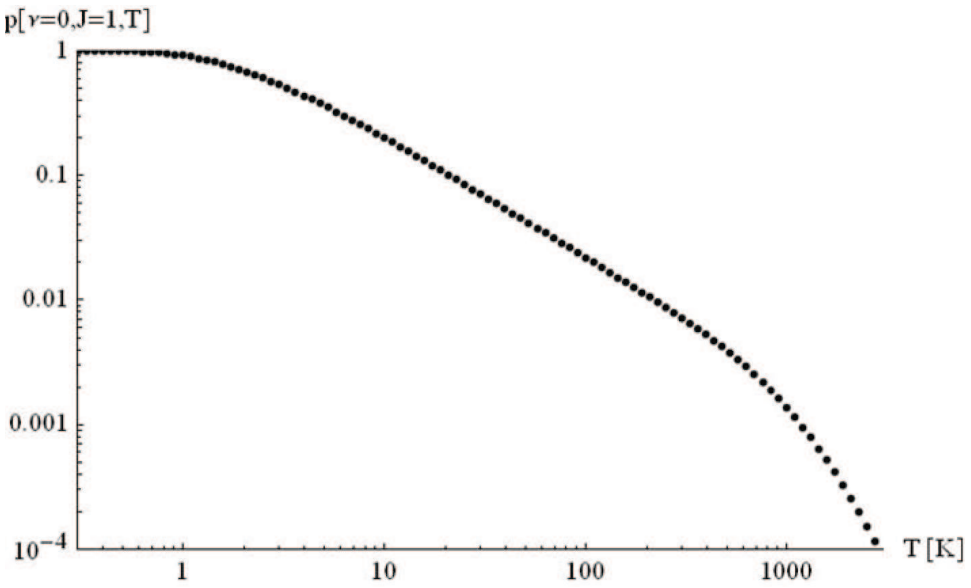

Figure 4.4: Fractional ro-vibrational ground state ($v = 0, J = 1$) population at different temperatures ranging from 0.3K to 3000K. The fraction converges to 1 as the temperature goes below 1K.

temperatures ranging from 0.3K to 3000K. In chapter III, we discussed the general trend of the R(1) lines being stronger than the R(2) lines for all the measured isotopes. This condition of $R(1) > R(2)$, combined with equation IV.9 gives an upper rotational temperature limit of $T_{rot} < 5.5k$. Therefore, we expect a minimum of 35% of the WC molecules to be at their rovibrational ground state when $T_{rot} = 5.5k$, which can be seen on fig. 4.4. For better estimation of the rotational temperature, accurate ratios among multiple rotational lines are required.

All the parameters mentioned above are listed in Table 4.3. We separate the directly measured quantities from the calculated quantities. In particular, the Frank Condon factor has been estimated based on dispersed fluorescence spectroscopy of the same transition [SSM02]. The number of WC molecules within the detection volume has been estimated based on the geometric efficiency, quantum efficiency, scattering rate of the transition, and the Frank Condon factor. These parameters will be used for calculation of the statistical sensitivity limit of the electron EDM experiment in

the following subsection.

4.2.2 Current level of statistical uncertainty and possible improvements

The EDM of an electron, d_e, inside a fully polarized WC molecule would produce a frequency shift of $\Delta\nu_{\mathrm{EDM}} = 2d_e\mathcal{E}_{\mathrm{eff}}/h$. The statistical uncertainty of the EDM shift is defined by the Fourier-limited frequency resolution of $\Delta\nu_{\mathrm{stat}} = 1/2\pi\tau\sqrt{\dot{N}\times T}$, where τ is the interrogation time and $\dot{N}$ is the rate of measurement, and T is the duration of measurement. Therefore, we can write down the expression for the statistical uncertainty of d_e as,

$$\delta d_e = \frac{h}{4\pi\tau\mathcal{E}_{\mathrm{eff}}\sqrt{\dot{N}\times T}}. \tag{IV.10}$$

From eq. IV.10, longer interrogation time, larger effective electric field, and more number of measurements result in smaller statistical uncertainty of d_e. Going back to Table 4.3, one can make the connections between the beam properties and the parameters in eq. IV.10. A slower beam axial velocity would give a longer interrogation time at fixed distance. A lower beam divergence would increase the molecular density within the LIF probe laser volume, which would result in a higher photon scattering rate. A colder rotational temperature would also enhance the photon scattering rate as more molecules would be in their rovibrational ground state.

The list of measured and calculated parameters in eq. IV.10 is shown in Table 4.4. The current status of the experiment gives a projected statistical uncertainty of $\delta d_e = 5\times10^{-27}e-cm/\sqrt{Day}$. From our systematic uncertainty analysis, we believe this would be the dominant term that limits our electron EDM measurement sensitivity, which is slightly above the current experimental limit [HKS$^+$11].

One possible improvement on this limit could come from extension of the WC beam line to increase the interrogation time. Due to the EDM sensitive $X^3\Delta_1$ state being in the ground state of WC, our interrogation time is only limited by the time of

Table 4.3: The list of measured and calculated parameters related to the WC molecular beam.

Parameter	Measured	Calculated
Beam Divergence	$0.00041sr$	
Beam MFP	$\sim 5m$	
Beam Axial Velocity	$650m/s$	
Distance Between Source and Probe	$75cm$	
Geometric Photon Collection Efficiency		0.003
Quantum Efficiency of Photo Multiplying Tube		0.1
Franck Condon Factor of $v' = 4 \leftarrow v" = 0$ excitation and $v' = 4 \rightarrow v" = 0$ decay		0.0001
WC Molecules within detection volume		$\sim 10^7 WC/pulse$
T_{rot}	$< 5.5K$	
Fractional Ro-vibrational Ground State		$> 35\%$

Table 4.4: The list of measured and calculated parameters related to electron EDM experiment.

Parameter	Measured	Calculated
Interrogation Time (τ)	$1.25ms$	
Photon Count Rate ($\dot{N}$)	$5photons/s$	
Effective Electric Field ($\mathcal{E}_{\text{eff}}$)		$54GV/cm$
Projected $\delta d_{e,stat}$		$5 \times 10^{-27} \frac{e-cm}{\sqrt{Day}}$

flight of the molecules, not by the lifetime of the state. As seen in Table 4.3, our beam has low divergence and long MFP, therefore extending the beam line of the molecules could be an option for us in order to increase the time of flight. However, there is also a chance that we might lose molecular flux passing through the fluorescence detection volume as we extend the beam line. From a conservative estimate, we believe a factor of $2 \sim 3$ of beam line extension is plausible without the lost of fluorescence detection rate.

Another prospect of improvement for statistics comes from the Franck Condon factor. From the dispersed fluorescence spectroscopy of ref. [Mor11], it was shown that the $v' = 4 \leftarrow v" = 0$ vibrational excitation of the $[20.6]\Omega = 2 \leftarrow X^3\Delta_1$ transition happens at ~ 100 times lower rate than the $v' = 1 \leftarrow v" = 0$ vibrational excitation of the same electronic transition. Therefore, probing a new stronger transition of $[20.6]\Omega = 2, v' = 1 \leftarrow X^3\Delta_1, v" = 0$ at a known wavelength of 545nm [SSM02] could give us a factor of 100 gain in $\dot{N}$. Combining the gains from the vacuum system and the laser system, the statistical uncertainty of d_e is expected to reach $10^{-28}e - cm/\sqrt{Day}$ level in the near future.

CHAPTER V

Conclusion

In this thesis, we have investigated the electron EDM measurement scheme using the $X^3\Delta_1$ ground state of WC molecules, where the focus was on identifying and estimating the main systematic and statistical uncertainties. A well collimated and internally cold beam of WC was developed for an electron EDM search in the $X^3\Delta_1$ state of the molecule. We have shown high resolution LIF spectroscopy of the $[20.6]\Omega = 2, v' = 4 \leftarrow X^3\Delta_1, v" = 0$ transition to extract molecular constants relevant to the electron EDM measurement scheme.

The ground state hyperfine constant, $h_{3\Delta_1,v"=0}$, was measured and compared with theoretical calculations to show self consistency in effective electric field calculations at a 10% level. The ground state Ω-doublet constant, $\tilde{o}_{^3\Delta_1}$, was measured to give the g-factor curves for top and bottom doublet levels, and this also allowed us to estimate the systematic uncertainty coming from imperfect Zeeman shift cancelation in our EDM measurement scheme. The result leads to systematics of $\delta d_e \approx 10^{-29} e - cm$ level with $\sim \mu$G control of the magnetic field. Also an alternative EDM measurement scheme using the g-factor crossing point of hyperfine levels of $^{183}W^{12}C$ isotope was shown, where the systematics could be suppressed even further. This crossing point of g-factors only happens with molecular isotopes with non-zero nuclear spin.

As for the statistical uncertainty, several beam properties such as the flux, velocity,

divergence, and rotational temperature were characterized. These properties were linked to the Fourier-limited frequency resolution of the EDM induced Stark shift measurement. The current statistical sensitivity limit was calculated to be $\delta d_e = 5 \times 10^{-27} e - cm/\sqrt{Day}$. Possible improvements coming from extension of the beam line and the Frank Condon factor were discussed.

We can summarize the main attractive features of a WC electron EDM experiment as, (i) verified calculation of large $\mathcal{E}_{\text{eff}}$, (ii) use of internal comagnetometer with Ω-doublet structure, (iii) further suppression of systematics due to g-factor crossing point, and (iv) unlimited lifetime of the EDM sensitive state, $X^3\Delta_1$. The former two features are shared by two other molecule based EDM experiments, which are the $^3\Delta_1$ metastable states of Thorium Oxide (ThO) [VCG$^+$10] and Hafnium Fluoride/Thorium Fluoride ion (HfF$^+$/ThF$^+$) [LBL$^+$11]. However, the later two features are unique properties of the WC system. Based on our analysis, we believe the WC system has many advantages for electron EDM measurement including some unique properties showing a lot of promise for future generation experiments.

It has been more than 50 years since the original proposal of Ramsey and Purcell about the possible existence of a permanent EDM [PR50]. Since then, the field of EDM experiments has grown continuously to play a major role in testing fundamental symmetry violations. Recently there have been various systems proposed for electron EDM experiments [AMG07, BHJD09, FW09, Hei, HKS$^+$11, LBL$^+$11, LMP$^+$09, RCSD02, SR06, VCG$^+$10], each having their own advantages.

In Table 5.1, we show the list of some of the on-going electron EDM experiments in atomic and molecular systems. Full list of EDM experiments can be found in Ref. [Kir]. Instead of listing the detailed experimental parameters, we are only showing the key characteristics of each experiment here. If any one of these experiments claims a non-zero measurement of the electron EDM, perhaps the most certain way of testing its validity is to confirm it with a measurement from a completely different

Table 5.1: The list of the electron EDM experiments with their characteristics.

Institution	Experiment	Characteristics
ACME: Harvard-Yale Ref. [VCG$^+$10]	ThO Beam	High flux cryogenic beam Internal Comagnetometer ($^3\Delta_1$)
Imperial College Ref. [HKS$^+$11]	YbF Beam	Current experimental limit of d_e
JILA Ref. [LBL$^+$11]	HfF^+ ion trap	Long coherence time τ Internal Comagnetometer ($^3\Delta_1$)
Oklahoma Ref. [SR06]	PbF Beam	Internal Comagnetometer ($^2\Pi_{1/2}$)
Penn State Ref. [FW09]	Trapped Cs	Long coherence time τ
Univ. of Michigan Ref. [LMP$^+$09]	WC Beam	Internal Comagnetometer ($X^3\Delta_1$) g-factor crossing
Yale Ref. [BHJD09]	PbO vapor cell	Internal Comagnetometer (a(1)) g-factor crossing

system. Therefore I believe that diversity in the field will be the key to successfully announcing the discovery of a permanent EDM in the future.

In my opinion, the most interesting aspect of the EDM experiment is in the error bars of the measurements. For many cases, the importance of error analysis lies in proving the validity of a possible existence of a "signal". However, when even a null measurement has a significant meaning, one needs to pay extra attention to the experimental uncertainties. This is the case for the EDM experiments, where the null measurement could serve as a constraint for particle physics theories. Therefore, rigorous uncertainty analysis is crucial. I hope the ground work I have done here on

analyzing the uncertainties of the WC electron EDM measurement scheme becomes fruitful someday. With innovative ideas and active collaborations throughout various fields, the discovery of a non-zero EDM measurement would no longer only be a dream.

APPENDICES

APPENDIX A

Frequency Calibration

The uncertainty in relative frequency measurement could be divided into statistical uncertainty and systematic uncertainty. First we describe the way we characterize the statistical uncertainty. We have measured one of the hyperfine splitting of the tungsten transition multiple times and compared the results with the previously known number. Figure A.1 shows a histogram of the relative frequency shift measurements between $^{183}\mathrm{W}(a)$ and $^{183}\mathrm{W}(b)$ of the $^7S_3 \rightarrow {}^7P_4$ transition, which essentially gives the hyperfine splitting of the $^7S_3$ state as shown on fig. 3.5. The results were compared with the previous measurements from ref. [BDT79]. The width of the histogram corresponds to the statistical uncertainty of the measurement, which was given as 1.6MHz from the fit.

In order to test for a possible systematic uncertainty in relative frequency measurements from the wavelength meter, we measured the known Ytterbium(Yb) isotope shifts. Ytterbium was chosen due to a notable high precision isotope shift measurements from Natarajan group [PSK$^+$09].

Having relatively low melting point, Yb atomic beam was produced by conventional method of resistively heated oven, rather than the technique we described in section 2. Multiple apertures along the beam line minimized the Doppler linewidth.

Table A.1: Our measurements of Yb isotopes and hyperfine structure are shown as relative shift from ^{176}Yb and compared with ref. [PSK$^+$09]. The 1 σ errors are shown inside the parentheses. As for our results, we show two separate sources of errors, first parenthesis showing the statistical uncertainties and the second parenthesis showing the systematic uncertainties in frequency measurements.

Transition	Shift from ^{176}Yb (MHz)	
	This work	Ref. [PSK$^+$09]
^{173}Yb$_{(7/2\rightarrow5/2)}$	-1426.3(1.6)(3.6)	-1431.872(60)
^{171}Yb$_{(1/2\rightarrow1/2)}$	-1170.6(1.6)(3.6)	-1177.231(60)
^{176}Yb	0(1.6)(3.6)	0(60)
^{174}Yb	955.2(1.6)(3.6)	954.832(60)
^{172}Yb	1952.6(1.6)(3.6)	1954.852(60)
^{170}Yb	3235.5(1.6)(3.6)	3241.177(60)
^{173}Yb$_{(5/2\rightarrow5/2)}$	3258.8(1.6)(3.6)	3266.243(60)
^{168}Yb	4613.4(1.6)(3.6)	4609.960(60)
^{171}Yb$_{(3/2\rightarrow1/2)}$	4758.3(1.6)(3.6)	4759.440(60)
^{173}Yb$_{(5/2\rightarrow3/2)}$	4762.4(1.6)(3.6)	4762.110(60)

A tunable frequency doubled diode laser system (Toptica DL pro) generated 555.6 nm light for the LIF spectroscopy on the $^1S_0 \rightarrow {}^3P_1$ transition of Yb. Yb has 7 isotopes, ^{168}Yb $\sim$ ^{176}Yb, with 2 of them, ^{171}Yb and ^{173}Yb, having hyperfine structure. Detailed analysis on Yb spectrum is omitted, as it goes outside the subject of this section.

We compare the center line positions of all of our Yb isotopes and hyperfine structure measurements with ref. [PSK$^+$09], which are shown in Table A.1. Figure A.2 shows the plot of Table A.1 in black squares, as well as the red solid line showing the least square linear fit. Ideally, this line should have slope of 1, and intercepting at 0. Our fit gave a slope of 0.9990(6), and the intercept at 2.0(1.7)MHz with 1 σ errors inside the parenthesis. The error of the slope, which is 6×10^{-4}, represents the fractional uncertainty over the measured frequency range. Accordingly, we can

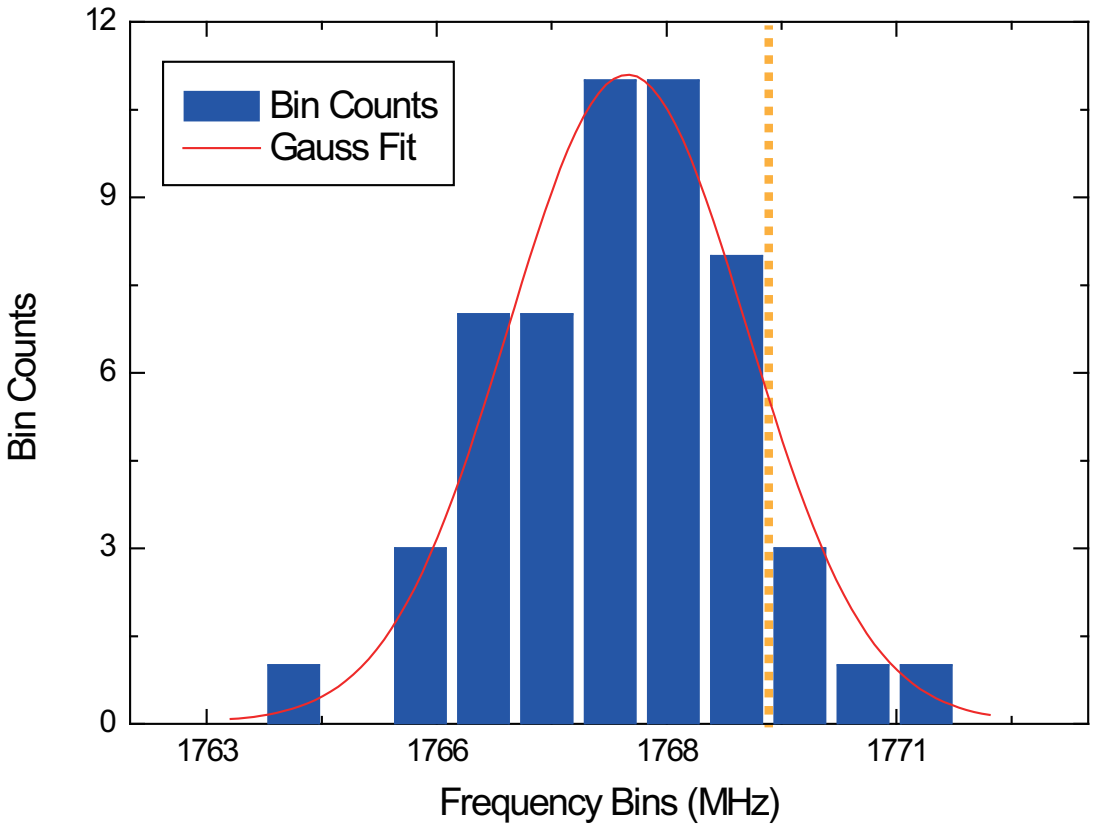

Figure A.1: The histogram of relative frequency shift between ^{183}W(a) and ^{183}W(b) of the $^7S_3 \rightarrow {}^7P_4$ transition is shown for 53 independent measurements. The Gauss fit for the histogram is shown in red solid line and the reference line position is shown in yellow dashed line. The uncertainty of the reference measurement is 42kHz which is within the thickness of the dashed line.

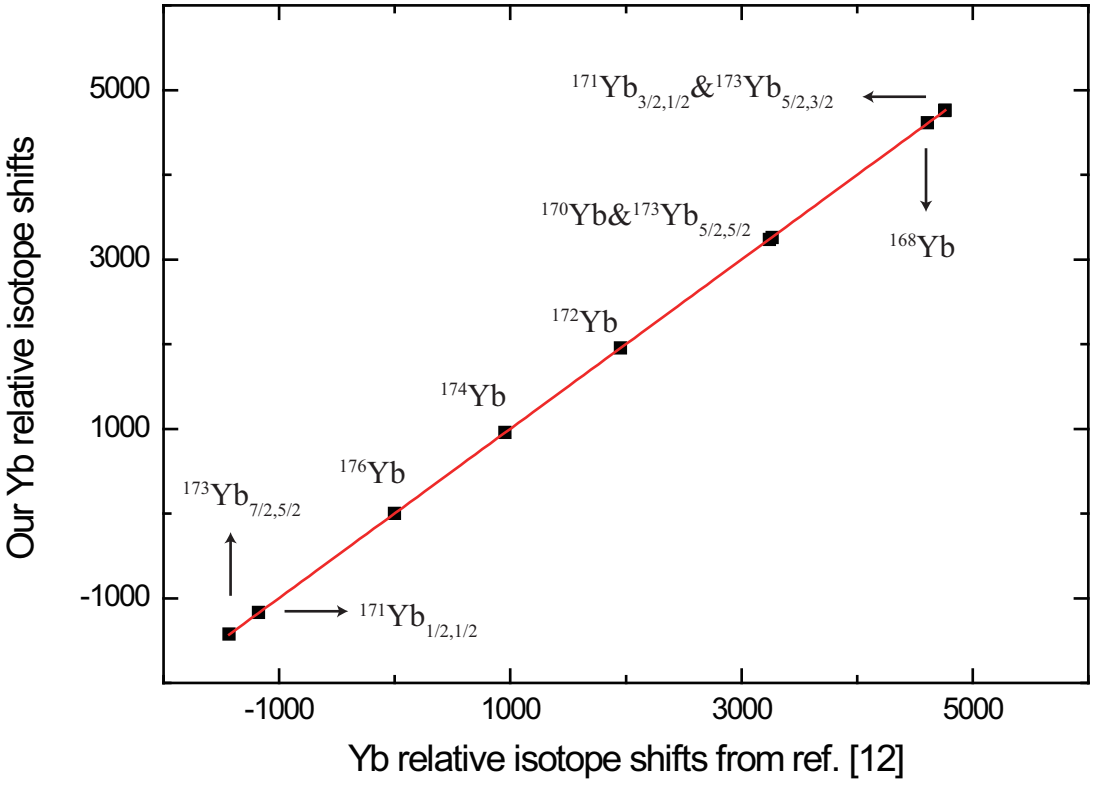

Figure A.2: Our relative frequency measurements of Yb isotopes and hyperfine structure are shown in black squares. The uncertainty of both ours and the reference measurements are within the symbols. The red solid line shows the least square linear fit of the data points.

assign systematic uncertainty of 3.6MHz over the range of 6GHz in the case of Yb isotope shift measurements at 555.6 nm transition. By assuming that the wavelength meter would perform in a similar way at the wavelength range of 385 nm - 410 nm, we can apply these results for the estimation of systematic uncertainty of tungsten transitions being studied in this work.

In conclusion, we report 1.6MHz of statistical uncertainty and 6×10^{-4} of fractional systematic uncertainty for the frequency measurements from our wavelength meter. The fractional systematic uncertainty converts to 60kHz for the 384.9 nm transition, 1.2MHz for the 400.9 nm transition, and 2.4MHz for the 407.4 nm transition. Adding statistical and systematic uncertainties in quadrature, the total uncertainty of frequency measurements are, 1.6MHz for the 384.9 nm transition, 2.1MHz for the 400.9 nm transition, and 2.9MHz for the 407.4 nm transition.

APPENDIX B

WC Ω-doublet Fitting

The R branches of the $[20.6]\Omega = 2, v' = 4 \leftarrow X^3\Delta_1, v" = 0$ transition of $^{182}W^{12}C$ and $^{186}W^{12}C$ isotopes are shown in Figs. B.1 and B.2. The Ω-doublet splittings observed in the R(4) and R(5) lines of these two isotopes combined with the results of the $^{184}W^{12}C$ isotope shown in Fig. 3.11 are listed in the second column of table B.1. From these, we couldn't extract any isotope dependence of the Ω-doublet constant from our data as we did not have enough precision on relative frequency shift measurement of the doublet splittings. The isotope dependence of the Ω-doublet constant comes from the difference in reduced mass, which is in $\sim 0.1\%$ level [WS12], however, our measured frequency splittings have an uncertainty in $\sim 10\%$ level dominated by the fitting error. This is why we had to fit the measured Ω-doublet splittings from all three isotopes using the same fit function of eq. III.26. As a result, we report the isotope independent ground state Ω-doublet constant $\tilde{o}_{^3\Delta_1}$ with a relatively large error bar, and only put an upper bound of 1kHz for the isotope independent excited state Ω-doublet constant $\tilde{o}_{[20.6]\Omega=2}$. Nevertheless, the extracted $\tilde{o}_{^3\Delta_1}$ is consistent with the previous measurement, which is shown in table 3.8.

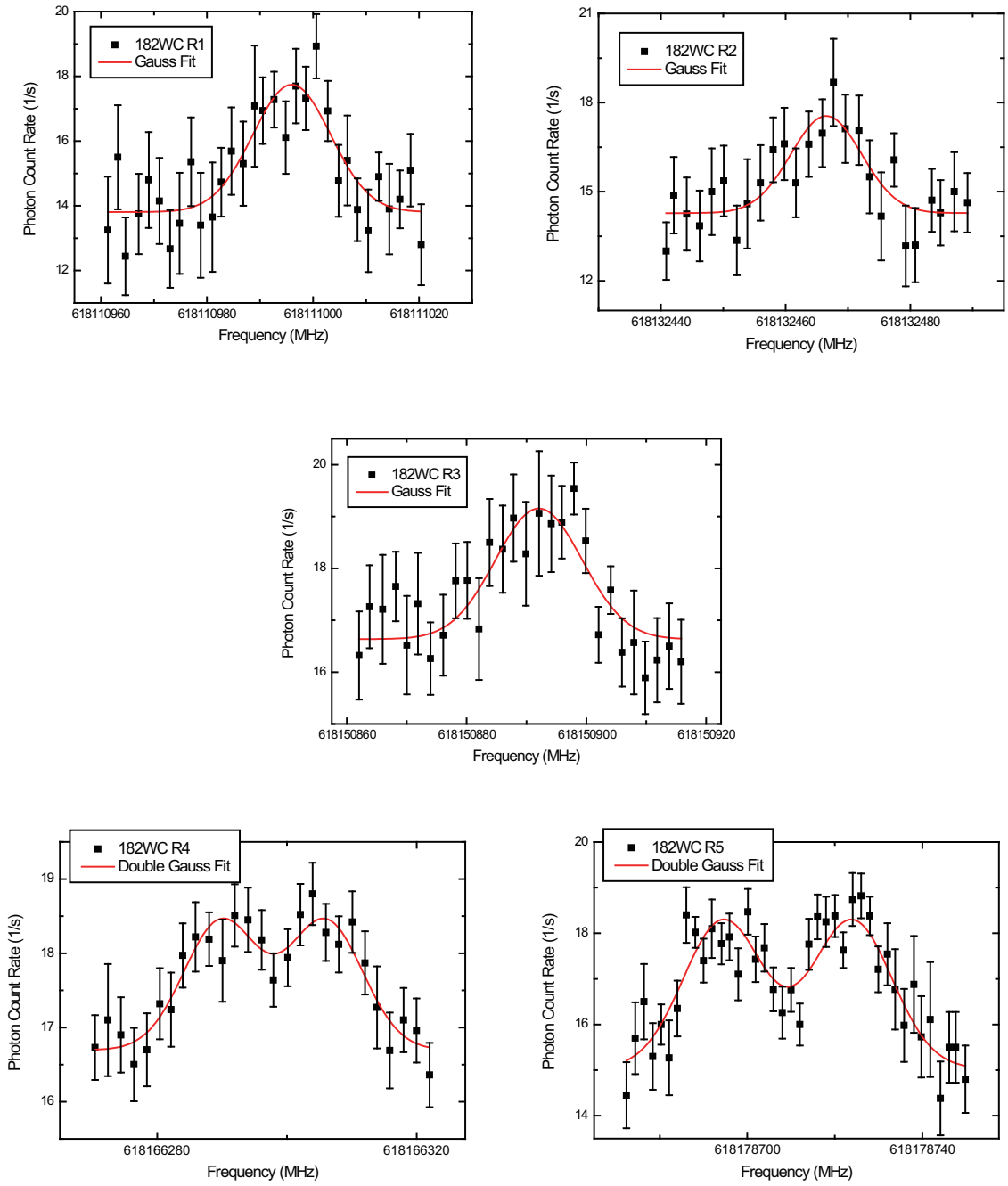

Figure B.1: The R(1) $\sim$ R(5) lines of the $[20.6]\Omega = 2, v' = 4 \leftarrow X^3\Delta_1, v" = 0$ transition for $^{182}W^{12}C$ are shown.

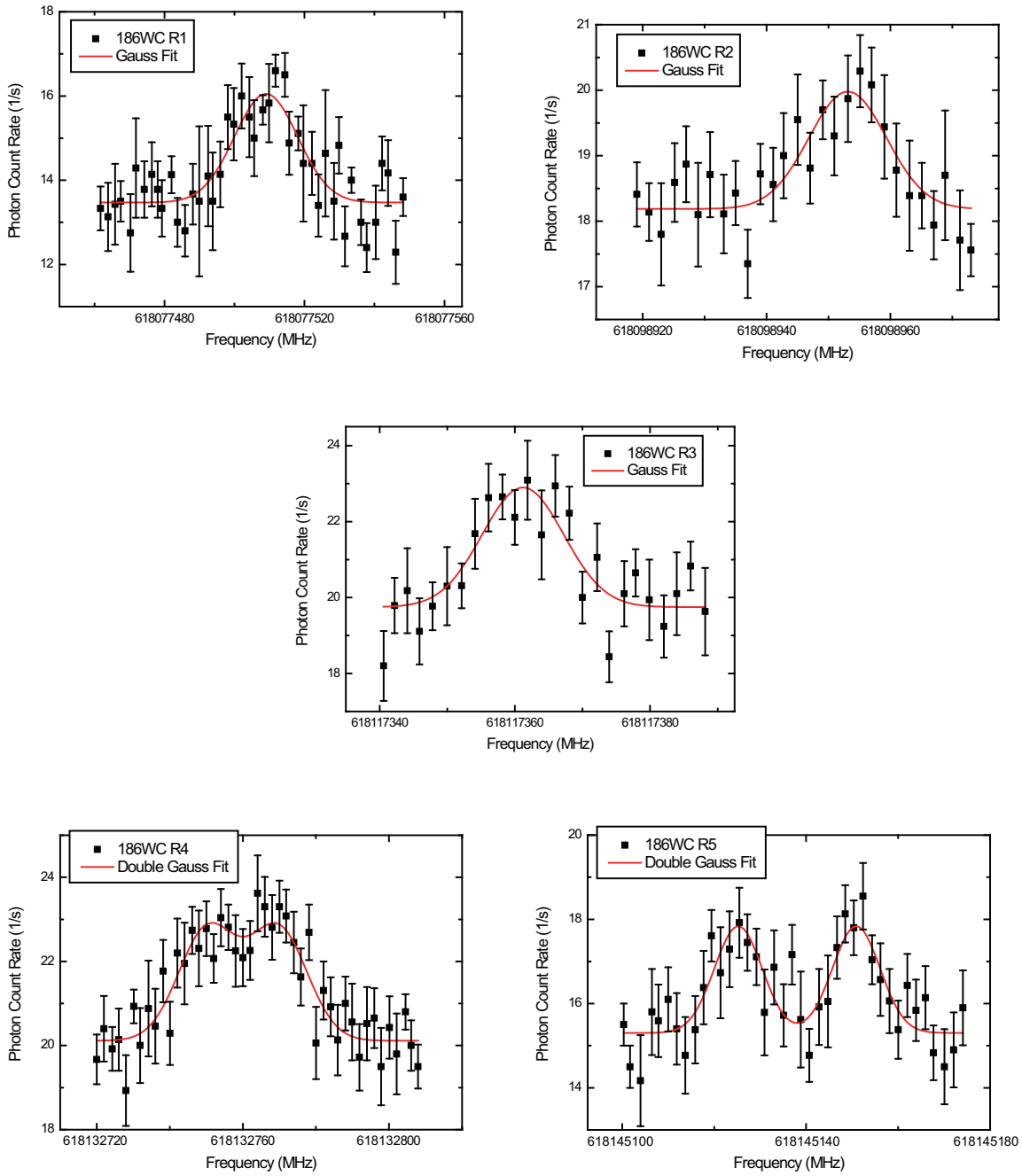

Figure B.2: The R(1) $\sim$ R(5) lines of the $[20.6]\Omega = 2, v' = 4 \leftarrow X^3\Delta_1, v" = 0$ transition for $^{186}W^{12}C$ are shown.

Table B.1: The measured Ω-doublet splittings of the $^{182}W^{12}C$, $^{184}W^{12}C$, $^{186}W^{12}C$ isotopes in the R(4) and R(5) lines of the $[20.6]\Omega = 2, v' = 4 \leftarrow X^3\Delta_1, v" = 0$ transition are shown. The 1 σ errors are shown inside the parentheses in the order of first parenthesis with the statistical uncertainty and the second parenthesis with the systematic uncertainty in relative frequencies. The residuals from the fits are shown on the third column for the $\{+,+\}$ case of eq. III.26, and the fourth column for the $\{+,-\}$ case.

Measured Line	Splitting (MHz)	Fit Residual for $\{+,+\}$ (MHz)	Fit Residual for $\{+,-\}$ (MHz)
$^{182}W^{12}C$, R(4)	16(1.6)(0.01)	-1.4	-1.7
$^{182}W^{12}C$, R(5)	28(1.6)(0.02)	1.3	1.5
$^{184}W^{12}C$, R(4)	18(1.6)(0.01)	0.7	0.4
$^{184}W^{12}C$, R(5)	27(1.6)(0.02)	0.3	0.5
$^{186}W^{12}C$, R(4)	18(1.6)(0.01)	0.7	0.4
$^{186}W^{12}C$, R(5)	25(1.6)(0.02)	-1.6	-1.4

BIBLIOGRAPHY

BIBLIOGRAPHY

[Ae08] C. Amsler and et al. *Phys. Lett. B*, 667:1, 2008.

[AHS87] P. Aufmuth, K. Heilig, and A. Steudel. *Atomic Data and Nuclear Data Tables*, 37:455, 1987.

[ALB04] A. B. Alekseyev, H. P. Liebermann, and R. J. Buenker. *Recent Advances in Relativistic Molecular Theory*. World Scientific, 2004.

[AMG07] J. M. Amini, C. T. Munger, Jr., and H. Gould. *Phys. Rev. A*, 75:063416, 2007.

[ASTW88] P. Aufmuth, A. Steudel, W. Tegtmeier, and E. Wöbker. *J. Phys. B*, 21:2253, 1988.

[ASW88] P. Aufmuth, A. Steudel, and E. Wöbker. *J. Phys. B*, 21:2237, 1988.

[B$\ddot{\text{o}}$2] S. Büttgenbach. *Hyperfine Structure in 4d- and 5d-Shell Atoms*. Springer-Verlag, 1982.

[Bal00] K. Balasubramanian. *J. Chem. Phys.*, 112:7425, 2000.

[BBP+85] S. A. Blundell, P. E. G. Baird, C. W. P. Palmer, D. N. Stacey, and G. K. Woodgate. *Z. Phys. A*, 321:31, 1985.

[BCM87] J. M. Brown, A. S. C. Cheung, and A. J. Merer. *J. Mol. Spect.*, 124:464, 1987.

[BDT79] S. Büttgenbach, R. Dicke, and F. Träber. *Phys. Rev. A*, 19:1383, 1979.

[BHJD09] S. Bickman, P. Hamilton, Y. Jiang, and D. DeMille. *Phys. Rev. A*, 80:023418, 2009.

[BLT83] R. V. Bensasson, E. J. Land, and T. G. Truscott. *Flash photolysis and pulse radiolysis: Contributions to the chemistry of biology and medicine*. Pergamon, 1983.

[Cam84] R. Campargue. *J. Phys. Chem.*, 88:4466, 1984.

[CKM10] K. N. Crabtree, C. A. Kauffman, and B. J. McCall. *Rev. Sci. Instrum.*, 81:086103, 2010.

[CLS84] G. Chambaud, B. Levy, and D. N. Stacey. *J. Phys. B*, 17:4285, 1984.

[Com07] E. D. Commins. *J. Phys. Soc. Jpn.*, 76:111010, 2007.

[DCKD09] S. C. Doret, C. B. Connolly, W. Ketterle, and J. M. Doyle. *Phys. Rev. Lett.*, 103:103005, 2009.

[DDPS81] T. G. Dietz, M. A. Duncan, D. E. Powers, and R. E. Smalley. *J. Chem. Phys.*, 74:6511, 1981.

[DKD04] S. Bickman Y. Jiang D. Kawall, F. Bay and D. DeMille. *Phys. Rev. Lett.*, 92:133007, 2004.

[Dun89] T. H. Dunning, Jr. *J. Chem. Phys.*, 90:1007, 1989.

[F+01] G. Federici et al. *Nucl. Fusion*, 41:1967, 2001.

[FB82] A. L. A. Fonseca and J. Bauche. *Z. Physik A*, 314:275, 1982.

[Fon28] G. R. Fonda. *Phys. Rev.*, 31:260, 1928.

[FS95] M. Fitzsimmons and V. K. Sarin. *Surf. Coat. Technol.*, 76:250, 1995.

[FW09] F. Fang and D. S. Weiss. *Opt. Lett.*, 34:169, 2009.

[GF74] R. J. Gallagher and J. B. Fenn. *J. Chem. Phys.*, 60:3487, 1974.

[Glu65] G. Gluck. *Ann. Phys., Paris*, 10:673, 1965.

[GSL+09] W. C. Griffith, M. D. Swallows, T. H. Loftus, M. V. Romalis, B. R. Heckel, and E. N. Fortson. *Phys. Rev. Lett.*, 102:101601, 2009.

[Hag63] O. F. Hagena. *Z. Angew. Physik*, 16:183, 1963.

[Hei] D. J. Heinzen. http://www.ph.utexas.edu/∼coldatom/.

[Hei85] K. Heilig. *Hyp. Int.*, 24:349, 1985.

[Hin97] E. A. Hinds. *Physica Scripta*, T70:34, 1997.

[HKS+11] J. J. Hudson, D. M. Kara, I. J. Smallman, B. E. Sauer, M. R. Tarbutt, and E. A. Hinds. *Nature*, 473:493, 2011.

[HOK78] J. Hojo, T. Oku, and A. Kato. *J. Less-Common Metal*, 59:85, 1978.

[HS74] K. Heilig and A. Steudel. *Atomic Data and Nuclear Data Tables*, 14:613, 1974.

[HSTH02] J. J. Hudson, B. E. Sauer, M. R. Tarbutt, and E. A. Hinds. *Phys. Rev. Lett.*, 89:023003, 2002.

[JW09] S. Jung and J. D. Wells. *Phys. Rev. D*, 80:015009, 2009.

[JWI+94] W. G. Jin, M. Wakasugi, T. T. Inamura, T. Murayama, T. Wakui, H. Katsuragawa, T. Ariga, T. Ishizuka, M. Koizumi, and I. Sugai. *Phys. Rev. A*, 49:762, 1994.

[KFD+87] M. G. Kozlov, V. I. Fomichev, Y. Y. Dmitriev, L. N. Labzowsky, and A. V. Titov. *J. Phys. B*, 20:4939, 1987.

[KG51] A. Kantrowitz and J. Grey. *Rev. Sci. Instrum.*, 22:328, 1951.

[Kin84] W. H. King. *Isotope Shifts in Atomic Spectra*. Springer, 1984.

[Kir] K. Kirch. http://nedm.web.psi.ch/EDM-world-wide/.

[KK04] J. C. Kim and B. K. Kim. *Scripta Mater*, 50:969, 2004.

[KL95] M. G. Kozlov and L. N. Labzowsky. *J. Phys. B*, 28:1933, 1995.

[Kop58] H. Kopfermann. *Nuclear Moments*. Academic, 1958.

[Lan12] I. Langmuir. *Phys. Rev.*, 34:406, 1912.

[Lan13] I. Langmuir. *Phys. Rev.*, 2:329, 1913.

[LBL+11] A. E. Leanhardt, J. L. Bohn, H. Loh, P. Maletinsky, E. R. Meyer, L. C. Sinclair, R. P. Stutz, and E. A. Cornell. *J. Mol. Spectrosc.*, 270:1–25, 2011.

[Lid09] D. R. Lide. *CRC Handbook of Chemistry and Physics*. CRC-Press, 2009.

[LMP+09] J. Lee, E. R. Meyer, R. Paudel, J. L. Bohn, and A. E. Leanhardt. *J. Mod. Opt.*, 56:2005, 2009.

[LSH89] A. Lipp, K. A. Schwetz, and K. Hunold. *J. Euro. Cera. Soc.*, 5:3, 1989.

[LWO11] C.-Y. Lien, S. R. Williams, and B. Odom. *Phys. Chem. Chem. Phys.*, 13:18825, 2011.

[Mat58] T. Matsuoka. *Toshiba Rev.*, 13-5:519–523, 1958.

[MB08a] E. R. Meyer and J. L. Bohn. *Phys. Rev. A*, 78:010502, 2008.

[MB08b] E. R. Meyer and J. L. Bohn. *Bull. Am. Phys. Soc.*, 53:28, 2008.

[MBD06] E. R. Meyer, J. L. Bohn, and M. P. Deskevich. *Phys. Rev. A*, 73:062108, 2006.

[MCH+93] I. Mills, T. Cvitas, K. Homann, N. Kallay, and K. Kuchitsu. *Quantities, units, and symbols in physical chemistry*. Blackwell Scientific Publications, 1993.

[Mor00] D. C. Morton. *Astrophys. J. Suppl. Ser.*, 130:403, 2000.

[Mor11] M. D. Morse. *Private Communication*, 2011.

[MS82] A. M. Martensson and S. Salomonson. *J. Phys. B*, 15:2115, 1982.

[MS99] H. J. Metcalf and P. V. D. Straten. *Laser Cooling and Trapping*. Springer, 1999.

[MTEK01] N. S. Mosyagin, A. V. Titov, E. Eliav, and U. Kaldor. *J. Chem. Phys.*, 115:2007, 2001.

[MZT10] N. S. Mosyagin, A. V. Zaitsevskii, and A. V. Titov. *Review of Atomic and Molecular Physics*, 1:63, 2010.

[N+96] R. Neu et al. *Plasma Phys. Control. Fusion*, 38:A165, 1996.

[NOW+10] K.-K. Ni, S. Ospelkaus, D. Wang, G. Que'me'ner, B. Neyenhuis, M. H. G. de Miranda, J. L. Bohn, J. Ye, and D. S. Jin. *Nature*, 464:1324, 2010.

[Pet11] A. N. Petrov. *Phys. Rev. A*, 83:024502, 2011.

[Pie92] H. O. Pierson. *Handbook of Chemical Vapor Deposition(CVD): Principles, Technology, and Applications*. William Andrew Inc., 1992.

[PMT09] A. N. Petrov, N. S. Mosyagin, and A. V. Titov. *Phys. Rev. A*, 79:012505, 2009.

[PR50] E. M. Purcell and N. F. Ramsey. *Phys. Rev.*, 78:807, 1950.

[PR05] M. Pospelov and A. Ritz. *Ann. Phys.*, 318:119, 2005.

[PSK+09] K. Pandey, A. K. Singh, P. V. K. Kumar, M. V. Suryanarayana, and V. Natarajan. *Phys. Rev. A*, 80:022518, 2009.

[Ram50] N. F. Ramsey. *Phys. Rev.*, 78:695, 1950.

[RCSD02] B. C. Regan, E. D. Commins, C. J. Schmidt, and D. DeMille. *Phys. Rev. Lett.*, 88:071805, 2002.

[RHJ08] D. Rothgeb, E. Hossain, and C. C. Jarrold. *J. Chem. Phys.*, 129:114304, 2008.

[RVK09] B. Friedrich R. V. Krems, W. C. Stwalley. *Cold Molecules: Theory, Experiment, Applications*. CRC-Press, 2009.

[San66] P. G. H. Sandars. *Phys. Lett.*, 22:290, 1966.

[San67] P. G. H. Sandars. *Phys. Rev. Lett.*, 19:1396, 1967.

[SBD10] E. S. Shuman, J. F. Berry, and D. DeMille. *Nature*, 467:820, 2010.

[SCCW06] F. Stevens, I. Carmichael, F. Callens, and M. Waroquier. *J. Phys. Chem. A*, 110:4846, 2006.

[SCMW03] T. Sugie, A. Costley, A. Malaquias, and C. Walker. *J. Plasma Fusion Res.*, 79:1051, 2003.

[Sco88] G. Scoles. *Atomic and Molecular Beam Methods.* Oxford University Press, 1988.

[Sel69] E. C. Seltzer. *Phys. Rev.*, 188:1916, 1969.

[SGH+11] J. F. Stanton, J. Gauss, M. E. Harding, P. G. Szalay, et al. cfour: a program package for performing high-level quantum chemical calculations on atoms and molecules, http://www.cfour.de, 2011.

[Ski09] C. H. Skinner. *Phys. Scr.*, T134:014022, 2009.

[SPH03] K. E. Strecker, G. B. Partridge, and R. G. Hulet. *Phys. Rev. Lett.*, 91:080406, 2003.

[SR06] N. E. Shafer-Ray. *Phys. Rev. A*, 73:034102, 2006.

[SSM02] S. M. Sickafoose, A. W. Smith, and M. D. Morse. *J. Chem. Phys.*, 116:993, 2002.

[TM99] A. V. Titov and N. S. Mosyagin. *Int. J. Quantum Chem.*, 71:359, 1999.

[TMAB01] A. V. Titov, N. S. Mosyagin, A. B. Alekseyev, and R. J. Buenker. *Int. J. Quantum Chem.*, 81:409, 2001.

[TMP+06] A. V. Titov, N. S. Mosyagin, A. N. Petrov, T. A. Isaev, and D. P. DeMille. *Progr. Theor. Chem. Phys. B*, 15:253, 2006.

[VCG+10] A. C. Vutha, W. C. Campbell, Y. V. Gurevich, N. R. Hutzler, M. Parsons, D. Patterson, E. Petrik, B. Spaun, J. M. Doyle, G. Gabrielse, and D. DeMille. *J. Phys. B*, 43:074007, 2010.

[WBZJ99] J. Weiner, V. Bagnato, S. Zilio, and P. S. Julienne. *Rev. Mod. Phys.*, 71:1, 1999.

[Weg74] P. P. Wegener. *Molecular Beams and Low Density Gasdynamics.* Marcel Dekker Inc., 1974.

[Wel84] A. F. Wells. *Structural Inorganic Chemistry.* Oxford Science Publications, 1984.

[Win75] H. F. Winters. *J. Chem. Phys.*, 62:2454, 1975.

[WS11a] F. Wang and T. C. Steimle. *J. Chem. Phys.*, 135:104313, 2011.

[WS11b] F. Wang and T. C. Steimle. *J. Chem. Phys.*, 134:201106, 2011.

[WS12] F. Wang and T. C. Steimle. *J. Chem. Phys.*, 136:044312, 2012.

[Wya10] J. Wyart. *J. Phys. B*, 43:074018, 2010.